

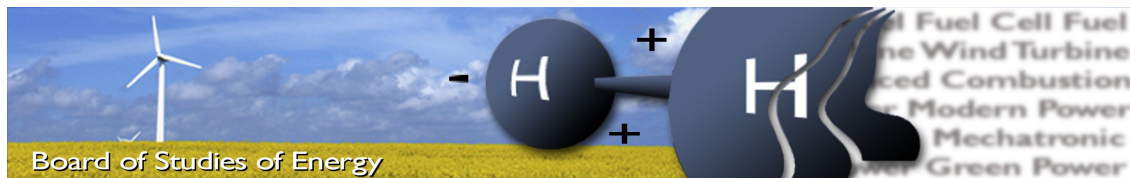
Master's Thesis:

Model Predictive Control of a Discrete Displacement Hydraulic Power Take-Off System



MCE4-1027
Magnus F. Asmussen
Nikolaj S. Høyer

Department of Energy Technology
Aalborg University
Mechatronic Control Engineering
June 1st 2017



Title: Model Predictive Control
of a Discrete Displacement Hydraulic Power Take-Off System

Semester: Master's Thesis in Mechatronic Control Engineering

Project period: 1.2.2017 to 1.6.2017

ECTS: 30

Supervisor: Anders Hedegaard Hansen

Project group: MCE4-1027

Magnus Færing Asmussen

Nikolaj Skaanning Høyer

Pages, total: 88
Appendices: A-C.

SYNOPSIS:

In this thesis a model predictive control scheme of a discrete displacement hydraulic power take-off system is developed. The thesis takes offset in the Wave Star wave energy converter for which a discrete fluid power power take-off system has been proposed. No optimal control structure of such system has yet been developed, why this work investigates the potential of model predictive control. A model of the PTO system is developed and validated by measurements performed on a hydraulic test bench. A model predictive control scheme maximising the harvested energy of the system including system losses is formulated. The control scheme requires a discrete optimisation problem to be solved in real time. Differential evolution is used as optimisation solver and is modified to fit the discrete optimisation problem and effort in lowering the computational time has been done by model simplifications and loss approximation. The proposed control scheme is implemented on the test bench and is compared to previous developed reactive control scheme. Tests show that the developed model predictive control may be implemented and executed in real time. Tests performed on the test bench suggest that the model predictive control scheme can outperform the reactive control scheme with respect to the average harvested power from the ocean waves.

By accepting the request from the fellow student who uploads the study group's project report in Digital Exam System, you confirm that all group members have participated in the project work, and thereby all members are collectively liable for the contents of the report. Furthermore, all group members confirm that the report does not include plagiarism.

Preface

This Master's thesis is written by student group MCE4-1027 in the spring semester of 2017 at Aalborg University at the Department of Energy Technology, Mechatronic Control Engineering. The thesis concerns development of a Model Predictive Control scheme for a discrete displacement hydraulic power take-off system for a wave energy converter. A case study of the Wave Star wave energy converter is done, as a hydraulic test bench located at AAU is available. The test bench is designed such that a power take-off system may be subjected to motion equal to the float arm of the Wave Star wave energy converter. This allows for test of model predictive control algorithms in a controlled environment.

Reader's Guide

A nomenclature containing symbol declaration and their respective units is found on page ix. All citations used can be found in the bibliography on page 90. The bibliography is sorted by numeration as they appear in the report. Equations, tables and figures are numbered as: (Chapter.Number).

Matrices are denoted with bold upper case letters and vectors are denoted with bold lower case letters. A list of selected terms used in the report is shown below:

Terminology

- *Absorbed Power* - Defined as the instantaneous produced mechanical power on the point absorber.
- *Harvested Power* - Defined as the instantaneous power going out of the PTO system.
- *Time Horizon* - Time interval over which the MPC optimises for control inputs.
- *Horizon Length* - Number of samples forward in time for which the MPC optimises for control inputs.

Abbreviations

PTO	Power Take-Off	BnB	Branch and Bound
MPC	Model Predictive Control	WEC	Wave Energy Converter
EMPC	Explicit Model Predictive Control	SS	Sea State
PSD	Power Spectral Density	DDC	Discrete Displacement Cylinder
WPEA	Wave Power Extraction Algorithm	FSA	Force Shifting Algorithm
DE	Differential Evolution	DFCU	Discrete Fluid Control Unit

Summary

In this thesis, a model predictive control scheme for a discrete displacement hydraulic power take-off system utilised in a wave energy converter is developed and tested. The thesis takes offset in the Wave Star point absorber wave energy converter, for which a discrete fluid power system has been proposed as power take-off system. Through literature survey it is found that model predictive control of wave energy converters has emerged as a leading control topology for wave energy conversion, but has yet to be tested for a discrete fluid power PTO system.

To develop a model predictive control algorithm, a model of the Wave Star WEC has been developed, along with a model of the discrete fluid power PTO system. Losses in the PTO system are addressed and modelled with the goal of including these in the MPC formulation. The model of the PTO system is validated from measurements performed on a hydraulic PTO test bench of the Wave Star WEC, located at Aalborg University.

A MPC controller is formulated based on a linear model of the point absorber, with the objective function of maximising the harvested energy over a finite time horizon. An analysis of the MPC performance assuming continuous PTO force is performed. This allows for confirmation of the optimality obtained by the MPC, and preliminary requirements regarding MPC time horizon and sample time. A wave forecasting scheme based on an autoregressive model is developed and tested. It is shown that wave forecasting may be obtained for 2-3 seconds forward in time, and it is shown that close to ideal performance may be obtained with the developed wave forecasting scheme.

A discrete optimisation routine based on a differential evolution algorithm is utilized to handle the discrete nature of the discrete fluid power PTO system. Losses associated with force shifting, and valve flow throttling is included in the pursuit of increasing the efficiency of the PTO transmission. Emphasis in optimising the DE algorithm with respect to execution time is done, to obtain convergence time allowing real time implementation of the MPC scheme.

Experimental evaluation of the developed MPC is done. The MPC is implemented and tested in a LabVIEW RT environment. Three MPC formulation are tested, with different loss mechanisms included in the MPC cost function. Depending on the amount of losses included in the MPC cost function, sample times of 0.2s and 0.3s of the MPC was obtained with the chosen implementation of the MPC code. The MPC was tested for several test waves, and the performance was compared to the previous used reactive control scheme. Based on the experimental evaluation it was found that the MPC was able to increase the harvested energy compared to the reactive control scheme. In smaller wave the MPC was seen to yield less harvested energy than the reactive control. The trends obtained from the experimental evaluation is backed up by simulations, where it is shown that additional performance may be obtained by including more accurate computation of the losses in the PTO transmission, or by increasing the time horizon. However it is shown by simulation that increasing the time horizon beyond 4 seconds does not result in better performance of the MPC.

It is concluded that MPC may be applicable for a discrete displacement hydraulic PTO system, and it may increase the amount of harvested energy compared to the reactive control scheme previously utilised.

Nomenclature

Symbol	Description	Unit
A_i	Piston area of i'th cylinder chamber of the PTO cylinder	$[m^2]$
B_{pto}	Reactive control damping parameter	$[\frac{Ns}{m}]$
C_{il}	Internal leakage coefficient	$[\frac{m^3}{sPa}]$
d_a	Moment arm of absorber	$[m]$
F_{pto}	PTO cylinder force	$[N]$
H_m	Significant wave height	$[m]$
J_{tot}	Total moment of inertia of float arm	$[kgm^2]$
J_{∞}	Added moment of inertia from water acceleration	$[kgm^2]$
k_{pto}	Reactive control spring parameter	$[\frac{N}{m}]$
k_{res}	Restoring torque coefficient	$[\frac{Nm}{rad}]$
k_v	Valve flow gain	$[\frac{m^3}{s\sqrt{Pa}}]$
L_i	Length of the i'th line element	$[m]$
m	Mass	$[kg]$
N	Horizon length of MPC	$[-]$
n_i	Number of valve used in DFCU	$[-]$
p_A	Wave cylinder chamber A pressure	$[Pa]$
p_B	Wave cylinder chamber B pressure	$[Pa]$
p_i	Pressure in the i'th chamber of the PTO cylinder	$[Pa]$
P_S	Wave cylinder supply pressure	$[Pa]$
P_T	Wave cylinder tank pressure	$[Pa]$
P_{abs}	Absorbed power	$[W]$
P_{har}	Harvested power	$[W]$
Q_i	Flow into the i'th chamber of the PTO cylinder	$[\frac{m^3}{s}]$
x_c	PTO cylinder position	$[m]$
x_v	Normalised equivalent valve spool position	$[\pm 1]$
T_{wp}	Peak wave period	$[s]$
T_s	Sample time of MPC	$[s]$
T_p	Pressure development time	$[s]$
$V_{0,i}$	Dead volume of i'th PTO cylinder chamber	$[m^3]$
v_c	PTO cylinder velocity	$[\frac{m}{s}]$
β	Bulk modulus	$[Pa]$
η	PTO transmission efficiency	$[-]$
η_w	Wave height	$[m]$
θ_{arm}	Angular position float arm	$[rad]$
λ	Fluid friction factor	$[-]$
μ	Dynamic viscosity	$[Pa s]$
ρ	Fluid density	$[\frac{kg}{m^3}]$
τ_{ext}	Excitation torque	$[Nm]$
τ_{pto}	PTO torque	$[Nm]$
τ_{rad}	Radiation torque	$[Nm]$
ω_{arm}	Angular velocity of float arm	$[\frac{rad}{s}]$

Contents

1	Introduction	1
1.1	Hydraulic Power Take-Off System	3
1.2	Reactive Control for Test Bench	6
1.3	MPC for WECs and Systems with Quantized Inputs	7
2	Problem Statement	11
2.1	Project Scope	11
2.2	Solution Strategy	11
3	System Model	13
3.1	Absorber Model	13
3.2	PTO Model	18
3.3	Test Bench Model	23
3.4	Losses in the PTO Transmission	26
3.5	Validation	30
3.6	Part Conclusion	36
4	Model Predictive Control	37
4.1	MPC Formulation	37
4.2	MPC Analysis	40
4.3	Part Conclusion	52
5	Quantized Input MPC	53
5.1	Cost Function Variable	53
5.2	Absorber to Cylinder Space	53
5.3	MPC Sample Time	55
5.4	Cost Functions	56
5.5	Optimisation Algorithm	58
5.6	Convergence time	63
5.7	Differential Evolution Algorithm	64
5.8	Differential Evolution Modification	65
6	MPC Simulation Evaluation	69
6.1	Model Complexity and Time Horizon	70
6.2	Evaluation of MPC Computational Time	71
6.3	Part Conclusion	73
7	Experimental Evaluation	75
7.1	DE Code Implementation	76
7.2	Evaluation	77
7.3	MPC with Wave Forecasting	84
7.4	Part Conclusion	85
8	Conclusion	87
	Bibliography	88
	Supplement A Branch and Bound Algorithm	91

Supplement B LabVIEW Program	95
B.1 Timing and Finish Late Handling	96
B.2 MATLAB Code	99
Supplement C Results	103

1 | Introduction

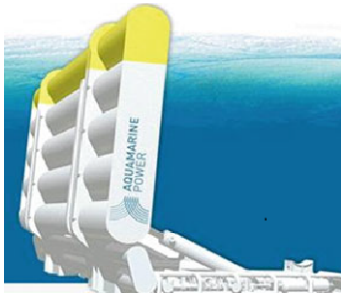
The environmental impact of large scale use of fossil fuels combined with the world's increasing demand of energy has augmented research within renewable energy sources. Many years of research have lead to well-established technologies for conversion of renewable energy sources such as wind and solar power. Wave energy is another renewable energy source with great potential which has not yet been fully exploited. As an example, a rough estimate is given in [1], where it is stated that a practical upper limit for wave energy production could supply 1/3 of the Danish electricity demand in 2009.

The conversion of ocean waves into electricity is an old idea. Earliest recorded interest of wave energy conversion dates to a patent from 1799[2]. Wave energy conversion has yet to make a commercial break through, as existing technologies are still too costly compared to well-developed technologies within solar and wind power. Thus, an unused potential of wave ocean energy exists. For wave energy to become a reliable and feasible renewable energy source in the future, optimisation of wave energy conversion is necessary. Most commonly wave energy converters are designed as oscillating bodies moving with the vertical motion of the ocean surface level. The energy associated with the oscillating motion of the body is converted into electricity by the system referred to as the power take-off (PTO) system. The oscillating body and the PTO system combined forms a device referred to as a wave energy converter (WEC).

Several topologies for WECs are seen, however they may all be categorized using terms such as terminators, attenuators, and point absorbers. An example of a WEC of the terminator type is shown in Figure 1.1a and 1.1d. The WEC is named Oyster and is restrained to the seabed, and oscillating flaps are moved by the ocean waves. A PTO system is positioned between the flaps and the structure on the seabed. An attenuator type of WEC is the Pelamis WEC shown in Figure 1.1b and 1.1e. Several oscillating body parts are linked in universal joints which allows both vertical and horizontal motion. A PTO system is placed in the joints converting the relative motion between the body parts into electricity. A point absorber type of WEC is the PowerBuoy shown in Figure 1.1c and 1.1f. Here the heaving(vertical) motion relative to a fixed body is converted into electricity by a PTO system dampening the relative motion. Common for these WECs is that they are in a development phase.

The many different ideas and technologies of wave energy conversion still being tested and designed, is an indication of the immature state of wave energy conversion.

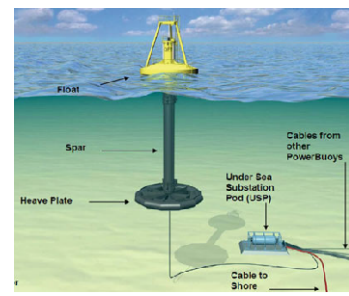
Another example of a WEC is the Wave Star C5 point absorber prototype deployed in Hanstholm, DK. The Wave Star WEC consists of a buoyant body point absorber attached to a lever arm. The oscillating motion of the point absorber creates a rotational motion with respect to the joint of the lever arm and a PTO system is positioned between the oscillating lever arm and the fixed structure of the WEC. Through the history of Wave Star, several WEC prototypes has been deployed. The latest prototype was deployed in 2009 and is a 110kW test machine connected to and feeding the Danish grid. The Wave Star prototype uses a hydraulic PTO system to exert a force opposing the motion of the point absorber, such that energy is extracted from the float arm motion. The prototype deployed in Hanstholm has two absorbers while the final concept is based on having multiple absorbers on one platform that may be installed associated with an offshore wind turbine, or as a standalone instalment. The Wave Star C5 prototype is shown in Figure 1.2 and technical data for the prototype is shown in Table 1.1. To contribute to the



(a) Oyster terminator type WEC.



(b) Pelamis attenuator type WEC.



(c) PowerBuoy point absorber type WEC.



(d) Oyster terminator type WEC.



(e) Pelamis attenuator type WEC.



(f) PowerBuoy point absorber type WEC.

Figure 1.1: Figures of different wave energy converters[3],[4][2].

research within wave energy this thesis will focus on Model Predictive Control (MPC) of the PTO system with the goal of increasing the energy captured by the WEC. The Wave Star WEC is used as a case study. The hydraulic PTO system of the Wave Star WEC is presented in the next section, along with the Wave Power Extraction Algorithm(WPEA) previously used in the control of the PTO system.



Figure 1.2: Picture of the Wavestar C5 prototype deployed in Hanstholm, DK.

Wavestar C5 prototype	
Location	Hanstholm, DK
Float diameter	Ø5m
Arm length	10m
Water depth	5 to 8m
Number of floats	2
Weight	1000 tons
Nominal electrical power	110kW
Deployment	2009-2016

Table 1.1: Technical data for the Wave Star C5 prototype deployed in Hanstholm, DK[5].

1.1 Hydraulic Power Take-Off System

The PTO system is an essential part of the WEC as it is the part extracting energy from the wave motion. Due to the relative slow oscillation of ocean waves, high torque/force is needed for high power transfer. For this reason, hydraulic PTO systems are often preferred as these provides high force density and great controllability. The PTO system previously used for the Wave Star WEC consisted of a symmetric cylinder connected to a bidirectional variable displacement axial piston motor/pump. The pressures in the cylinder chambers, hence the produced cylinder force, is controlled by varying the motor/pump swash plate angle. In [6] it was shown that this configuration yields low efficiency due to large variations in the motor loading. For this reason a discrete fluid power system has been proposed. Using a discrete fluid power system as PTO system restricts the applied force to quantised values which reduces the controllability. As a consequence the control strategies used to compute the control input may increase in complexity as the control input cannot be chosen freely. A general introduction to discrete fluid power system is given in the next section, along with a description of the discrete fluid power system proposed for the Wave Star WEC.

1.1.1 Discrete Fluid Power Systems

Discrete fluid power systems are characterized by using control units which only take discrete values. Control units such as fast switching on/off valves, characterised by either being fully opened or closed during operation, are used in discrete fluid power systems. By proper selection of the valve opening area the throttling loss is reduced, hence higher efficiency may be obtained when compared to systems utilising traditional proportional valves. A subclass of discrete fluid power systems is secondary controlled systems where on/off valves are used to connect each chamber of a hydraulic actuator to common pressure lines. Effectively a Discrete Displacement Cylinder(DDC) is obtained which can exert a number of discrete forces. The number of cylinder chambers and pressure lines determines the number of forces available. Two examples of such systems are shown in Figure 1.3. The first example is a cylinder with two chambers connected to three common pressure lines yielding $3^2 = 9$ discrete forces. The other is a cylinder with three chambers connected to three pressure lines yielding $3^3 = 27$ discrete forces. A disadvantage of secondary controlled systems is that the cylinder force cannot vary freely, but can only take a number of discrete forces. Hence the system is a system with quantised inputs. Due to the fast switching of the valves, shifting between the available forces imposes a near step input to the system at each force shift. This may excite the natural frequency of low mass systems, why this can cause both mechanical fatigue problems and difficulties in motion control of the cylinder piston.

Efficient control of the hydraulic cylinder may be obtained by secondary control. Ideally flow throttling loss is avoided, however losses associated with the switching between the discrete force levels due to oil compressibility are present[7]. Despite losses, high efficiency of the discrete fluid power system shown in Figure 1.3 may be obtained why it is an attractive PTO topology for wave energy converters.

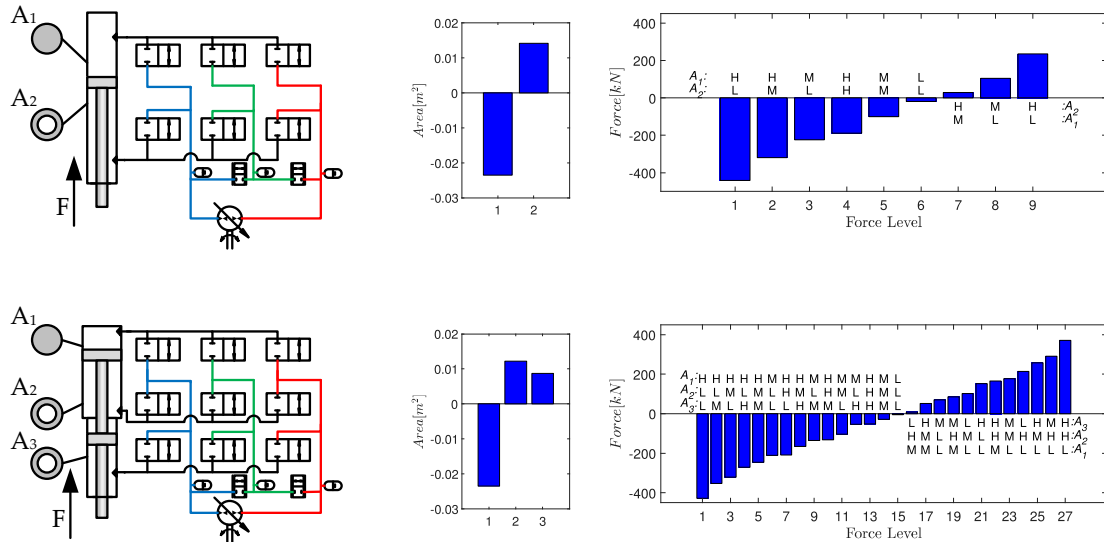


Figure 1.3: Examples of secondary controlled systems with 200bar on the high pressure line, 107.5bar on the intermediate pressure line and 20bar on the low pressure line. The sign of the area indicates the direction of the resulting force.

1.1.2 Wave Star Power Take-Off System

An illustration of the Wave Star WEC along with the layout of the hydraulic PTO system is shown in Figure 1.4.

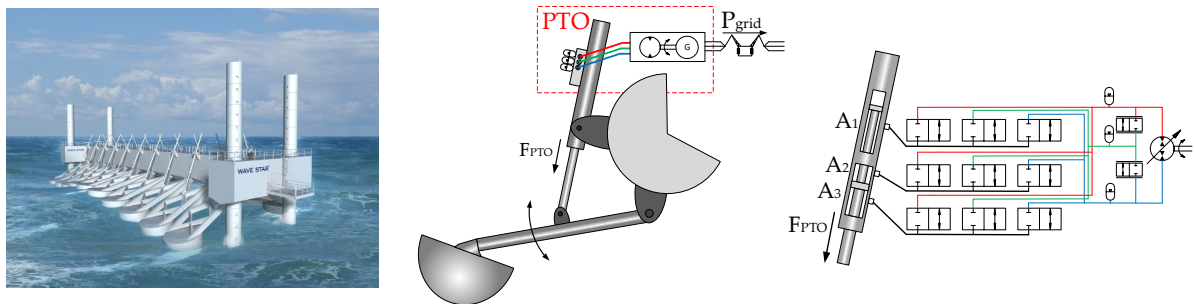


Figure 1.4: Illustration of the Wavestar WEC prototype and the discrete fluid power PTO system.

The hydraulic PTO cylinder is a multi chamber cylinder, where three of the chambers are utilized. Combined with three common pressure lines, 27 discrete forces are available for opposing the motion of the point absorber. The disadvantage of secondary controlled systems yielding large acceleration of the system between force shifts is minimised due the relatively large mass of the point absorber. A hydraulic motor between the high- and low pressure line is used to convert the fluid energy into rotational energy driving an electrical generator, feeding the grid. In [8] a comprehensive investigation of WPEAs for the Wave Star prototype is performed. Through simulation and scaled model testing, a reactive control scheme was chosen as the WPEA extracting most energy. The reactive control generates a continuous force trajectory to be tracked by the PTO cylinder. The simplest

method of tracking the continuous force reference is to choose the closest discrete force available, however this may not be optimal energy-wise due the aforementioned shifting losses associated to each force shift. A Force Shift Algorithm(FSA) described in[9] is used to switch between forces. The energy cost associated with each force shift is estimated and force shifts are chosen as a compromise between force tracking and shifting losses. This approach takes a part of the system losses into account but may be sub optimal considering the harvested energy, as the utilised FSA only considers the current cost of shifting and does not take future states into account. The reactive control scheme along with the FSA was developed by use of a PTO test bench located at AAU. The test bench is designed to exert a PTO system to a motion equal to the float arm of the Wave Star WEC. The hydraulic PTO test bench is presented in the next section.

1.1.3 PTO Test Bench at AAU

The test bench is equipped with a full-scale version of the proposed discrete displacement hydraulic PTO cylinder of the Wave Star WEC. A symmetric cylinder (250mm/180mm x 3000mm) is used to load the PTO cylinder, and is controlled to emulate the motion of a single C5 point absorber of the Wave Star WEC interacting with the ocean waves, hence the cylinder is denoted as the wave cylinder. The wave cylinder is able to exert a force of 840kN onto the PTO cylinder. By appropriate motion control of the wave cylinder, the test bench may be used to test different PTO control strategies in large variety of emulated ocean waves in a controlled environment. Pictures of the test bench are shown in Figure 1.5 and 1.6.

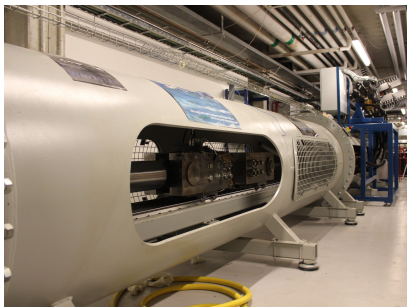


Figure 1.5: Picture of the PTO test bench.



Figure 1.6: Picture of the PTO test bench.

Given a wave time series as input, the position and velocity reference of the wave cylinder is computed based on an online simulation of the C5 point absorber dynamics using position, velocity and force feedback of the PTO cylinder. A diagram of the test bench is illustrated in Figure 1.7.

Each chamber of the PTO cylinder is connected to the three pressure lines through three digital flow control units(DFCU). The DFCUs consist of a set of fast switching on/off valves in parallel, which combined operate as a proportional valve with quantised opening area. Valve opening trajectories are utilized to minimise pressure oscillations in the cylinder chambers. The total opening area of the DFCUs are matched according to the connected chamber piston area, why different number of valves are utilised, depending on which chamber is connected to the DFCU. The wave- and PTO cylinder are mechanically linked by a sliding mass where position, velocity and force transducers are placed. The

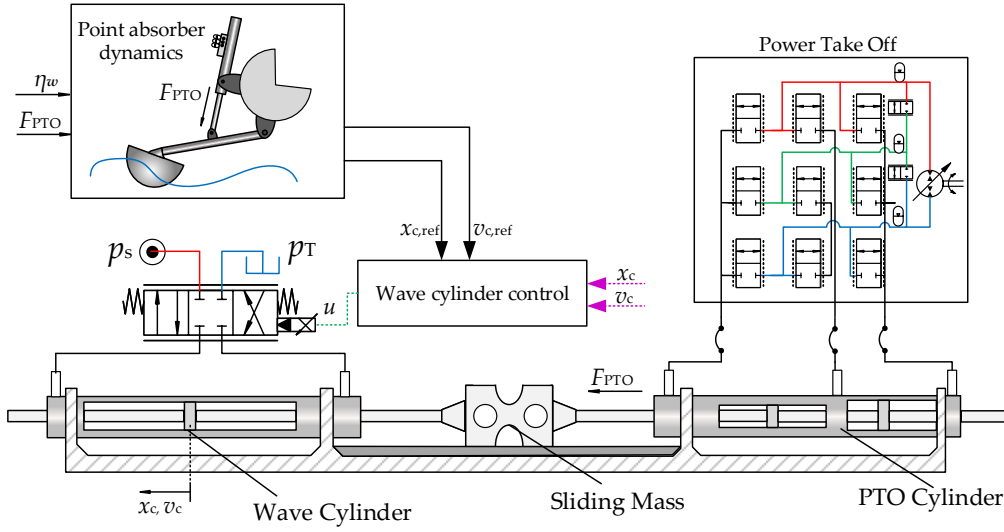


Figure 1.7: Diagram of the PTO test bench at AAU.

WPEA used to compute the PTO cylinder force reference is presented in the next section.

1.2 Reactive Control for Test Bench

In [8] reactive control was found as the best suited WPEA for the discrete fluid power PTO system developed for the Wave Star test bench. The reactive control strategy computes a continuous force reference for the PTO cylinder as shown below:

$$F_{pto} = k_{pto}x_c + B_{pto}v_c \quad (1.1)$$

Where x_c is the cylinder piston position and v_c is the cylinder piston velocity. The parameters for the reactive control, B_{pto} and k_{pto} , were found by optimising the output power for different sea states defining the characteristics of ocean waves. Optimal choice of control parameters exist for different sea states, why the parameters are changed according to the sea state to maximise harvested energy. As the force applied by the PTO system is restricted to a number of force levels the continuous force reference from the reactive control is transformed to a discrete level by the aforementioned FSA. The FSA works by defining a maximum allowed tracking error that the PTO force may deviate from the force reference. Within that range, the FSA may choose the available force shift associated with the lowest shifting loss found from a lookup table. Further a fixed time limit is used to decide how often a force shift is allowed. In Figure 1.8 the FSA is sketched with the governing equations in Equation (1.2), (1.3) and (1.4)[9].

$$F_{pto}(t) = F(k), \quad k = \underset{k \in \{k_-, x, k_+\}}{\operatorname{argmin}_k} \{F_{ref} - F(k)\} \quad (1.2)$$

$$k_+ = \underset{k \in S_+}{\operatorname{argmin}_k} \{E(x_c, k)\}, \quad S_+ = \{k | F_{ref} < F(k) < F_{ref} + F_b\} \quad (1.3)$$

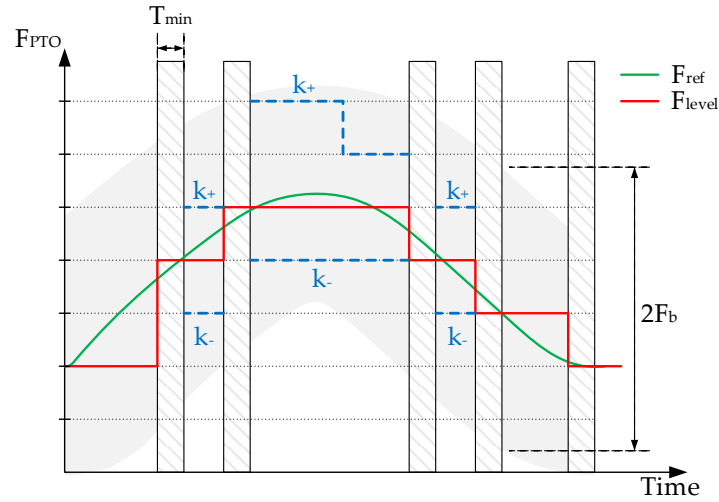


Figure 1.8: Illustration of the force shifting algorithm.

$$k_- = \underset{k \in S_-}{\operatorname{argmin}_k} \{E(x_c, k)\}, \quad S_- = \{k | F_{\text{ref}} - F_b < F(k) < F_{\text{ref}}\} \quad (1.4)$$

Where F is a vector of available forces, F_{ref} is the force reference calculated from (1.1) and F_b is the allowed deviation from the force reference. E is the loss associated with the force shift in a given position. k_+ and k_- are the force shifts associated with lowest loss contained in the sets, S_+ and S_- . S_+ and S_- contains all the force levels inside the allowed deviation from the reference above and below the reference respectively.

Shifting the force level is thus based on some force tracking error and information regarding the losses associated with different force shifts. The disadvantage of the reactive control scheme with the described FSA is that it only considers the current state of the system. It is unknown if the chosen compromise between tracking and losses is optimal considering harvested energy over a longer time horizon. It may be possible to choose more expensive force shifts that accumulated over a time period yields more harvested energy. To increase the amount of harvested energy from point absorbers MPC has been proposed. MPC rely on a model of the system and calculates the control input based on estimated future states of the system. This is done by optimising the control inputs subject to a cost function over a finite time horizon. MPC may have the potential of finding the optimal control input, taking future control inputs into account, why this may be an attractive control scheme for the PTO system of the Wave Star WEC. Some research regarding MPC for WECs have already been done which is reviewed in the next section.

1.3 MPC for WECs and Systems with Quantized Inputs

The basic idea of MPC is to compute the current control input by solving an open loop finite horizon optimal control problem by solving an optimisation problem online at each

time step. A model of the plant is used to estimate future states subject to future control inputs, possible future disturbances and initial conditions. The solution of the optimisation problem is a sequence of future control input over the finite time horizon, where the first control input is applied to the plant. Once new information regarding the plant states are obtained, the process is repeated where the time horizon is shifted one sample period forward in time. A block diagram of a MPC scheme is shown in Figure 1.9. The notation $(k+i|k)$ denotes the future values forward in time at time k over a given horizon where $i = 1 \dots N$ and N is the horizon length.

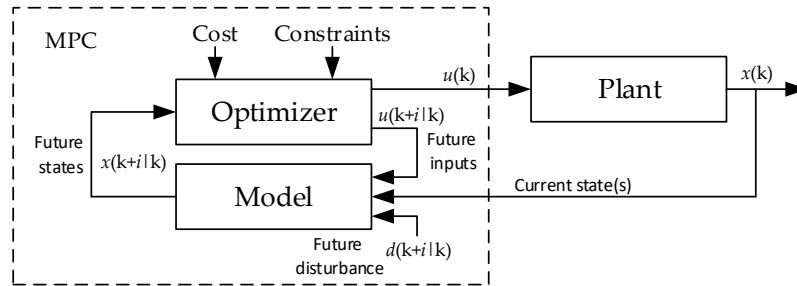


Figure 1.9: A block diagram of a MPC scheme.

The number of design variables in the optimisation problem, for a system with a single input, is determined by the horizon length. The computational demand of MPC is higher compared to other WPEAs as an optimisation problem is to be solved at every time step. As a consequence, the models used for MPC are often relatively simple to reduce the computational demand.

MPC has been applied for WEC systems in papers such as [10][11][12]. In the papers linear MPC with continuous control inputs is applied. It is shown that the MPC scheme can potentially perform better than the reactive control scheme with respect to harvested energy. In [12] a MPC scheme developed for the Wave Star WEC is presented assuming that the PTO force can take continuous values. Here it was shown that the MPC was able to harvest more energy than the commonly used reactive controller in a wide range of sea states. Even when the future wave is estimated and not fully known the MPC showed better performance than the reactive controller. In [12] it is further shown that the losses in the PTO transmission needs to be modelled properly and included in the MPC cost function to increase the harvested energy.

In found literature MPC for WEC systems is only carried out for continuous control inputs. The PTO system of the Wave Star test bench may only apply discrete forces on the float arm. To take this into account discrete control inputs needs to be implemented in the MPC which makes the optimisation problem a discrete variable optimisation problem. Discrete optimisation problems are in general known of being harder to solve than continuous problems which may complicate MPC for the Wave Star WEC. As a consequence, MPC with discrete control inputs may need to compromise between the complexity of the model and the computational power available. Feasibility of MPC algorithms for WEC systems with a discrete fluid power PTO system still needs to be investigated.

MPC applied for a system with quantized inputs is performed in [13]. Here a pneumatic clutch actuator is controlled by using on/off valves. The scheme is a system with quan-

tized input in the sense that the on/off valves are either fully opened or closed. Fast dynamics of the systems requires a fast solution of the MPC algorithm, why an Explicit MPC (EMPC) method is used. EMPC is based on computing the solution to the optimisation problem offline for every expected operating point. The solution is then used to compute the control input as an explicit function of the states and reference, why solving an online optimisation problem is avoided. To be applicable for a WEC, a complete solution to all possible future wave elevations is required. Due to the inherently stochastic behaviour of ocean waves, this seems impractical, why it is assumed that EMPC is not suitable as WPEA. Arbitrary wave elevations should be incorporated in the MPC, why an online solving of the optimisation algorithm seems unavoidable.

In most literature MPC is only investigated from a theoretical point of view and not implemented in practice why this still may be a topic of interest. Some experimental evaluation of MPC applied as WPEA is reported in [14]. Here a nonlinear MPC scheme is applied for a scale version of a point absorber WEC with a permanent magnet linear generator in the PTO stage. The MPC algorithm is solved offline for a pre-recorded wave time series, and the solution is then applied in a wave tank for the same wave time series. However the used PTO system allows for continuous control variables. Especially when using discrete control inputs it may be interesting to investigate if MPC may be practically implemented for a fluid power system such as the Wave Star WEC, as a discrete variable optimal control problem is to be solved online at each time step. This thesis will address MPC with discrete control inputs for a discrete fluid power system. Both development of the MPC scheme and the implementation will be done as a preliminary feasibility analysis of MPC for discrete fluid power systems.

2 | Problem Statement

Based on a literature review the most used WPEA is determined as the reactive control scheme. However, literature suggest that MPC is an attractive algorithm for wave power extraction and may potentially outperform reactive control in terms of energy harvested by the WEC. Effort in utilizing discrete fluid power systems has been successfully done and it has been shown that the overall PTO efficiency can be increased using discrete fluid power systems compared to conventional fluid power. The combination of MPC and a discrete fluid power system seems to combine the identified advantages of high wave energy conversion potential and high PTO efficiency. Hence the problem statement is formulated as:

“How may a Model Predictive Control scheme be formulated and implemented for a discrete displacement hydraulic power take-off system?”

2.1 Project Scope

The main focus of this thesis is divided into sub-problems as elaborated below:

- Formulation of a MPC algorithm suitable for a discrete displacement hydraulic PTO system.
- Implementation of the MPC algorithm for online computation. Analysis of needed model complexity and development of efficient discrete variable optimisation algorithm.
- Practical performance evaluation of the MPC with respect to the common reactive control scheme.

To answer the problem statement a solution strategy is formulated and is elaborated below.

2.2 Solution Strategy

To test MPC of a discrete displacement hydraulic PTO system the test bench located at Aalborg University described in Section 1.1.3 is used as a case study to evaluate MPC experimentally. The sub objectives that needs to be solved to answer the problem formulation are listed below:

- **Absorber and Test Bench Model**
To test and design a MPC scheme a model of the PTO system is developed. The model will be of suitable complexity to capture dominating dynamics of the system and is to be validated with experimental data. A linear model of the Wave Star point absorber and a non-linear model of the PTO system and test bench is to be presented. A model of the test bench is developed in order to validate the model of the PTO cylinder. Losses in the PTO cylinder are identified and included in the model and a comparison between simulated and measured PTO efficiency is to be performed. The losses are to be incorporated in the MPC formulation.
- **Formulation of the MPC & Parameter Study**

The control law for the MPC strategy will be formulated based on the linear point absorber model. An appropriate MPC formulation should be chosen to allow maximisation of harvested energy over a finite time horizon. An analysis of MPC parameters is done with respect to the harvested energy. Suitable sample time and horizon length is to be chosen as these values heavily influence the performance of the MPC, but also the computational load. The analysis is based on model simulations. A wave forecasting scheme is formulated as well, and the significance of wave forecasting accuracy is to be addressed.

- **Choice of Optimisation Algorithm**

Different optimisation algorithms able of handling discrete variables are to be compared, and tested subject to different model complexities. The goal is to develop an efficient MPC algorithm suitable for real time implementation, why fast convergence of the MPC algorithm is necessary. A test scenario is formulated where the true optimum is known. The performance of the optimisation algorithms are evaluated based on convergence time and sensitivity to initial starting point. The computational time of the optimisation algorithm should be minimised to run the MPC online.

- **MPC Performance Evaluation**

Once a suitable formulation of the MPC algorithm is chosen, the MPC performance is evaluated in terms of harvested energy subject to model complexity and time horizon. The evaluation is performed by simulations. This eliminates practical limitations such as limited computational power, why the significance of horizon length and MPC sample time may be studied fully. The evaluation allows for preliminary indications regarding suitable time horizon and model complexity and general MPC feasibility.

- **Experimental Evaluation**

The designed MPC will be implemented on the test bench for experimental evaluation. For the implementation, computational time and other practical challenges should be considered and solved. After implementing the control strategy at the test bench an experimental evaluation will be performed to evaluate the performance of MPC and compare it to the reactive control scheme.

3 | System Model

In this chapter a model of the Wave Star WEC system is derived. The system considered is a single point absorber of the Wave Star C5 prototype which is sketched in Figure 3.1. The model will be used to develop and test MPC algorithms. The system consists of a point absorber attached to an arm connected to a hydraulic cylinder noted as the PTO cylinder as shown in Figure 3.1. The model will describe the dynamics of the absorber, the PTO cylinder and losses in the PTO system. As MPC algorithms are to be implemented and tested on the PTO test bench described in Section 1.1.3, a model of the test bench is derived. This enables the possibility of validating the PTO cylinder model, and further to use the model for MPC feasibility studies. Thus both an absorber model and a test bench model are derived.

3.1 Absorber Model

In this section a model of the C5 Wave Star point absorber is derived. A sketch of the point absorber along with relevant definitions are shown in Figure 3.1.

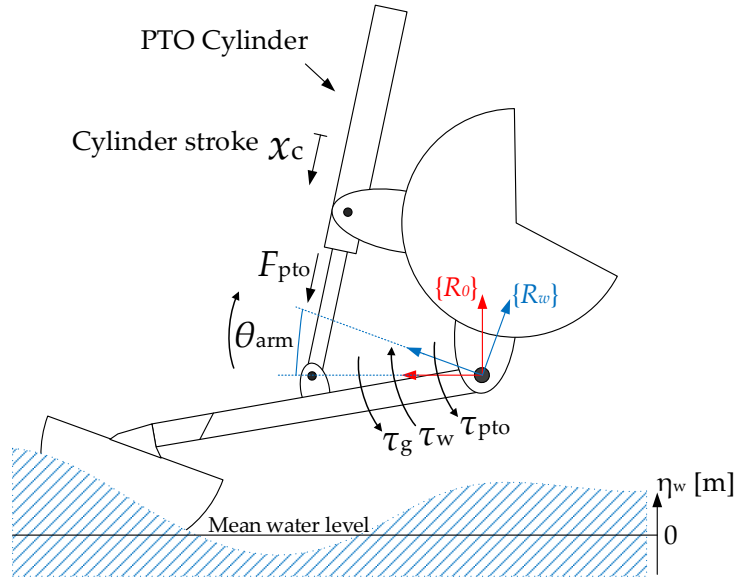


Figure 3.1: Sketch of the Wave star C5 point absorber.

The point absorber are modelled as one rigid body as shown below:

$$J_{tot}\ddot{\theta}_{arm} = \tau_{wave} - \tau_{pto} - \tau_g \quad (3.1)$$

Where J_{tot} is the total moment of inertia of the float and float arm, $\ddot{\theta}_{arm}$ the angular acceleration of the float arm, τ_{wave} the moment applied by the wave on the absorber, τ_g the moment due to gravity and τ_{pto} the moment applied by the PTO cylinder. The different terms in Equation (3.1) will be described in the following sections.

3.1.1 Float and wave interaction

A model of the float and wave interaction of the C5 point absorber using linear wave theory has been derived in [15]. The following model is based on this work. The float and wave interaction may be described by three different effects:

- Excitation torque
- Buoyancy torque
- Radiation torque

To describe the excitation torque produced by the incoming waves a model of the waves is necessary. To reproduce realistic ocean waves, a model based on filtering Gaussian white noise is used. The underlying assumption of the model is that the incoming waves may be given by a Power Spectral Density (PSD). By some general characteristics of the incoming wave, the PSD of the waves may be approximated by the Pierson-Moskowitz (PM) spectrum given in Equation (3.2). For a single sided spectrum the parameters A and B may be given by the significant wave height H_m and the wave peak period T_{wp} as given in Equation (3.3) and (3.4)[16]. Given the parameters H_m and T_{wp} , the average power in the wave at a specific frequency may be described. The significant wave height is the mean height of the one-third highest waves of the desired wave signal. The peak period is the wave period where the most power is concentrated[9]. To generate a wave signal with the desired PSD a filter may be designed such that the output of the filter, with Gaussian white noise as input, has the desired PSD. Such a filter has been provided for this thesis and referred to as “wave generator”. A wave may then be generated based on the wave characteristics H_m and T_{wp} . Different sea states(SS) are defined by different values of H_m and T_{wp} . The PM spectrum for three sea states are shown in Figure 3.2.

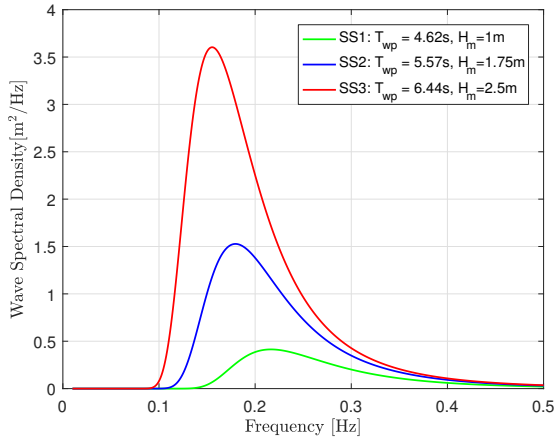


Figure 3.2: PM spectra for different sea states.

$$S(f) = \frac{A}{f^5} e^{\frac{-B}{f^4}} \quad (3.2)$$

$$A = \frac{1}{4} B H_m^2 \quad (3.3)$$

$$B = \frac{5}{4} \frac{1}{T_{wp}^4} \quad (3.4)$$

The excitation torque is defined as the torque applied to the float arm, from the incoming wave, for the float arm being fixed in neutral position, where the neutral position is defined as the position of the point absorber in calm water. The wave torque is derived from the pressure acting on the surface of the submerged float. In [15] the fluid mechanics involved with this process is solved using a numerical wave simulation tool. From this a force filter is derived as $\frac{\tau_{ext}(s)}{\eta_w(s)}$, where η_w is the wave height. The force filter has been

provided for this thesis. For an irregular wave profile shown in Figure 3.4, with significant wave height H_m and peak wave period T_{wp} , the corresponding excitation torque on the float arm derived from the force filter is shown in lower Figure of 3.4.

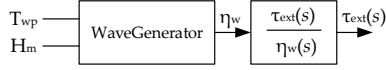


Figure 3.3: Diagram of the excitation torque computation, given H_m and T_{wp} .

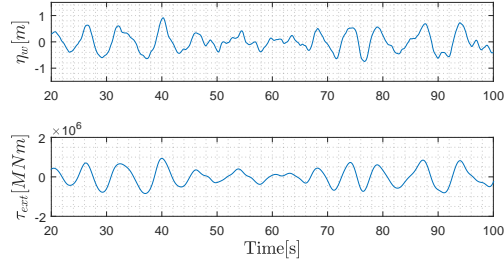


Figure 3.4: Wave height profile and corresponding wave excitation torque.

The buoyancy torque may be derived from Archimedes' principle which states that a body submerged in a fluid is exerted to a force in an upwards direction equal to the mass of the displaced fluid. The buoyancy torque for the point absorber may be described by the non-linear function $\tau_b(\theta_{arm})$:

$$\tau_b(\theta_{arm}) = V_{sub}(\theta_{arm})\rho_{water} g d_a(\theta_{arm}) \quad (3.5)$$

Where V_{sub} is the volume of the submerged part of the float, ρ_{water} is the density of water, g is the gravitational constant and d_a is the moment arm of the float arm. The hydrostatic restoring torque may be defined as the balance between the buoyancy torque and the gravitational torque as:

$$\tau_{res} = \tau_b - \tau_g \quad (3.6)$$

Assuming calm water, τ_{res} may be linearised in the position where $\tau_b = \tau_g$, hence the restoring torque may be described as:

$$\Delta\tau_{res} \approx \left. \frac{\partial\tau_{res}}{\partial\theta} \right|_{\theta_{arm}=0} \Delta\theta_{arm} = -k_{res}\theta_{arm} \quad (3.7)$$

Thus the linearised restoring torque may be seen as an equivalent spring effect from the buoyancy and gravitational torque, where the spring constant may be found as: $k_{res} = \rho_{water} g d_a(\theta) A_w$, where A_w is the cross sectional area of the submerged float in the water surface level[15].

The radiation torque is the torque applied to the float due to waves being radiated from the motion of the float. The radiation torque due to waves being radiated in calm water may be described by an inertia term and a convolution term as:

$$\tau_{rad} = -J_{\infty}\ddot{\theta}_{arm} - k_r(t) * \omega_{arm} \quad (3.8)$$

The inertia term may be seen as an additional mass added to the point absorber due to the water around the float is accelerated when the float is in motion. $k_r(t)$ is the impulse response from the absorber velocity to the radiation torque. In [15], $k_r(t) * \omega_{arm}$ is approximated by a 5th order transfer function given as:

$$\frac{\tau_{rad,kr}(s)}{\omega_{arm}(s)} = K_r(s) = \frac{b_0 s^5 + \dots + b_4 s + b_5}{s^5 + \dots + a_4 s + a_5} \quad (3.9)$$

Thus the torque equilibrium of the point absorber may be stated as:

$$J_{\text{tot}}\ddot{\theta}_{\text{arm}} = \tau_{\text{ext}} - k_{\text{res}}\theta_{\text{arm}} - J_{\infty}\ddot{\theta}_{\text{arm}} - \tau_{\text{rad,kr}} - \tau_{\text{pto}}$$

$$\Updownarrow$$

$$\ddot{\theta}_{\text{arm}} = \frac{1}{J_{\text{tot}} + J_{\infty}} (\tau_{\text{ext}} - k_{\text{res}}\theta_{\text{arm}} - \tau_{\text{rad,kr}} - \tau_{\text{pto}})$$

By transforming Equation (3.9) to observable canonical form the system may be represented on state space form with the arm position as output:

$$\underbrace{\begin{bmatrix} \ddot{\theta}_{\text{arm}} \\ \dot{\theta}_{\text{arm}} \\ \tau_{\text{rad,kr}} \\ \dot{x}_{\text{kr},1} \\ \dot{x}_{\text{kr},2} \\ \dot{x}_{\text{kr},3} \\ \dot{x}_{\text{kr},4} \end{bmatrix}}_{\mathbf{\dot{x}}} = \underbrace{\begin{bmatrix} 0 & \frac{-k_{\text{res}}}{J_{\text{tot}}+J_{\infty}} & \frac{-1}{J_{\text{tot}}+J_{\infty}} & 0 & 0 & 0 & 0 \\ 1 & 0 & 0 & 0 & 0 & 0 & 0 \\ b_1 - a_1 b_0 & 0 & -a_1 & 1 & 0 & 0 & 0 \\ b_2 - a_2 b_0 & 0 & -a_2 & 0 & 1 & 0 & 0 \\ b_3 - a_3 b_0 & 0 & -a_3 & 0 & 0 & 1 & 0 \\ b_4 - a_4 b_0 & 0 & -a_4 & 0 & 0 & 0 & 1 \\ b_5 - a_5 b_0 & 0 & -a_5 & 0 & 0 & 0 & 0 \end{bmatrix}}_{\mathbf{A}} \underbrace{\begin{bmatrix} \dot{\theta}_{\text{arm}} \\ \theta_{\text{arm}} \\ \tau_{\text{rad,kr}} \\ x_{\text{kr},1} \\ x_{\text{kr},2} \\ x_{\text{kr},3} \\ x_{\text{kr},4} \end{bmatrix}}_{\mathbf{x}} + \underbrace{\begin{bmatrix} \frac{1}{J_{\text{tot}}+J_{\infty}} \\ 0 \\ 0 \\ 0 \\ 0 \\ 0 \\ 0 \end{bmatrix}}_{\mathbf{B}} \underbrace{(\tau_{\text{ext}} - \tau_{\text{pto}})}_{\mathbf{u}} \quad (3.10)$$

$$y = \mathbf{C}\mathbf{x} = [0 \ 1 \ 0 \ 0 \ 0 \ 0 \ 0] \mathbf{x} \quad (3.11)$$

The frequency response of the point absorber from the resulting torque \mathbf{u} to the arm position θ_{arm} is shown in Figure 3.5. The resonance frequency of the point absorber is found to 0.285Hz, thus having a natural period of approximately 3.5s.

$k_{\text{res}} = 14 \cdot 10^6$	$\left[\frac{\text{Nm}}{\text{rad}} \right]$	$a_5 = 9184$
$J_{\text{tot}} = 2.46 \cdot 10^6$	$[\text{kgm}^2]$	$b_0 = 0$
$J_{\infty} = 1.32 \cdot 10^6$	$[\text{kgm}^2]$	$b_1 = 14 \cdot 10^6$
$a_1 = 93$		$b_2 = 62.3 \cdot 10^7$
$a_2 = 1665$		$b_3 = 8.156 \cdot 10^9$
$a_3 = 6305$		$b_4 = 1.3143 \cdot 10^{10}$
$a_4 = 13277$		$b_5 = 1.4359 \cdot 10^9$

Table 3.1: Model parameter values used to model the point absorber [15].

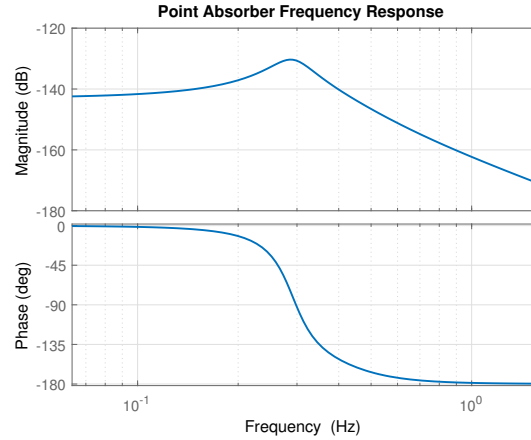


Figure 3.5: Frequency response of Equation (3.10) with the arm position θ_{arm} as output.

The torque applied by the PTO system is described in the following section starting with the absorber and cylinder kinematics.

3.1.2 Absorber and Cylinder Kinematics

The moment applied by the PTO cylinder is dependent on the force applied by the cylinder and the moment arm which is varying with θ_{arm} . The relation between the cylinder stroke and the float arm angle may be described by geometric relations. Relevant definitions of the geometry are shown in Figure 3.6 with the used geometric constants are listed to the right.

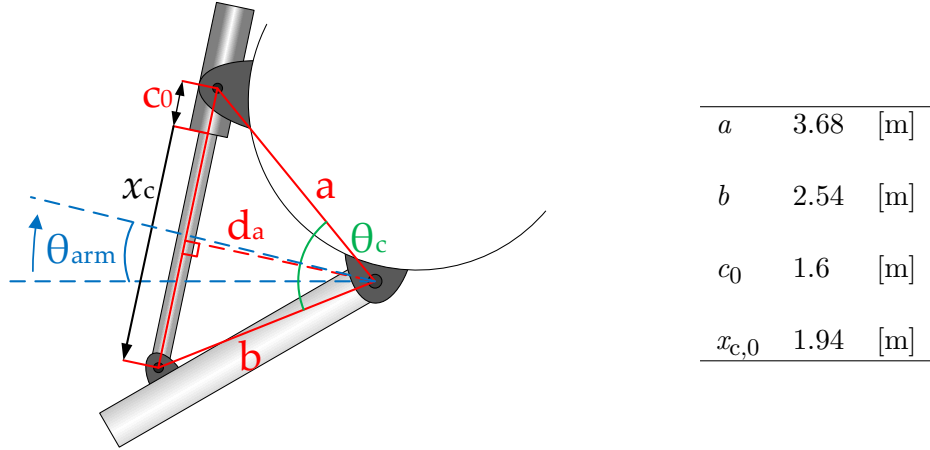


Figure 3.6: Geometric sketch of float arm and PTO cylinder.

θ_{arm} is defined as the angular displacement away from the neutral position, hence $\theta_{\text{arm}} = 0$ in calm ocean level. From Figure 3.6 the geometric relation between the angle of the float arm, θ_{arm} , and the cylinder stroke, x_c , may be stated as:

$$x_c = \sqrt{a^2 + b^2 - 2ab \cos(\theta_c)} - c_0 \quad (3.12)$$

Where θ_c is defined as:

$$\theta_c = \theta_{c,0} - \theta_{\text{arm}} \quad (3.13)$$

Where $\theta_{c,0}$ is the angle of θ_c when $\theta_{\text{arm}} = 0$ described by the cosine relation:

$$\cos(\theta_{c,0}) = \frac{a^2 + b^2 - (c_0 + x_{c,0})^2}{2ab} \quad (3.14)$$

Where $x_{c,0}$ is the cylinder stroke at $\theta_{\text{arm}} = 0$. The moment arm, d_a , may be stated as shown below:

$$d_a = \frac{ab \sin(\theta_c)}{x_c + c} \quad (3.15)$$

The cylinder stroke and moment arm as function of the arm angle θ_{arm} are shown in Figure 3.7 and 3.8 respectively.

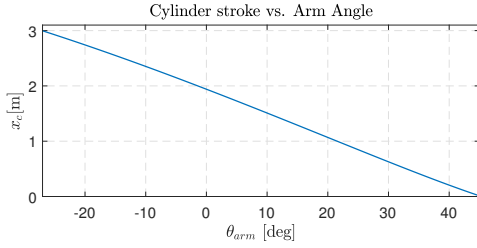


Figure 3.7: Cylinder stroke as function of the arm angle.

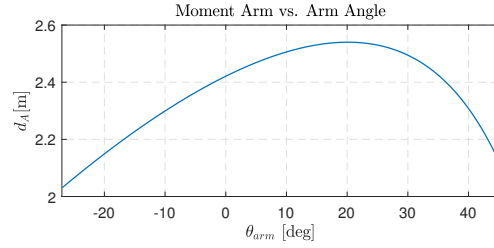


Figure 3.8: Moment arm as function of the arm angle.

The Wave Star WEC is designed with a cylinder stroke of 3m, where only 2m of the stroke, centred around $x_c = 2m$, is used in power production. Retraction to a stroke of 0m is performed in extreme sea states as a storm protection. As the DDC utilized on the AAU PTO test bench only has a stroke of 2m, the relation given in Equation (3.12) is shifted 1m, such that a neutral position results in a cylinder stroke of 1m. The torque applied by the PTO cylinder on the float arm may then be described as:

$$\tau_{pto} = d_a(\theta_{arm})F_{pto} \quad (3.16)$$

Where F_{pto} is the resulting force from the PTO cylinder described in the following section.

3.2 PTO Model

The PTO system consists of a multi chamber cylinder, a primary side consisting of a valve manifold switching the pressure in each chamber between three pressure levels supplied by the secondary side. The pressure in each chamber is determined by controlling three DFCUs connected to each pressure line giving nine DFCUs in total. A diagram of the hydraulic PTO system can be seen in Figure 3.9. For simplicity the secondary side is considered ideal, hence the line pressures are assumed constant.

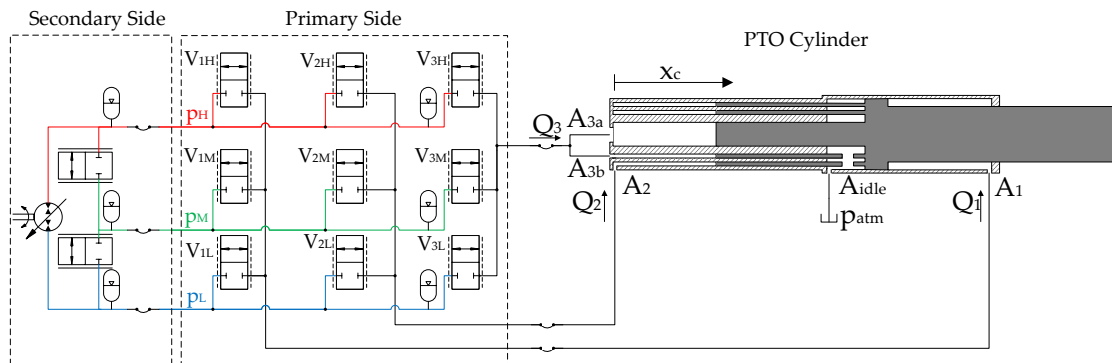


Figure 3.9: Hydraulic diagram of PTO system containing valve manifold and multi chamber cylinder.

The cylinder used in the PTO system is shown in Figure 3.10 where a cross sectional view is shown. As seen the cylinder has five chambers where one is vented to atmospheric pressure. Chamber 3a and 3b are considered as one single chamber as they are operated in parallel as shown in Figure 3.9.

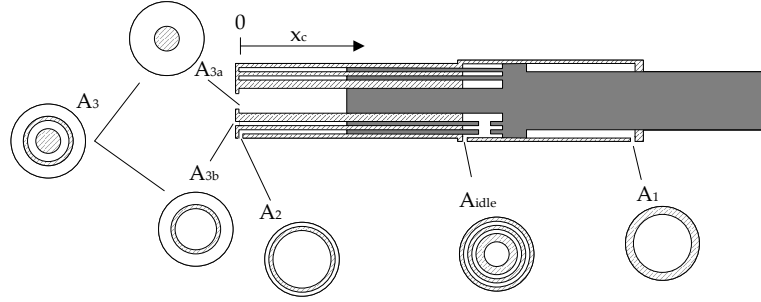


Figure 3.10: Sketch of the multi chamber cylinder used in the PTO system.

Disregarding friction force the resulting force, defined positive in the x-direction, applied by the cylinder may be described as a sum of the forces from each chamber as shown below:

$$F_{pto} = -p_1 A_1 + p_2 A_2 + p_3 A_3 + P_{atm} A_{idle} \quad (3.17)$$

Where P_{atm} is atmospheric pressure and p_i is the pressure in the i 'th cylinder chamber.

As the pressure of the three PTO cylinder chambers can obtain three different pressure levels a total of 27 forces is available. In Figure 3.11 the 27 different force levels and the corresponding valve configuration are shown, with a high pressure of 180bar, a medium pressure of 100bar and a low pressure of 20bar.

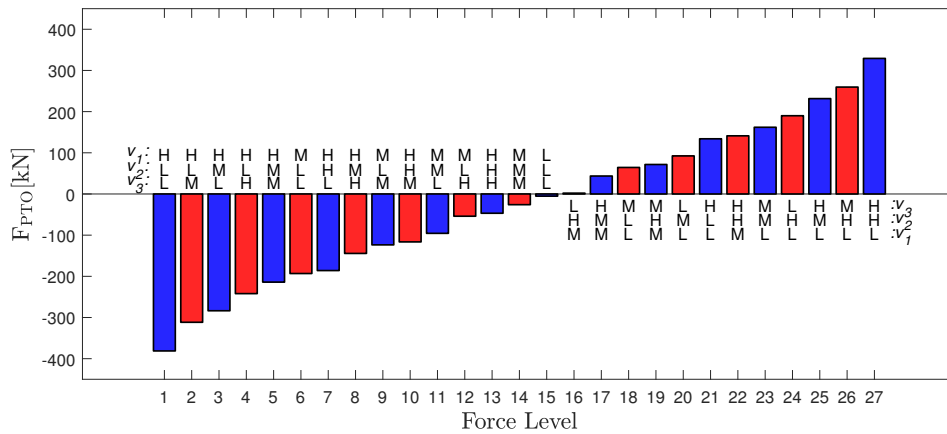


Figure 3.11: 27 possible force levels and corresponding force applied by the PTO cylinder.

In Figure 3.11 the state of each chamber $\{v_1, v_2, v_3\}$ is denoted with a capital letter $\{H, M, L\}$ indicating which pressure line the chamber is connected to.

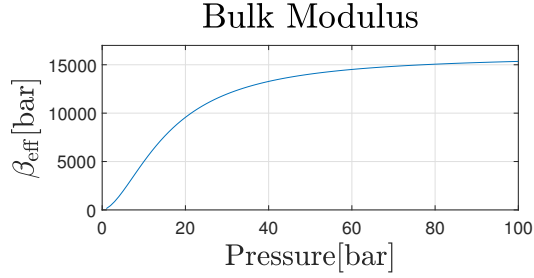
The pressure inside each chamber of the PTO cylinder may be described by the continuity equation as shown below for each chamber assuming no leakage:

$$\dot{p}_1 = (Q_1 + v_c A_1) \frac{\beta(p_1)}{V_{0,1} - x_c A_1} \quad (3.18)$$

$$\dot{p}_2 = (Q_2 - v_c A_2) \frac{\beta(p_2)}{V_{0,2} + x_c A_2} \quad (3.19)$$

$$\dot{p}_3 = (Q_3 - v_c A_3) \frac{\beta(p_3)}{V_{0,3} + x_c A_3} \quad (3.20)$$

Where β is the effective bulk modulus, v_c is the cylinder velocity, x_c the stroke of the cylinder, A_i the piston area of the chambers, $V_{0,i}$ is the volume of the chambers for $x_c = 0$, Q_i the flow into the chambers where the subscript i indicates the cylinder chamber. The cylinder stroke is defined in positive direction as shown in Figure 3.10 with $x_c = 0$ at the end stop of the cylinder. The effective bulk modulus is modelled as shown below assuming the stiffness of the fluid sufficiently higher than the stiffness of air.



$$\beta(p) = \frac{1}{\frac{1}{\beta_F} + \frac{\varepsilon_A}{\beta_A}} \quad (3.21)$$

$$\varepsilon_A(p) = \left(\frac{p_{\text{atm}} \varepsilon_A(p_{\text{atm}}) C_{\text{ad}}}{p} \right)^{\frac{1}{C_{\text{ad}}}} \quad (3.22)$$

Figure 3.12: Bulk modulus model with $\beta_F = 16000$ [bar] and $\varepsilon_A(p_{\text{atm}}) = 0.01$.

Where β_F is the stiffness of the pure fluid, $\beta_A = C_{\text{ad}} \cdot p$ the stiffness of air and ε_A the volumetric ratio of free air in the fluid found from Equation (3.22). The parameter β_F also represents the maximum value of Equation (3.21). The value is used as a soft parameter to compensate for model uncertainties and finite hose stiffness, and will be used to fit the model with experimental measurements.

Each DFCU consists of multiple on/off valves as shown in Figure 3.13.

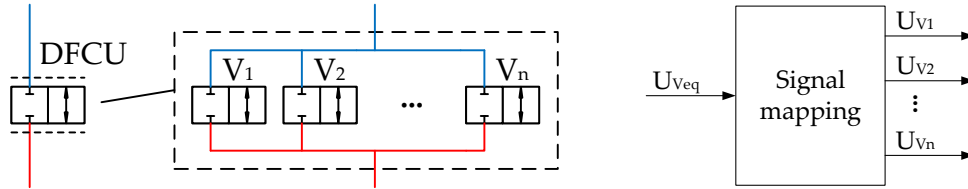


Figure 3.13: Visualisation of DFCU consisting of multiple on/off valves.

The flow through each DFCU shown in Figure 3.9 is modelled as one equivalent valve by the orifice equation shown below:

$$Q_{ij} = n_i k_v x_{v,ij} \sqrt{|p_j - p_i| \text{sign}(p_j - p_i)} \quad \begin{array}{l} i = \{1, 2, 3\} \\ j = \{H, M, L\} \end{array} \quad (3.23)$$

Where the subscript i and j represent the corresponding cylinder chamber and pressure line respectively. x_v is the equivalent valve spool position and is assumed to take continuous values. The number of valves n_i connecting the i 'th chamber are $n_1 = 18$, $n_2 = 10$, $n_3 = 8$. The on/off valves used in the DFCUs are of the WS22GDA series manufactured by Bucher Hydraulics. The valve gain k_v is a fitted value found from measured flow characteristics provided by Bucher Hydraulics. The k_v value used is the average of two calculated valve gains depending on the flow direction through the valve and is found to

be approximately $1 \cdot 10^{-6} \left[\frac{m^3/s}{\sqrt{Pa}} \right]$.

The opening of the DFCUs are controlled such the pressure development in the chambers follows a chosen pressure trajectory. To achieve this the valve opening trajectories are based on an algorithm described in [7]. The valve opening trajectories used are not included in the modelling of the PTO cylinder, but are included when considering losses in the PTO transmission and for design of the MPC. For simplicity the valve opening is modelled by a ramp function defined by a opening time, T_v as shown below:

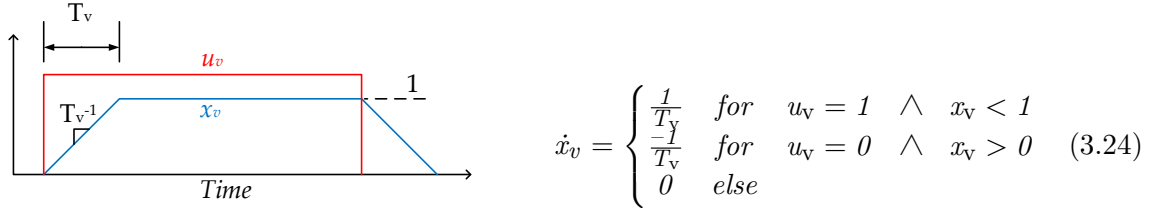


Figure 3.14: Sketch of the valve opening.

Where x_v is the normalised equivalent opening of the DFCU and u_v the control input for the DFCU being either one or zero. The opening of the DFCUs is timed such one valve is closed before another is opened to avoid short circuiting two pressure lines. The timing of a pressure shift from medium to high pressure is sketched in the figure below:

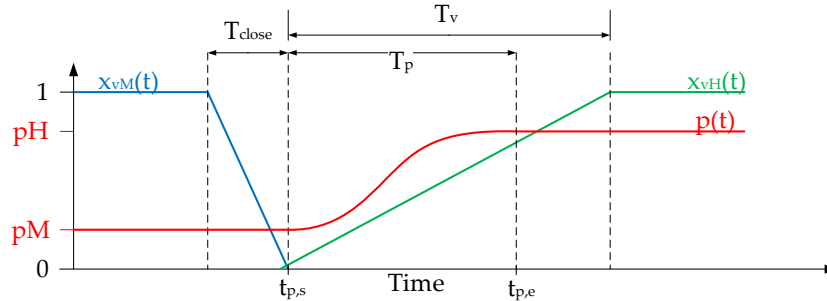


Figure 3.15: Sketch of the valve timing with pressure development indicated.

The closing time, T_{close} , for the valves are chosen as fast as possible to reduce shifting time. The valve bandwidth allows for a closing time of approximately 12ms. The opening time, T_v , are chosen as a compromise between rise time of the pressure and the oscillations of the pressure. The time T_p indicates the time of the pressure development.

3.2.1 Transmission Line Model

The pressure line dynamics are expected to be excited by the fast switching of the valves why the line dynamics are included in the model. The transmission line is modelled by dividing the hose into n elements as shown in Figure 3.16.

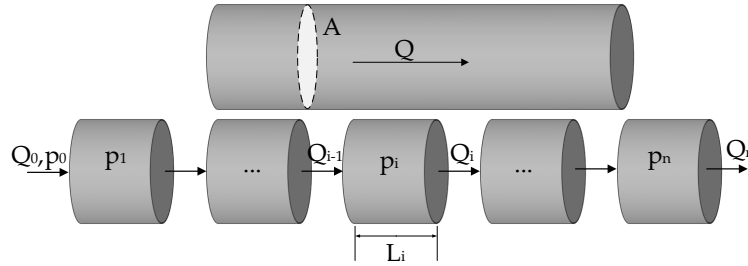


Figure 3.16: Model of a transmission line.

The flow dynamics may then be described by the momentum equation assuming each hose element as a single mass as shown below, neglecting, pressure losses in the hoses:

$$\dot{Q}_i = (p_i - p_{i+1}) A_i \frac{1}{\rho L_i} \quad \forall i = 1, 2, \dots, n \quad (3.25)$$

The pressure dynamics for the i^{th} line element may be described by the continuity equation shown below:

$$\dot{p}_i = (Q_{i-1} - Q_i) \frac{\beta_i(p_i)}{A_i L_i} \quad \forall i = 1, 2, \dots, n \quad (3.26)$$

Q_0 is the combined flow from the valves into the respective transmission line and p_{n+1} is the pressure in the respective cylinder chamber. The bulk modulus for each element is modelled as shown in Equation (3.21).

3.3 Test Bench Model

A model of the test bench is used to validate the PTO cylinder model. The test bench consists of the PTO system and a wave emulator system used to emulate the motion of the float arm. The wave emulator system consists of a symmetrical cylinder controlled by two proportional valves in parallel as shown in Figure 3.17. A control algorithm generates inputs for each valve from a wave reference and the force applied from the PTO cylinder to emulate the motion of the float arm. The control is developed in [8] and will be used to test control strategies on the test bench.

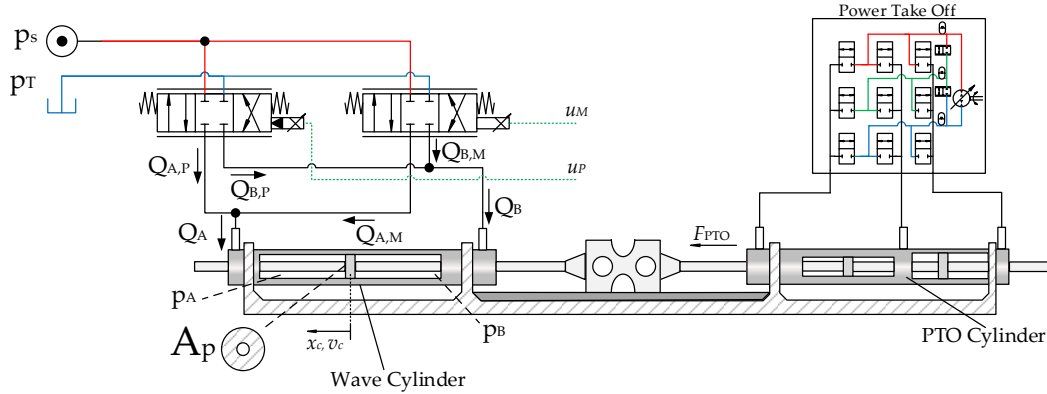


Figure 3.17: Overview of the PTO test bench at AAU.

The motion of the wave cylinder piston may be described as shown below:

$$\ddot{x}_c = \frac{(p_B - p_A)A_p - F_{\text{fric}}(v_c) + F_{\text{pto}}}{m_{\text{tot}}} \quad (3.27)$$

Where A_p is piston area of the wave cylinder, m_{tot} is the total mass and p_A and p_B are the pressure inside chamber A and B of the wave cylinder. The total friction force is modelled by coulomb, viscous and stribek friction as shown below:

$$F_{\text{fric}}(v_c) = \left(B_s e^{-\frac{|v_c|}{\alpha}} + B_v |v_c| + K_c \right) \tanh\left(\frac{v_c}{\gamma}\right) \quad (3.28)$$

Where B_s is a stribek friction coefficient, B_{fric} a viscous friction coefficient, K_c a Coulomb friction coefficient and γ a coefficient determining the rate of change around zero. In Figure 3.18 the friction force as a function of cylinder piston velocities may be seen with the friction coefficients to the right found from an earlier semester project[17].

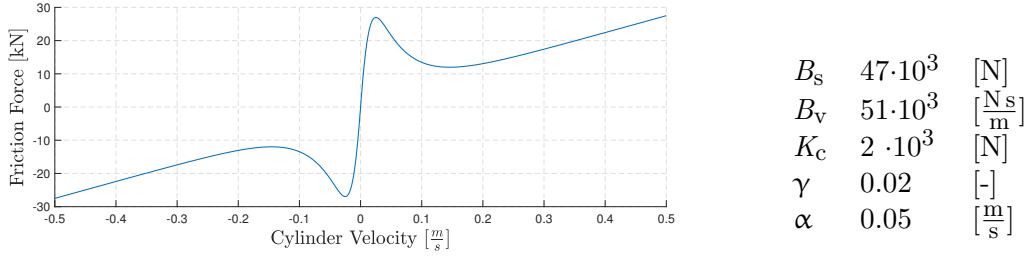


Figure 3.18: Friction force as a function of cylinder velocity.

The wave cylinder chamber pressure dynamics are modelled as:

$$\dot{p}_A = (Q_A + v_c A_p + (p_B - p_A) C_{il}) \frac{\beta_A}{V_{A,0} - x_c A_p} \quad (3.29)$$

$$\dot{p}_B = (Q_B - v_c A_p - (p_B - p_A) C_{il}) \frac{\beta_B}{V_{B,0} + x_c A_p} \quad (3.30)$$

Where the effective bulk modulus, β , is modelled as shown in Equation (3.21). The dead volumes $V_{0,A}$ and $V_{0,B}$ are defined as the chamber and hose volume when the cylinder piston is in centre position. C_{il} is an internal leakage coefficient. The dynamics of the transmission line from pump to valve manifold is neglected. The valves used are a Parker servo valve(D111FP NG32) and a Moog servo valve(D634-P) where the Parker valve is used as the main operating valve and the Moog is utilized at lower flow demands. The combined flow from the two valves into the chambers of the wave cylinder may be described as shown below:

$$Q_A = Q_{A,P} + Q_{A,M} \quad (3.31)$$

$$Q_B = Q_{B,P} + Q_{B,M} \quad (3.32)$$

Where the subscript P and M indicates which valve is providing the flow. Each flow may be described by the orifice equation shown below:

$$Q_{A,P} = \begin{cases} k_{v,P}(x_{v,P}) \sqrt{|P_s - p_A|} \text{sign}(P_s - p_A) & \text{for } x_{v,P} \geq 0 \\ k_{v,P}(x_{v,P}) \sqrt{|p_A - P_T|} \text{sign}(p_A - P_T) & \text{for } x_{v,P} < 0 \end{cases} \quad (3.33)$$

$$Q_{A,M} = \begin{cases} k_{v,M}(x_{v,M}) \sqrt{|P_s - p_A|} \text{sign}(P_s - p_A) & \text{for } x_{v,P} \geq 0 \\ k_{v,M}(x_{v,M}) \sqrt{|p_A - P_T|} \text{sign}(p_A - P_T) & \text{for } x_{v,P} < 0 \end{cases} \quad (3.34)$$

$$Q_{B,P} = \begin{cases} k_{v,P}(x_{v,P}) \sqrt{|P_s - p_B|} \text{sign}(P_s - p_B) & \text{for } x_{v,M} \geq 0 \\ k_{v,P}(x_{v,P}) \sqrt{|p_B - P_T|} \text{sign}(p_B - P_T) & \text{for } x_{v,M} < 0 \end{cases} \quad (3.35)$$

$$Q_{B,M} = \begin{cases} k_{v,M}(x_{v,M}) \sqrt{|P_s - p_B|} \text{sign}(P_s - p_B) & \text{for } x_{v,M} \geq 0 \\ k_{v,M}(x_{v,M}) \sqrt{|p_B - P_T|} \text{sign}(p_B - P_T) & \text{for } x_{v,M} < 0 \end{cases} \quad (3.36)$$

Where P_s and P_T is the supply and tank pressure which is assumed constant. $k_{v,P}(x_v)$ and $k_{v,M}(x_v)$ is in an earlier semester project[17] mapped as a function of the valve input which is described in the following subsection.

3.3.1 Valve Modelling

The valve dynamics are modelled by a second order transfer function and a slew rate limiter defining the opening time of the valves. The data sheets for the Parker and the Moog valve indicate a step time for 100% stroke which is used as the rate limit. Further a frequency response for a 5% stroke for the Parker and 10% stroke for the Moog is given which is shown in Figure 3.19 and 3.20.

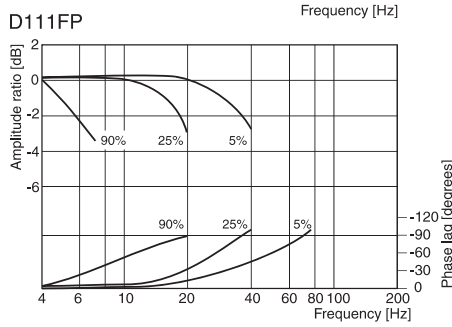


Figure 3.19: Frequency response for Parker valve[18].

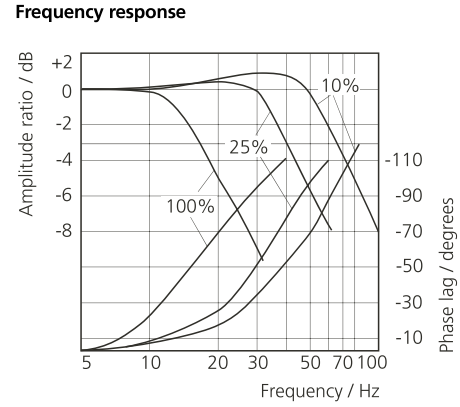


Figure 3.20: Frequency response for Moog valve[19].

The transfer function is chosen as an estimate of the frequency response for a 1% stroke for both valves. In Table 3.2 the coefficients for the Parker and Moog valve are shown.

	$\omega_n [\frac{rad}{s}]$	$\zeta [-]$	Rate Limit [s^{-1}]
Parker Valve	300	0.9	2222%
Moog Valve	550	0.55	4000%

Table 3.2: Valve coefficients for the Parker and Moog valve.

In the figure below the structure of the valve model for both the Parker and Moog valve is illustrated.

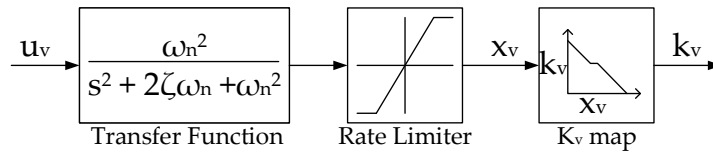


Figure 3.21: Diagram of the valve model.

The k_v map for the Parker and Moog valve is given in Equation (3.37) and (3.38) respectively.

$$k_{v,P} = \begin{cases} (P_1 \sin(P_2 u + P_3) + P_4) \operatorname{sgn}(u) & \text{for } -10 \leq u < -0.95 \wedge 10 \geq u > 0.91 \\ 0 & \text{for } -0.95 \leq u \leq 0.91 \end{cases} \quad (3.37)$$

$$k_{v,M} = M_1 u^5 + M_2 u^4 + M_3 u^3 + M_4 u^2 + M_5 u + M_6, \quad \text{for } -10 \leq u \leq 10 \quad (3.38)$$

The function for the Parker valve is set to 0 between -0.95 and 0.91 due to an overlap of the Parker valve. Both functions are shown in Figure 3.22 and 3.23 and the coefficients for each fit are shown in Table 3.3.

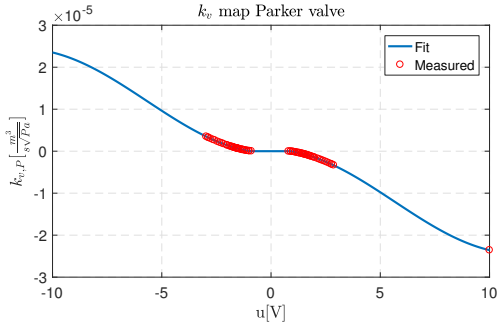


Figure 3.22: k_v map for Parker valve[17].

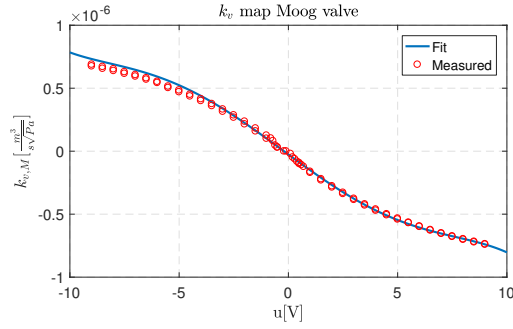


Figure 3.23: k_v map for Moog valve[17].

Parker Fit Coefficients		Moog Fit Coefficients	
$P_1 = 2.57 \cdot 10^{-4}$	$\left[\frac{m^3}{s\sqrt{Pa}} \right]$	$M_1 = -8.98 \cdot 10^{-11}$	$\left[\frac{m^3}{s\sqrt{Pa} V^5} \right]$
$P_2 = 2.77 \cdot 10^{-1}$	$\left[\frac{1}{V} \right]$	$M_2 = -1.15 \cdot 10^{-10}$	$\left[\frac{m^3}{s\sqrt{Pa} V^4} \right]$
$P_3 = 1.58$	$[-]$	$M_3 = 1.89 \cdot 10^{-8}$	$\left[\frac{m^3}{s\sqrt{Pa} V^3} \right]$
$P_4 = -2.49 \cdot 10^{-4}$	$\left[\frac{m^3}{s\sqrt{Pa}} \right]$	$M_4 = 1.48 \cdot 10^{-8}$	$\left[\frac{m^3}{s\sqrt{Pa} V^2} \right]$
		$M_5 = -2.63 \cdot 10^{-6}$	$\left[\frac{m^3}{s\sqrt{Pa} V} \right]$
		$M_6 = -5.36 \cdot 10^{-7}$	$\left[\frac{m^3}{s\sqrt{Pa}} \right]$

Table 3.3: Valve fit coefficients for the Parker and Moog valve[17].

Piston areas of the cylinder, dead volumes of the cylinder along with the remaining parameters used for the model are shown in Table 3.4.

A_1	235	$[\text{cm}^2]$	$V_{0,1}$	48.1	[L]	L_1	4.35	[m]	ε_A	0.01	[%]
A_2	122	$[\text{cm}^2]$	$V_{0,2}$	1.1	[L]	L_2	1.35	[m]	β_F	16e3	[bar]
A_3	87	$[\text{cm}^2]$	$V_{0,3}$	2.3	[L]	L_3	1.69	[m]	C_{ad}	1.4	[-]
A_{idle}	236.4	$[\text{cm}^2]$	$V_{A,0}$	39.6	[L]	A_L	11.4	$[\text{cm}^2]$	m_{tot}	2750	[kg]
A_p	236.4	$[\text{cm}^2]$	$V_{B,0}$	39.6	[L]	ρ	860	$\left[\frac{\text{kg}}{\text{m}^3} \right]$	μ	26e6	[Pa s]

Table 3.4: Valve coefficients for the Parker and Moog valve.

After modelling the system the losses will be considered in the following sections.

3.4 Losses in the PTO Transmission

In this section the losses in the PTO cylinder is investigated. A simple model of the losses is desirable, such that these may be included in the MPC formulation. For a pressure

change in a cylinder chamber, loss associated with fluid compression will be present. A general analysis of the loss in a chamber due to changing the pressure is desired. The analysis is done for both a fixed volume and a changing volume. Throttling losses in the valve manifold is included as well.

3.4.1 Shifting Losses for Fixed Chamber Volume

In Figure 3.24 a sketch of a fixed chamber connected to a pressure source through an orifice is shown.

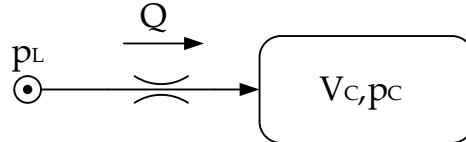


Figure 3.24: Model of a fixed volume connected to a pressure source

The loss due to the compressibility of the fluid is in [7] for a fixed volume stated as:

$$E_{\text{loss},\beta} = \frac{1}{2} \Delta p^2 \frac{V}{\beta} \quad (3.39)$$

Where Δp is the pressure change in the volume, V is the volume and β is the effective bulk modulus assumed constant for this analysis. In general the bulk modulus varies with the fluid pressure but for pressures above 20bar, which is the pressure in the low pressure line, the variation is low. Equation (3.39) may be proven by considering the energy loss as the difference between energy from the pressure line and into the fixed volume as shown below:

$$E_{\text{loss},\beta} = E_{\text{in}} - E_{\text{out}} = \int_0^{\infty} (p_L Q(t)) - \int_0^{\infty} (p_c(t) Q(t)) \quad (3.40)$$

Where E_{in} is the energy from the pressure line, E_{out} is the energy into the volume, p_L is the constant line pressure, p_c the chamber pressure and Q the flow into the cylinder chamber. The amount of flow needed to change the pressure from p_c to p_L may be described by the flow continuity equation:

$$\dot{p}_c = \frac{\beta}{V} Q(t) \quad (3.41)$$

Where β is the effective bulk modulus and is assumed fixed. From Equation (3.41) the pressure of the volume may be described as:

$$p_c = \frac{\beta}{V} \int Q(t) dt + p_{c,0} \quad (3.42)$$

As the pressure in the volum will go towards the line pressure, $\lim_{t \rightarrow \infty} p_c(t) = p_L$, the following may be stated:

$$p_L = \frac{\beta}{V} \int_0^{\infty} Q(t) dt + p_{c,0} \quad (3.43)$$

The volume of flow needed to change the pressure in the volume from p_c to p_L may be described as shown below:

$$V_\beta = \int_0^\infty Q(t) dt = (p_L - p_{c,0}) \frac{V}{\beta} \quad (3.44)$$

Inserting Equation (3.42) and (3.44) into Equation (3.40), Equation (3.39) may be derived. As it can be seen the loss is dependent on the pressure difference squared and the volume of the chamber. In Figure 3.25 a map showing the energy loss for a pressure change in each chamber of the PTO cylinder is shown for a cylinder stroke of $x_c = 1m$.

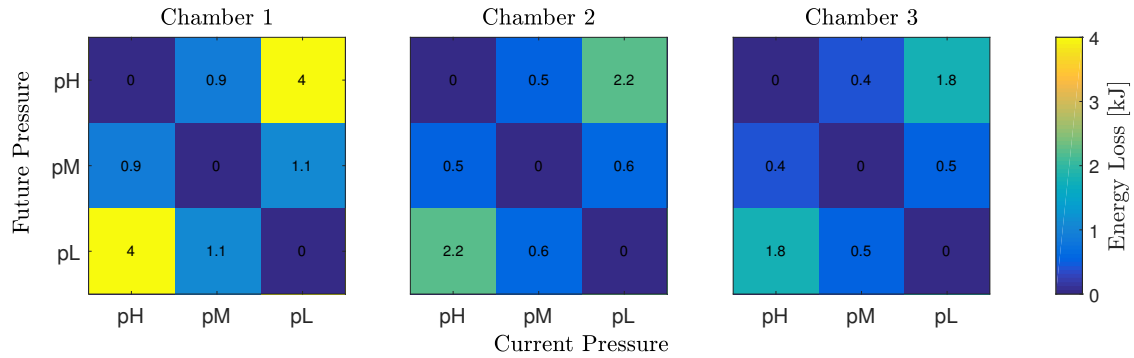


Figure 3.25: Energy loss associated with switching between pressure lines for each chamber at $x_c = 1m$, $pH = 180bar$, $pM = 100bar$, $pL = 20bar$ and $\beta = 10000bar$.

The losses for cylinder chamber one is higher compared to the other chambers. The reason for this is the higher volume of this chamber for the given position. As it can be seen in Equation (3.39) the loss is proportional to the chamber volume. In Figure 3.26 the loss for each chamber as function of the cylinder stroke, for a pressure change from $100[bar]$ to $180[bar]$, is shown.

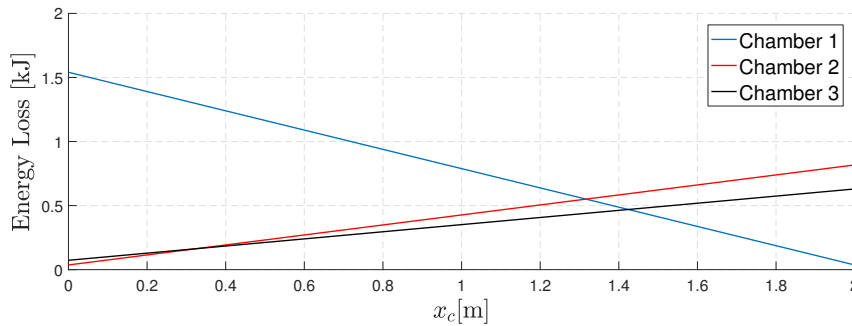


Figure 3.26: Energy loss as a function of the cylinder stroke with $\beta = 10000[bar]$ and $\Delta p = 80[bar]$.

3.4.2 Shifting Losses for Changing Chamber Volume

A changing volume during pressure change is considered, as the effect of a changing volume influences the energy loss. In Figure 3.28 a model of a chamber with changing volume is shown.

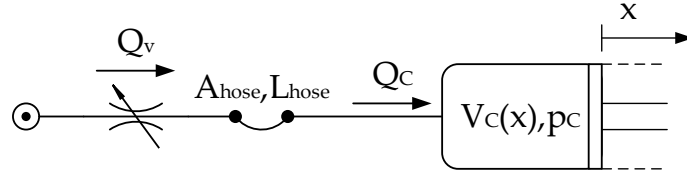


Figure 3.27: Model of a changing volume with a fixed pressure source.

In [7] the energy loss associated with the pressure change for a changing volume is stated as:

$$E_{\text{loss},\beta} = \frac{1}{2}\Delta p^2 \frac{V}{\beta} + \frac{1}{2}\Delta p \dot{V} T_p + \frac{13}{70}\Delta p^2 \frac{\dot{V}}{\beta} T_p \quad (3.45)$$

The proof of Equation (3.45) is shown in [7] under the assumptions that the volume change of the chamber is constant and that the chamber pressure dynamics may be described by a third order function as shown below, where T_p is the pressure development time shown in Figure 3.15.

$$p_c(t) = \frac{-2\Delta p}{T_p^3} t^3 + \frac{3\Delta p}{T_p^2} t^2 + p_{c,0} \quad \text{for } t_{p,s} < t < t_{p,e} \quad (3.46)$$

Where $t_{p,s}$ and $t_{p,e}$ are respectively the start and end time of the pressure development as shown in Figure 3.15. To illustrate the loss as a function of both piston position and velocity the energy loss is calculated for each chamber when changing from medium to high pressure, which is shown in the figure below.

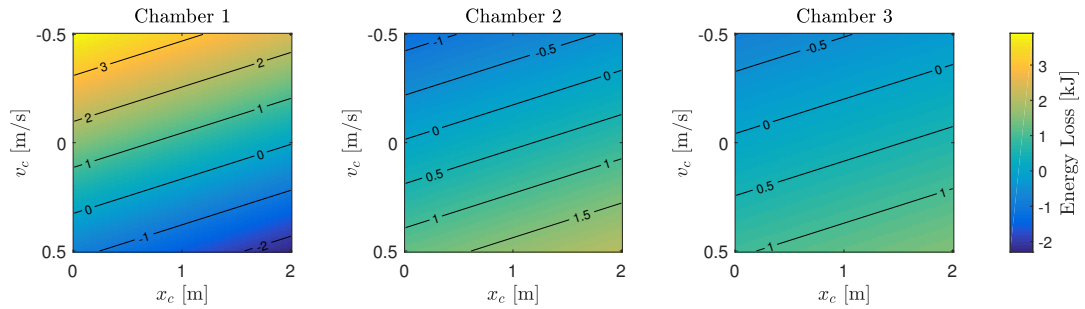


Figure 3.28: Energy loss for each chamber for different positions and velocities for a pressure shift from 100bar to 180bar, $T_p = 50\text{ms}$ and $\beta = 10000\text{bar}$.

As it can be seen in Figure 3.28 the energy loss is varying with the position and velocity. From Figure 3.28 it is evident the volume change is heavily influencing the loss associated with a pressure change. For high velocities and negative volume gradient, energy may even be recovered by changing pressure. This is evident from the energy loss being negative for some operating points in Figure 3.28.

3.4.3 Throttling Losses

A loss due to throttling the flow through each of the DFCUs is inevitable. Assuming infinitely fast switching, each of the cylinder chambers will always be connected to a DFCU with the same opening area. Thus the total power loss due to flow throttling may be described by the total flow and pressure drop across each active DFCU as:

$$P_{\text{loss,t}} = \sum_{i=1}^3 Q_i \Delta p_i = \sum_{i=1}^3 \frac{|A_i v_c|^3}{(n_i k_v)^2} \quad (3.47)$$

Where A_i is the piston area of the i 'th chamber, n_i is the number of valves in the DFCU connecting the i 'th chamber and k_v is the valve gain for the valves used in the DFCUs. As evident the throttling loss is dependent on the piston velocity cubed, and independent of the chamber pressures. The throttling losses from the resulting flow for each chamber and the total loss as function of the piston velocity are shown in the figures below.

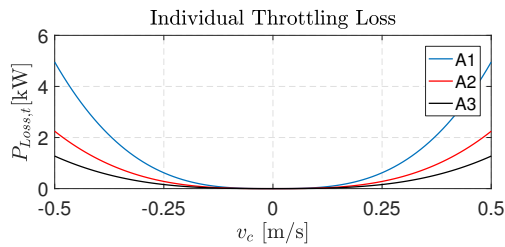


Figure 3.29: Throttling loss contribution from DFCU connected to chamber 1, 2 and 3.

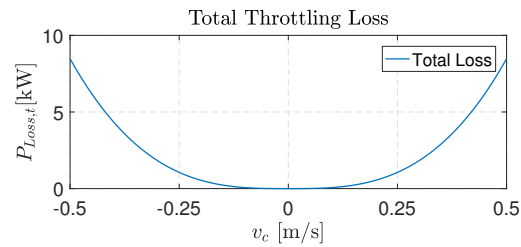


Figure 3.30: Combined throttling losses as function of the cylinder velocity.

From Figure 3.30 it is seen that the throttling loss is low for piston velocities under 0.2m/s . It may be expected that the throttling loss has a low influence on the PTO efficiency for lower sea states, but could become more dominant for higher sea states.

3.5 Validation

A validation of the PTO cylinder model and the estimated losses is done. In Figure 3.31 an overview of the test bench and the placement of the different sensors used for the validation is shown:

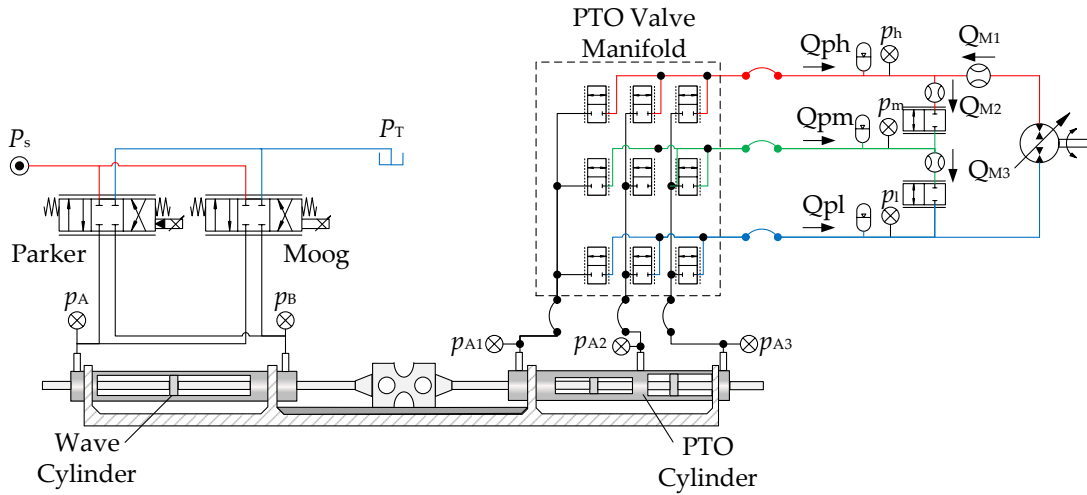


Figure 3.31: Overview of the test bench with indication of sensor placement.

As it can be seen the pressure transducers measuring the chamber pressures are placed close to the inlet of the chambers. Both the model and the loss estimation will be validated starting with the model.

3.5.1 Model Validation

To validate the model of the PTO system a number of tests is carried out on the Wave Star test bench. For a given test the valve input for both the wave cylinder and the PTO cylinder is logged and given as input for the model. The validation routine is performed according to Figure 3.32.

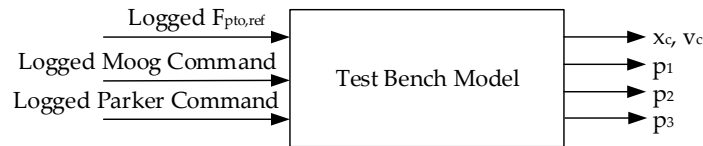


Figure 3.32: Validation routine

For validation of the pressure change inside each chamber a test is conducted where the cylinder is kept in a fixed position and the PTO force reference is changed such each chamber alternately is changed from medium to high pressure. In Figure 3.33 the line pressure connected to each cylinder chamber is shown and in Figure 3.34 the chamber pressures under each force change is shown.

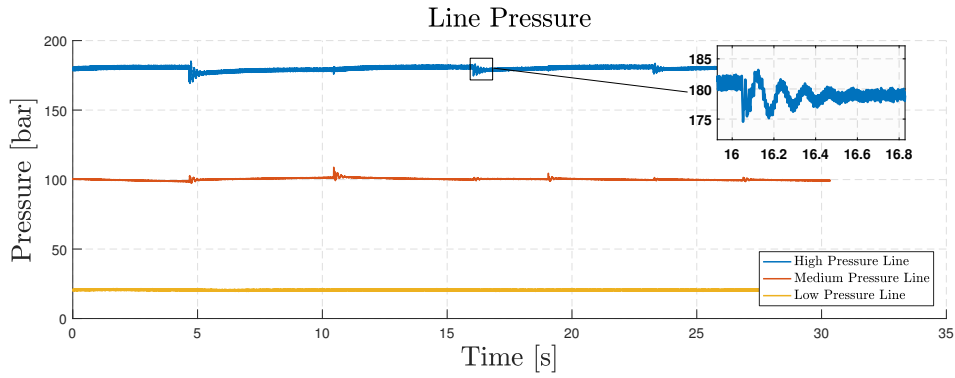


Figure 3.33: Line pressures.

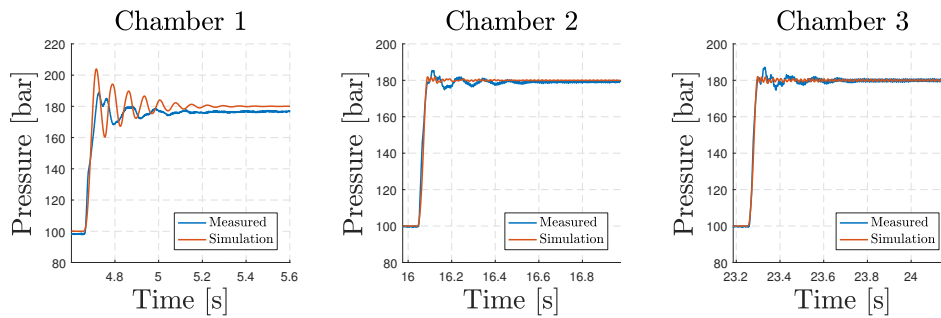


Figure 3.34: Pressure for each chamber of the PTO cylinder.

As shown the line pressures are oscillating during a pressure change. These oscillations may influence the chamber pressures and may explain some of the simulation deviation compared to the measurement. The model is seen to yield higher oscillating response compared to the measured response for chamber one. This may be due to the modelling of the opening trajectory of the valves which is simplified compared to the actual opening trajectory. As shown the pressure dynamics in each chamber is deviating from the measurements but is for model purposes considered sufficient. To validate the motion of the cylinder a test is carried out with the wave cylinder subjected to a sinusoidal motion with an amplitude of 0.2m/s and a frequency of 0.1Hz. In addition the PTO force reference is changed during the test. In Figure 3.35 the PTO force reference can be seen and in Figure 3.37 the position and velocity of the cylinder may be seen for both simulation and measurement.

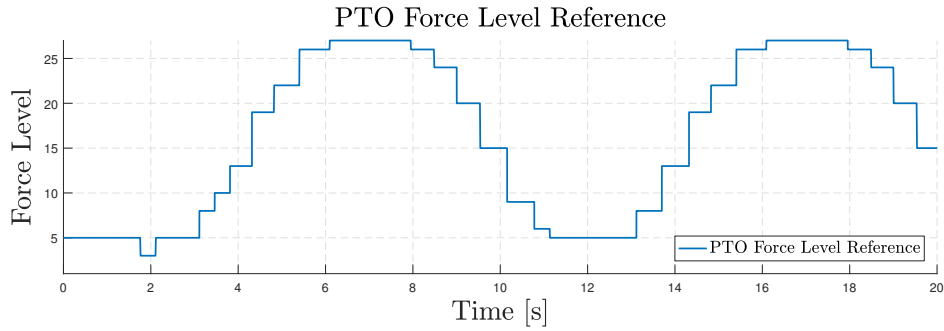


Figure 3.35: Force reference for PTO cylinder given as force level.

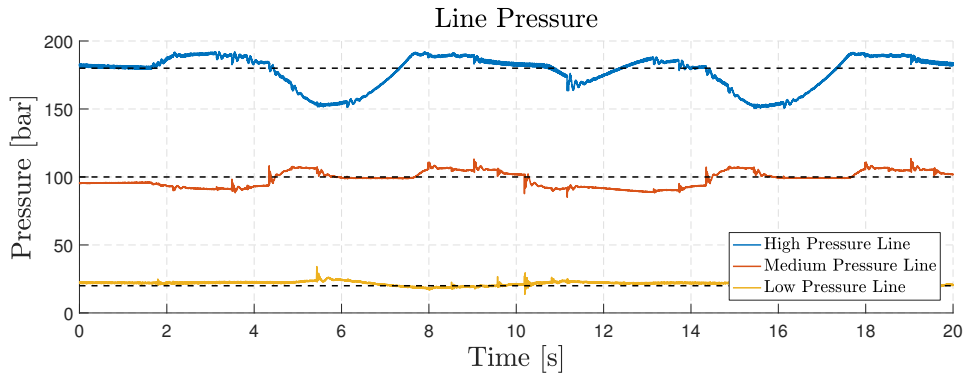


Figure 3.36: Line Pressures.

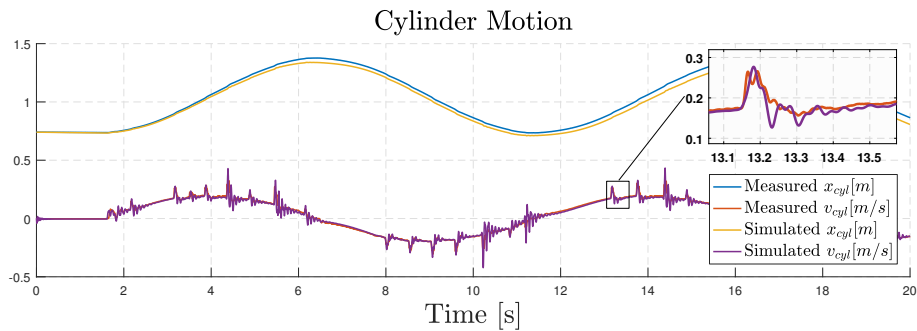


Figure 3.37: Position and velocity for of cylinder.

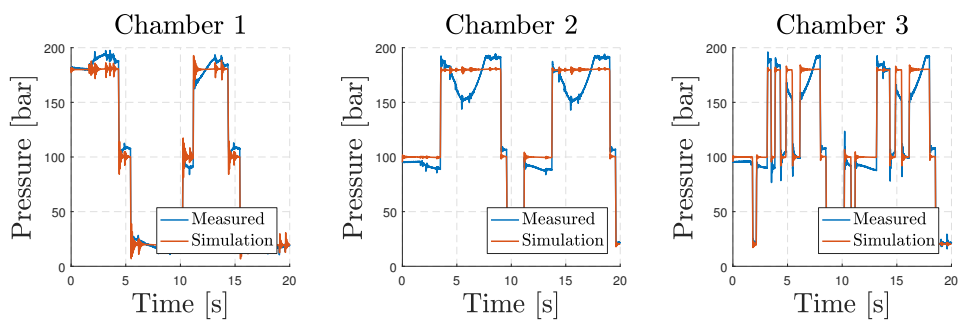


Figure 3.38: Cylinder chamber pressures for a sinusoidal cylinder motion.

As shown the line pressures are fluctuating which may explain the deviations in the chamber pressures. The velocity of the cylinder piston is in general seen to fit the mea-

surements. The oscillations of the cylinder piston velocity after a force shift are due to the low inertia of the system and would be smaller for the actual point absorber. The model deviation is expected as only the primary side of the PTO transmission is included in the model. The secondary side includes pumps, accumulators, and line pressure control and is obviously influencing the line pressures on the primary side. However, for the model purpose it is considered sufficient to neglect the dynamics of the secondary side of the PTO system.

3.5.2 Validation of Losses

It is desired to validate the assumed losses described in Section 3.4. The purpose of the validation is to investigate how the estimated losses corresponds to the measured efficiency of the discrete PTO transmission. The efficiency of the PTO transmission is calculated as the ratio between the input power to the PTO system, and the output power after the switching valve manifold. The input power is calculated as the PTO force multiplied with the piston velocity. The output power is defined as the sum of the power in the three pressure lines after the switching valve manifold. To calculate the output power, the flow and pressure transducers positioned on the test bench as shown in Figure 3.31 are utilised. The positioning of the flow transducers imposes different methods of calculating the output power, as the flow in the low pressure line is not measured directly. By the defined positive direction of the flow measurements as shown in Figure 3.31, the flow in the high and medium pressure lines may be calculated based on the three flow measurements as:

$$Q_{ph} = Q_{m2} - Q_{m1} \quad (3.48)$$

$$Q_{pm} = Q_{m3} - Q_{m2} \quad (3.49)$$

From the calculated flow rates in the high and medium pressure line, two different methods to calculate the output power are used, and the calculated output power based on flow and pressure measurements is an average of the two methods presented below.

Power Calculation Method 1

Taking the low pressure line as reference, the total output power may be calculated as:

$$\left. \begin{aligned} P_{h,1} &= Q_{ph} (p_h - p_l) \\ P_{m,1} &= Q_{pm} (p_m - p_l) \end{aligned} \right\} P_{out,1} = P_{h,1} + P_{m,1} \quad (3.50)$$

The output power of method 1 is thus calculated as the sum of the power in the medium and high pressure line with respect to the low pressure line.

Power Calculation Method 2

The second method is based on estimating the flow in the low pressure line based on measured cylinder velocity. The flow in the low pressure line is calculated as the volume gradient in each chamber, when the low pressure line is connected to the given volume, hence compression flow is neglected and only the steady state contribution is calculated. The flow in the low pressure line is thus calculated as shown below, where $v_{i,1} = 1$ denotes that the valve connecting the chamber to the low pressure line is open.

$$Q_{A1,pl} = \begin{cases} A_1 v_{cyl} & \text{if } v_{1,1} = 1 \\ 0 & \text{else} \end{cases} \quad Q_{A2,pl} = \begin{cases} A_2 v_{cyl} & \text{if } v_{2,1} = 1 \\ 0 & \text{else} \end{cases} \quad Q_{A3,pl} = \begin{cases} A_3 v_{cyl} & \text{if } v_{3,1} = 1 \\ 0 & \text{else} \end{cases}$$

The total flow in the low pressure line in the defined positive direction may be calculated as:

$$Q_{pl} = Q_{A1,pl} - Q_{A2,pl} - Q_{A3,pl} \quad (3.51)$$

Where $Q_{A1,pl}$ is defined as flow from the cylinder to the pressure line and $Q_{A2,pl}$ and $Q_{A3,pl}$ are defined as flow from the pressure line to the cylinder. The output power is then given as:

$$P_{out,2} = Q_{ph}p_h + Q_{pm}p_m + Q_{pl}p_l \quad (3.52)$$

Efficiency Calculation

The efficiency of the PTO transmission based on pressure and flow measurement is calculated as:

$$\eta_{mes} = \frac{E_{out,mes}}{E_{in}} = \frac{\int \left(\frac{1}{2} P_{out,1} + \frac{1}{2} P_{out,2} \right) dt}{\int v_c F_{pto} dt} \quad (3.53)$$

The estimated efficiency of the test bench is calculated based on the estimated shifting loss for each force shift and throttling losses according to Equation (3.45) and Equation (3.47) as:

$$\eta_{est} = \frac{E_{in} - E_{loss,\beta} - E_{loss,t}}{E_{in}} = \frac{\int v_c F_{pto} dt - \sum_{i=1}^{n_{shifts}} E_{loss,\beta,i} - \int P_{loss,t} dt}{\int v_c F_{pto} dt} \quad (3.54)$$

To validate the estimated losses, the test bench is operated in four different operation cycles and the estimated efficiency is compared to the measured efficiency. For two of the operating cycles the wave cylinder is configured to emulate irregular waves for sea state 1 and 2, and the remaining two are for regular sine waves with a frequency of 0.1Hz and 0.3Hz respectively both with a velocity amplitude of 0.2[m/s]. In Table 3.5 the measured average power input and power output along with measured and estimated efficiencies for the four test are shown. In the tests a reactive controller is used along with the FSA, described in Section 1.2, to determine the applied discrete force level. The same controller is used for all the tests.

<i>Test wave</i>	SS1	SS2	sine 1	sine 2
$P_{in,avg,mes}[kW]$	6.97	11.65	9.73	12.87
$P_{out,avg,mes}[kW]$	5.33	9.06	7.71	10.33
η_{mes}	0.76	0.77	0.79	0.80
η_{est}	0.85	0.88	0.9	0.89

Table 3.5: Measured and estimated PTO efficiency for different test waves.

From the table it is evident that the estimated efficiency is 9-11 percentage points above the measured efficiency. The difference may be due to friction and other loss mechanism which are not included in the efficiency calculation and . From the losses included in the loss estimation, the throttling loss is seen to contribute to approximately 18% of the total loss in average over the four different tests. As the deviation of the estimated and measured efficiency is similar for all operation cycles the estimated efficiency may be used to compare efficiency of different control strategies.

3.6 Part Conclusion

A linear model of the Wave Star point absorber was derived, with the purpose of utilizing the model in MPC. A nonlinear model of the PTO cylinder was derived as well. To validate the model of the PTO cylinder, a model of the PTO test bench at AAU was developed to allow validation of the model by practical tests. Measurement performed on the test bench showed acceptable correlation with simulated response, why the PTO cylinder model is used to evaluate the MPC performance by simulations. Simple loss mechanisms were modelled as well, with the purpose of including the losses in the MPC formulation. Estimated and measured efficiency of the test bench was seen to deviate from each other. An offset of 9-11 percentage points between measured and estimation efficiency was seen.

4 | Model Predictive Control

In this chapter the MPC scheme is derived. MPC computes the control input by solving an optimisation problem based on future predicted states and disturbances such that the harvested energy is maximised. Generally, MPC is used as a tracking controller where a desired state trajectory is to be tracked. The MPC derived in the next section is based on computing the PTO torque to yield maximum harvested energy over a finite time horizon. As the MPC is to be implemented online, linear MPC is used. Linear MPC permits to formulate the state predictions as simple static matrix calculations, why linear MPC in general offers lower computational demand compared to e.g. nonlinear MPC. Initially a MPC scheme computing a continuous PTO torque reference is developed for simplicity and to allow comparison against optimal control in regular waves. Well-established techniques and efficient solvers for such MPC problems exist. This allows a comprehensive simulation study, and the MPC performance may be evaluated in a wide range of control parameters. A MPC scheme able to handle discrete inputs is developed in Chapter 5.

4.1 MPC Formulation

The formulation of the MPC is based on the linear model of the point absorber, as the linearity offers the aforementioned advantages. The linear time invariant model of the point absorber in discrete time domain, may be described by:

$$\mathbf{x}_{k+1} = \mathbf{A}\mathbf{x}_k + \mathbf{B}\mathbf{u}_k \quad (4.1)$$

$$\mathbf{y}_k = \mathbf{C}\mathbf{x}_k \quad (4.2)$$

Where \mathbf{x}_k is the state vector, \mathbf{A} and \mathbf{B} are system matrices dependent of the model discretisation, and \mathbf{y}_k is the output vector. The advantage of linear MPC is that the problem over a finite time horizon may be "lifted" such that the future states χ_{k+} is explicitly formulated in terms of the initial states \mathbf{x}_k and the future control inputs \mathbf{u}_{k+} . The state space model of Equation (4.1) may be used as a prediction of the states one step ahead. Equation (4.1) may be written at the time $k + 1$ as:

$$\mathbf{x}_{k+2} = \mathbf{A}\mathbf{x}_{k+1} + \mathbf{B}\mathbf{u}_{k+1} \quad (4.3)$$

$$\mathbf{x}_{k+2} = \mathbf{A}^2\mathbf{x}_k + \mathbf{A}\mathbf{B}\mathbf{u}_k + \mathbf{B}\mathbf{u}_{k+1} \quad (4.4)$$

This relation may be used to formulate the prediction of the future state over a horizon N as[20]:

$$\underbrace{\begin{bmatrix} \mathbf{x}_{k+1} \\ \mathbf{x}_{k+2} \\ \mathbf{x}_{k+3} \\ \vdots \\ \mathbf{x}_{k+N} \end{bmatrix}}_{\chi_{k+}} = \underbrace{\begin{bmatrix} \mathbf{A} \\ \mathbf{A}^2 \\ \mathbf{A}^3 \\ \vdots \\ \mathbf{A}^N \end{bmatrix}}_{\mathbf{P}} \mathbf{x}_k + \underbrace{\begin{bmatrix} \mathbf{B} & \mathbf{0} & \mathbf{0} & \cdots & \mathbf{0} \\ \mathbf{A}\mathbf{B} & \mathbf{B} & \mathbf{0} & \cdots & \mathbf{0} \\ \mathbf{A}^2\mathbf{B} & \mathbf{A}\mathbf{B} & \mathbf{B} & \cdots & \mathbf{0} \\ \vdots & \vdots & \vdots & \ddots & \vdots \\ \mathbf{A}^{N-1}\mathbf{B} & \mathbf{A}^{N-2}\mathbf{B} & \mathbf{A}^{N-3}\mathbf{B} & \cdots & \mathbf{B} \end{bmatrix}}_{\mathbf{H}} \underbrace{\begin{bmatrix} \mathbf{u}_k \\ \mathbf{u}_{k+1} \\ \mathbf{u}_{k+2} \\ \vdots \\ \mathbf{u}_{k+N-1} \end{bmatrix}}_{\mathbf{u}_{k+}} \quad (4.5)$$

Where $\mathbf{0}$ is a zero matrix of appropriate size. χ_{k+} is a vector of the predicted future states over the time horizon of length N subject to the initial states \mathbf{x}_k at time k and the control inputs over the horizon contained in the vector \mathbf{u}_{k+} . The matrices \mathbf{P} and \mathbf{H} are

defined as the prediction matrices, and contains the system matrices of Equation (4.1). The predicted future outputs is given as:

$$\mathbf{y}_\omega = \mathbf{C}_\omega \chi_{k+} \quad , \quad \mathbf{C}_\omega = \begin{bmatrix} \mathbf{C} & \mathbf{0} & \mathbf{0} & \cdots & \mathbf{0} \\ \mathbf{0} & \mathbf{C} & \mathbf{0} & \cdots & \mathbf{0} \\ \mathbf{0} & \mathbf{0} & \mathbf{C} & \cdots & \mathbf{0} \\ \vdots & \vdots & \vdots & \ddots & \vdots \\ \mathbf{0} & \mathbf{0} & \mathbf{0} & \cdots & \mathbf{C} \end{bmatrix} \quad (4.6)$$

Considering the point absorber model, the prediction of future states may be formulated as:

$$\chi_{k+} = \mathbf{P}\mathbf{x}_k + \mathbf{H}\boldsymbol{\tau}_{\text{ext},v} - \mathbf{H}\boldsymbol{\tau}_{\text{pto},v} \quad (4.7)$$

With:

$$\boldsymbol{\tau}_{\text{ext},v} = [\boldsymbol{\tau}_{\text{ext},k} \quad \boldsymbol{\tau}_{\text{ext},k+1} \quad \boldsymbol{\tau}_{\text{ext},k+2} \quad \cdots \quad \boldsymbol{\tau}_{\text{ext},k+N-1}]^T \quad (4.8)$$

$$\boldsymbol{\tau}_{\text{pto},v} = [\boldsymbol{\tau}_{\text{pto},k} \quad \boldsymbol{\tau}_{\text{pto},k+1} \quad \boldsymbol{\tau}_{\text{pto},k+2} \quad \cdots \quad \boldsymbol{\tau}_{\text{pto},k+N-1}]^T \quad (4.9)$$

Where $\boldsymbol{\tau}_{\text{ext}}$ is a vector containing future wave excitation torques, and $\boldsymbol{\tau}_{\text{pto}}$ is a vector containing the applied PTO torque over the time horizon. The goal of the MPC is to maximise the harvested energy over a given horizon. If only considering maximising the mechanical power transferred to the point absorber, the absorbed energy may be given from the integral of the instantaneous absorbed power over the time horizon as:

$$E_{\text{abs}} = \int_t^{t+T_s N} P_{\text{abs}}(\boldsymbol{\tau}) d\boldsymbol{\tau} = \int_t^{t+T_s N} \boldsymbol{\omega}_{\text{arm}}(\boldsymbol{\tau}) \boldsymbol{\tau}_{\text{pto}}(\boldsymbol{\tau}) d\boldsymbol{\tau} \quad (4.10)$$

Where T_s is the MPC sample time. The discrete approximation of Equation (4.10) may be formulated as:

$$E_{\text{abs}} \approx T_s \sum_{i=k}^{k+N} \boldsymbol{\omega}_{\text{arm},i+1} \boldsymbol{\tau}_{\text{pto},i} = T_s (\mathbf{C}_\omega \chi_{k+})^T \boldsymbol{\tau}_{\text{pto},v} \quad (4.11)$$

As evident the discrete approximation of Equation (4.10) resembles a backward euler integration method, which is a first order integration method. If the PTO torque dynamics are neglectable, hence the PTO dynamics are much faster than the absorber dynamics, the approximation to the integral is considered fair if the sample time is chosen in the order of 10 times faster than the absorber dynamics.

Inserting Equation (4.7) into (4.11) yields:

$$E_{\text{abs}} = T_s \left[[\mathbf{C}_\omega (\mathbf{P}\mathbf{x}_k + \mathbf{H}\boldsymbol{\tau}_{\text{ext},v} - \mathbf{H}\boldsymbol{\tau}_{\text{pto},v})]^T \boldsymbol{\tau}_{\text{pto},v} \right] \quad (4.12)$$

$$= T_s \left[\mathbf{x}_k^T \mathbf{P}^T \mathbf{C}_\omega^T \boldsymbol{\tau}_{\text{pto},v} + \boldsymbol{\tau}_{\text{ext},v}^T \mathbf{H}^T \mathbf{C}_\omega^T \boldsymbol{\tau}_{\text{pto},v} - \boldsymbol{\tau}_{\text{pto},v}^T \mathbf{H}^T \mathbf{C}_\omega^T \boldsymbol{\tau}_{\text{pto},v} \right] \quad (4.13)$$

$$= T_s \left[-\boldsymbol{\tau}_{\text{pto},v}^T \underbrace{\mathbf{H}^T \mathbf{C}_\omega^T}_{\mathbf{Q}} \boldsymbol{\tau}_{\text{pto},v} + \underbrace{\left(\mathbf{x}_k^T \mathbf{P}^T \mathbf{C}_\omega^T + \boldsymbol{\tau}_{\text{ext},v}^T \mathbf{H}^T \mathbf{C}_\omega^T \right)}_{\mathbf{f}} \boldsymbol{\tau}_{\text{pto},v} \right] \quad (4.14)$$

$$= T_s \left[-\boldsymbol{\tau}_{\text{pto},v}^T \mathbf{Q} \boldsymbol{\tau}_{\text{pto},v} + \mathbf{f} \boldsymbol{\tau}_{\text{pto},v} \right] \quad (4.15)$$

Only considering maximisation of the absorbed energy over a finite time horizon the optimisation problem may be formulated as:

$$\begin{aligned} & \underset{\tau_{\text{pto},v} \in \mathbb{R}^N}{\text{Min}} \left(T_s \left[\tau_{\text{pto},v}^T \mathbf{Q} \tau_{\text{pto},v} - \mathbf{f} \tau_{\text{pto},v} \right] \right) \\ & \text{s.t.} \quad \tau_{\text{pto},\min} \leq \tau_{\text{pto}} \leq \tau_{\text{pto},\max} \end{aligned} \quad (4.16)$$

Where $\tau_{\text{pto},\max}$ and $\tau_{\text{pto},\min}$ are the upper and lower bound of τ_{pto} and is chosen to $\pm 1MNm$. The objective function in Equation (4.15) may be seen to have quadratic and linear terms of $\tau_{\text{pto},v}$, why the minimisation problem is a quadratic programming problem. The problem may be solved by standard quadratic solvers, e.g the solver *quadprog* in Matlab. Identifying \mathbf{Q} as the Hessian of the problem, the quadratic programming formulation of the MPC is convex, as \mathbf{Q} is found to be positive definite.

4.1.1 Constraints

One of the advantages of using MPC is that constraints can be included in the control algorithm. Constraints may arise from physical limits of the system such as cylinder stroke or a maximum allowed cylinder velocity. Constraints may be introduced in different ways dependent of how strictly the constraints have to be fulfilled. Hard constraints does not allow the solution to violate the constraints and may be included in the optimisation problem by extending it as shown below:

$$\begin{aligned} & \underset{\tau_{\text{pto},v} \in \mathbb{R}}{\text{Min}} \left(T_s \left[\tau_{\text{pto},v}^T \mathbf{Q} \tau_{\text{pto},v} - \mathbf{f} \tau_{\text{pto},v} \right] \right) \\ & \text{s.t.} \\ & \text{bounds : } \tau_{\text{pto},\min} \leq \tau_{\text{pto}} \leq \tau_{\text{pto},\max} \\ & \text{inequality constraints : } \gamma_m(x) \leq 0 \quad \text{for } m = 1, 2, \dots, M \\ & \text{equality constraints : } \varphi_l(x) = 0 \quad \text{for } l = 1, 2, \dots, L \end{aligned}$$

Where M and L is the number of inequality and equality constraints respectively. Constraints regarding cylinder position and velocity may be necessary due to the limited stroke of the cylinder. This may be included by inequality constraints as shown below:

$$\begin{aligned} \gamma_{\max,m}(x) &= X_{k+} - x_{\max} \quad \text{for } m = 1, 2, \dots, M \\ \gamma_{\min,m}(x) &= -X_{k+} + x_{\min} \quad \text{for } m = 1, 2, \dots, M \end{aligned}$$

Where X_{k+} is the system states in cylinder coordinates. x_{\min} and x_{\max} are vectors containing the constraints of the cylinder position and velocity. The physical constraints may also be implemented by soft constraints. Soft constraints are formulated by penalising the cost function if the constraints are violated. This can be done by introducing slack variables in the form of a scalar p and a vector S defined as:

$$S = [s_m \quad \dots \quad s_M] \quad \text{for } m = 1, 2, \dots, M \quad (4.17)$$

The optimisation problem may then be changed to:

$$\begin{aligned}
 & \underset{\tau_{\text{pto},v} \in \mathbb{R}}{\text{Min}} \left(T_s \left[\tau_{\text{pto},v}^T \mathbf{Q} \tau_{\text{pto},v} - \mathbf{f} \tau_{\text{pto},v} \right] + p \|S\| \right) \\
 & \text{s.t.} \\
 & \tau_{\text{pto},\min} \leq \tau_{\text{pto}} \leq \tau_{\text{pto},\max} \\
 & \gamma_m(x) + s_m = 0 \quad \text{for } m = 1, 2, \dots, M \\
 & s_m \geq 0 \quad \text{for } m = 1, 2, \dots, M
 \end{aligned}$$

By doing this a violation of the constraints is allowed, but by choosing p sufficiently high violations will only occur if no feasible solution exist. The scalar p is thus a parameter to be tuned determining the "softness" of the constraints. By choosing $p = 0$ an unconstrained problem is obtained and by choosing $p = \infty$ the original hard constrained problem is obtained. For the system considered in this thesis constraints may turn the optimisation infeasible as the system is driven by the ocean waves. This means that infeasibility may be inevitable at instances with relatively large incoming waves and hard constraints on e.g. the point absorber velocity as the generated PTO torque may not be sufficient to brake the system. For this reason it is concluded that including constraints in the optimisation may turn out irrelevant and is therefore omitted.

4.2 MPC Analysis

An analysis of the MPC performance subject to model complexity and parameter sensitivity is done. The analysis is performed assuming that the PTO torque is continuous for simplicity. This also allows for comparison of the MPC and analytical derived optimal power extraction in regular waves. The purpose of the analysis is to obtain indications of the necessary MPC time horizon and sample time, as well as the influence of considering non ideal PTO efficiency, why simple damping losses are included in the MPC formulation. Lastly a forecasting of the excitation torque is developed to evaluate the performance of MPC with unknown future waves compared to perfect knowledge of the future wave of the finite time horizon. Only the point absorber dynamics are considered for the following analysis, hence the PTO dynamics are considered infinitely fast. The following simulations are performed according to the figure below. For the analysis ideal wave estimation is assumed if nothing else is stated.

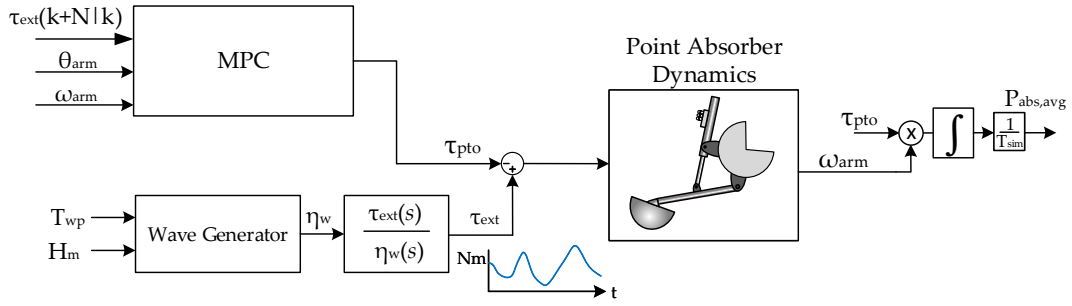


Figure 4.1: Diagram of simulation routine performed for the MPC analysis.

4.2.1 Optimal Power Extraction

To test the MPC algorithm it is compared to a reactive control scheme subject to a sine wave excitation. This allows identification of reactive control parameters which yields optimal wave power extraction. The mechanical system may be described as an equivalent electrical circuit as shown in Figure 4.2, where the float arm velocity corresponds to the current, and torque corresponds to the voltage.

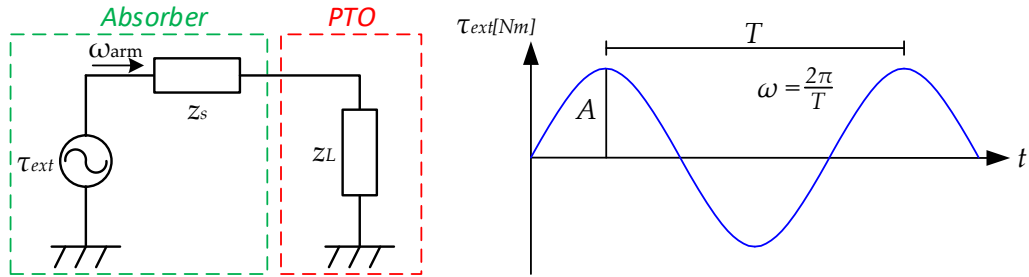


Figure 4.2: Equivalent electrical circuit of the mechanical absorber and PTO system.

The mechanical system may be interpreted as being driven by an excitation torque, with the dynamics given by the mechanical absorber impedance and the mechanical PTO impedance. The analogue to the electrical system may be interpreted as inductance corresponding to inertia J , capacitance to inverse of spring constant $\frac{1}{k}$, and resistance being damping B [16]. Thus the source and load impedance shown in Figure 4.2 may be described in terms of mechanical parameters as:

$$Z_s = R_s + jX_s = B_{rad} + j\omega(J_{tot} + J_\infty) - j\frac{k_{res}}{\omega} \quad (4.18)$$

$$Z_L = R_L + jX_L = B_{pto} + j\omega J_{pto} - j\frac{k_{pto}}{\omega} \quad (4.19)$$

Where ω is the frequency of τ_{ext} . B_{rad} is the radiation damping torque coefficient, and is constant for a regular wave excitation. Maximum power is dissipated in the load impedance, hence power being delivered to the PTO system, if $Z_L = Z_s^*$, where $*$ denotes

the complex conjugate. According to Ohm's law in the mechanical analogy it follows that: $\tau_{pto} = Z_L \omega_{arm}$. If it is assumed that the PTO torque is applied as $\tau_{pto} = B_{pto} \omega_{arm} + k_{pto} \theta_{arm}$, the reactive control law that yields optimal wave power extraction for a sine wave excitation with position and velocity feedback may be found by solving:

$$\left. \begin{aligned} Z_L &= Z_s^* \\ \tau_{pto} &= k_{pto} \theta_{arm} + B_{pto} \omega_{arm} \end{aligned} \right\} \Rightarrow \begin{aligned} k_{pto} &= (J_{tot} + J_{\infty}) \omega^2 - k_{res} \\ B_{pto} &= B_{rad} \end{aligned} \quad (4.20)$$

The optimal control for a regular wave is thus defined by system parameters and the incoming wave frequency. To test the MPC against the optimal control case, an arbitrary wave may be chosen. For the comparison, a sine wave with a frequency of 0.2Hz and an amplitude of 0.3m is chosen. For this specific wave, the optimal control parameters for the reactive control are identified as:

$$\begin{aligned} k_{pto} &= -8.03 \cdot 10^6 \left[\frac{\text{Nm}}{\text{rad}} \right] \\ B_{pto} &= 8.16 \cdot 10^5 \left[\frac{\text{Nm s}}{\text{rad}} \right] \end{aligned} \quad (4.21)$$

The MPC parameters to be tuned are the time horizon and the sample time. It is expected that the MPC solution will approach the optimal solution as the time horizon and sample frequency goes towards infinity. The MPC is tested in the simulation model, and the time horizon is iteratively tuned until the MPC solution converges to the optimal reactive control solution. The MPC was seen to approach the optimal reactive solution with a sample time of $T_s = 0.025s$ and a horizon length of $N = 265$ corresponding to a time horizon of 6.625 seconds. The simulation results are shown in the figures below.

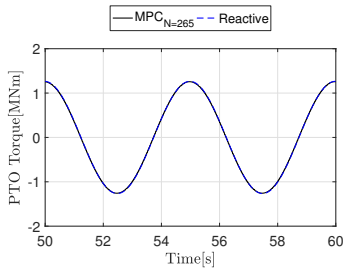


Figure 4.3: PTO torques for the reactive and MPC.

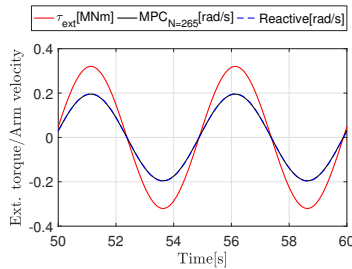


Figure 4.4: Excitation torque and arm velocities.

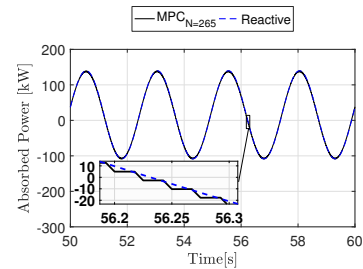


Figure 4.5: Instantaneous power for reactive and MPC.

From Figure 4.4 it is seen that the excitation torque and absorber velocity are in phase for both the reactive controller and the MPC, thus optimal power extraction occurs. Due to the inherently discrete computation of the PTO torque of the MPC, the instantaneous power also becomes piecewise constant as evident from the zoom shown in Figure 4.5. As elaborated in Section 4.1, the discrete approximation of the absorbed energy over the MPC time horizon in Equation (4.11) resembles a backward euler integration method, which may also be seen in the zoom of Figure 4.5. From this it may be concluded that the MPC solution go towards the optimal PTO trajectory if the sample frequency and the time horizon go towards infinity. For the two simulations shown in the figures above the average absorbed power is 15.7kW for the reactive control and 15.2kW for the MPC.

To test the performance of the MPC scheme against the reactive control scheme, they are tested in irregular waves as well, and a parameter study of the sample time and time

horizon of the MPC is performed. In order to simplify the MPC algorithm, a truncated model formulation is investigated to lower the computational demand and to avoid the necessity of state estimation.

4.2.2 Truncated Model Formulation

The virtual radiation damping states of the model in Equation (3.10) are not available for measurement. However as the model is formulated in observer canonical form, the states may be estimated by design of an observer. The states may be estimated by[21]:

$$\dot{\hat{x}} = (\mathbf{A} - \mathbf{LC})\hat{x} + \mathbf{B}u + \mathbf{L}y \quad (4.22)$$

Where \mathbf{L} is the observer gain matrix and y are the measured states; the arm angle and angular velocity. The poles of \mathbf{L} are placed such the estimation error dynamics are ten times faster than the open loop poles of the system shown in Equation (3.10).

In regard to the MPC formulation, using the full order model may introduce higher computational demand as the prediction matrices \mathbf{H} and \mathbf{P} rapidly increases in size with the horizon length N . For this reason it is desired to investigate a truncation of the model in order to obtain a MPC formulation with smaller prediction matrices. The model given in Equation (3.10) may be simplified by having the radiation damping filter expressed in a single damping coefficient B_{damp} . Thus the truncated model is given as:

$$\underbrace{\begin{bmatrix} \ddot{\theta}_{\text{arm}} \\ \dot{\omega}_{\text{arm}} \\ \omega_{\text{arm}} \end{bmatrix}}_{\dot{\mathbf{x}}_s} = \underbrace{\begin{bmatrix} -B_{\text{damp}} & -k_{\text{res}} \\ J_{\text{tot}} + J_{\infty} & 0 \\ 1 & 0 \end{bmatrix}}_{\mathbf{A}_s} \underbrace{\begin{bmatrix} \omega_{\text{arm}} \\ \theta_{\text{arm}} \end{bmatrix}}_{\mathbf{x}_s} + \underbrace{\begin{bmatrix} 1 \\ J_{\text{tot}} + J_{\infty} \\ 0 \end{bmatrix}}_{\mathbf{B}_s} \underbrace{(\tau_{\text{ext}} - \tau_{\text{pto}})}_u \quad (4.23)$$

Another advantage of formulating the MPC on this form is that the state estimation is avoided as only the measured states, arm angle and angular velocity, are needed for the MPC. To test if the truncation is reasonable, the full order MPC is compared to a MPC formulation with the truncated model. To determine the best choice of the damping coefficient B_{damp} , the MPC is evaluated with different values of B_{damp} and sea states with respect to average harvested power for wave series containing 100 wave periods. The comparison of the full order formulation and the truncated formulation for three different sea states and different values of the damping coefficient are shown in Figure 4.6-4.8 where the dashed line indicates the average absorbed power for the MPC with the full order model. The simulations are performed in a simulation model of the full order model shown in Equation (3.10), and with either the truncated model or full order model in the MPC formulation.

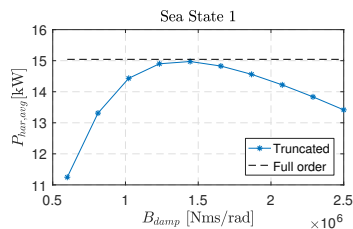


Figure 4.6: Varying damping compared to full order formulation for SS1.

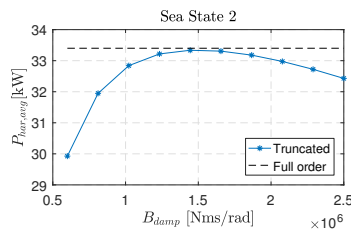


Figure 4.7: Varying damping compared to full order formulation for SS2.

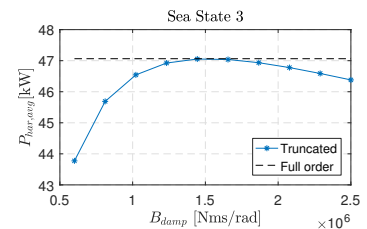


Figure 4.8: Varying damping compared to full order formulation for SS3.

From the figures it is evident that an optimal choice of the damping coefficient exist. It is seen that the maximum average harvested power for all three sea states for the truncated MPC formulation is close to a damping coefficient of $1.5 \frac{Nms}{rad}$ for the three sea states. For the three sea states the average harvested power for the truncated formulation with the best damping coefficient are in average only 0.1% below the average harvested power obtained by the full order MPC formulation. By this it is regarded as fair to use the truncated MPC formulation if the damping coefficient B_{damp} is chosen to the optimal value for the given sea state. The optimal choice of B_{damp} is seen to slightly vary with the horizon length N as well. This is addressed by tuning the constant damping coefficient once the horizon length is chosen.

4.2.3 Parameter Study

A parameter study on the sample time T_s and horizon length N is performed to investigate the MPC performances' sensitivity to these values. In the first part of the parameter study the efficiency of the PTO system is not considered, as only the influence of the MPC parameters is desired.

Initially the PTO moment trajectory is investigated based on the sample time and horizon length. The PTO moment trajectory for the reactive control scheme is included for comparison. The comparison is performed on the wave signal showed in Figure 4.9, which is a wave signal generated for sea state 2.

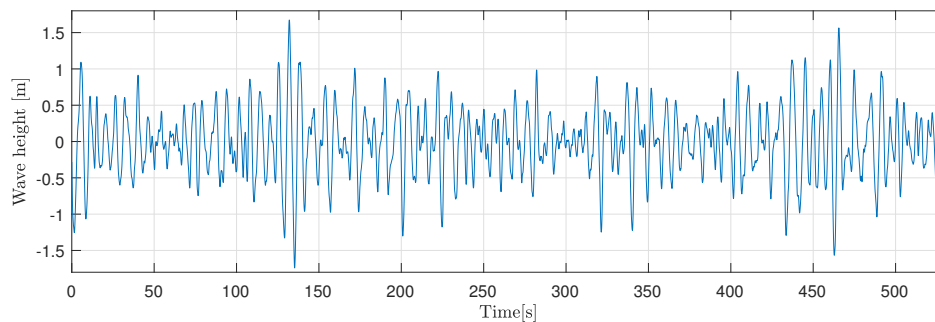


Figure 4.9: Wave signal used in the following comparison.

For the given wave signal the MPC is tested for different time horizons. The simulation results are shown in Figure 4.11-4.13. A simulation for the same wave signal with reactive control is shown in Figure 4.10.

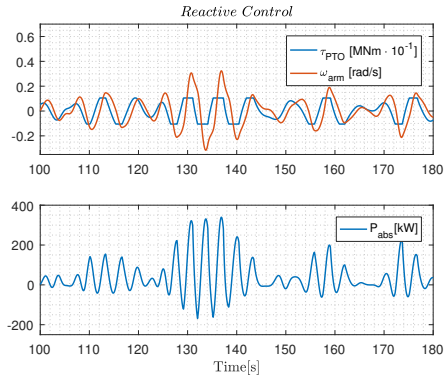


Figure 4.10: Simulation result for reactive control.

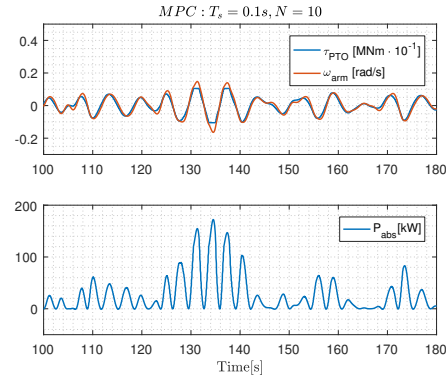


Figure 4.11: Simulation result for MPC with $T_s = 0.1s$ and $N = 10$.

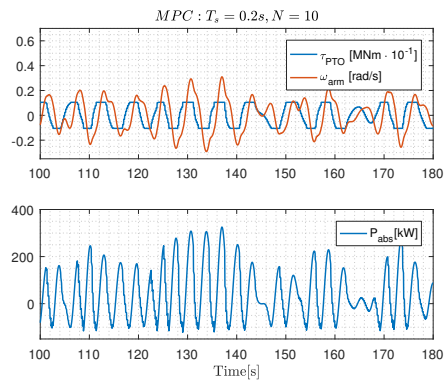


Figure 4.12: Simulation result for MPC with $T_s = 0.2s$ and $N = 10$.

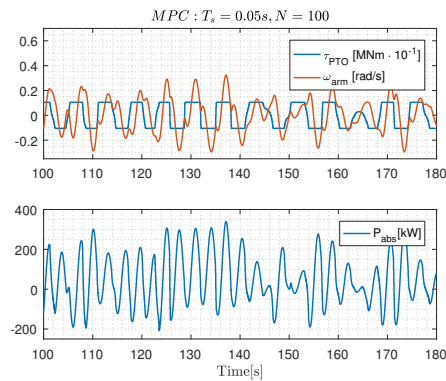


Figure 4.13: Simulation result for MPC with $T_s = 0.05s$ and $N = 100$.

From the simulation results it is evident that increasing the time horizon also results in four quadrant power operation. From Figure 4.11, where the time horizon is 1s, the power transfer only occurs in one direction. This may be explained by the relatively short time horizon compared to the peak period of the waves which is 5.57s for sea state 2. From Figure 4.12 it is evident that increasing the time horizon imposes reactive power for the PTO system. For the simulation with a sample time of 0.2s and a horizon length of 10 the PTO torque is seen to jump between the saturation limits of the PTO torque. Further increasing the time horizon to 5s as shown in Figure 4.13 is seen to change the PTO torque trajectory to jump between the saturation limits faster.

To assess the MPC performance's sensitivity to the sample time and time horizon, the MPC is evaluated with respect to average absorbed power for a wave series containing 100 wave periods for three different sea states. The results are shown in Figure 4.14 and Figure 4.15. From Figure 4.14 it is evident that a time horizon beyond 6 seconds does not influence the average absorbed power. The time horizon could be chosen to 3 or 4 seconds without significant influence on the average absorbed power. The influence of varying the sample period is shown in Figure 4.15. Here the time horizon is chosen to 6s to only see the influence of the sample period. From the simulations, a similar decrease in absorbed power is seen with increasing sample period for all sea states. For sea state 1 a sample time of 0.4s results in a negative average absorbed power. This suggest that a upper bound of the sample time must be formulated. A maximum sample time of 0.35s is imposed due to the natural period of the point absorber of approximately 3.5 seconds. With a sample period 0.35s approximately ten samples during one natural period of the

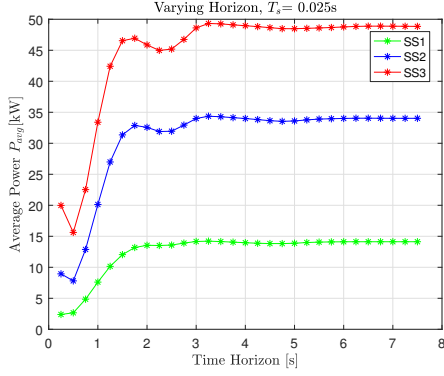


Figure 4.14: Average absorbed power for different time horizons and sea states.

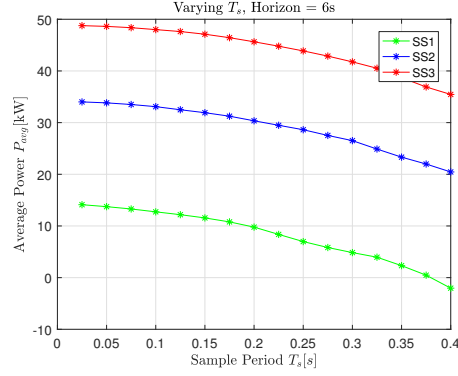


Figure 4.15: Average absorbed power for different sample periods and sea states.

system is performed. From Figure 4.15 it may be concluded that the MPC sample time should be chosen as low as possible considering infinitely fast PTO dynamics.

4.2.4 MPC including PTO Efficiency

So far, the efficiency of the PTO system has not been considered. It is desired to investigate the influence of a non-ideal PTO system with respect to the MPC performance. A simple case is investigated, where a damping friction loss is included in the PTO system. The simple friction loss is given by $P_{\text{loss}} = b_f \omega_{\text{arm}}^2$. From the simulation results shown in Figure 4.11-4.13 a longer time horizon of the MPC is seen to force the point absorber to higher velocities. With friction losses present it may be expected that this is not the optimal solution, as the power delivered to the grid will be affected by the friction losses in the PTO system.

The energy harvested including the damping friction loss over the time horizon may be stated as:

$$E_{\text{har}} = \int_t^{t+T_s N} P_{\text{abs}}(\tau) - P_{\text{loss}}(\tau) d\tau = \int_t^{t+T_s N} \omega_{\text{arm}}(\tau) \tau_{\text{pto}}(\tau) - b_f \omega_{\text{arm}}^2(\tau) d\tau \quad (4.24)$$

The discretized approximation may be given as:

$$E_{\text{har}} \approx T_s \sum_{i=k}^{k+N} \omega_{\text{arm},i+1} \tau_{\text{pto},i} - b_f \omega_{\text{arm},i+1}^2 = T_s \left[(\mathbf{C}_{\omega\chi})^T \tau_{\text{pto},v} - (\mathbf{C}_{\omega\chi})^T b_f (\mathbf{C}_{\omega\chi}) \right] \quad (4.25)$$

By writing out Equation (4.25) and neglecting terms without the future control inputs, the quadratic programming problem can be formulated as:

$$E_{\text{har}} = T_s \left[-\tau_{\text{pto},v}^T \underbrace{(\mathbf{H}^T \mathbf{C}_{\omega}^T b_f \mathbf{C}_{\omega} \mathbf{H} + \mathbf{H}^T \mathbf{C}_{\omega})}_{\mathbf{Q}_f} \tau_{\text{pto},v} + \underbrace{(\mathbf{x}_k^T \mathbf{P}^T \mathbf{C}_{\omega}^T \tau + \tau_{\text{ext},v}^T \mathbf{H}^T \mathbf{C}_{\omega}^T + 2(\mathbf{x}_k^T \mathbf{P}^T \mathbf{C}_{\omega}^T b_f \mathbf{C}_{\omega} \mathbf{P}) + 2(\tau_{\text{ext},v}^T \mathbf{P}^T \mathbf{C}_{\omega}^T b_f \mathbf{C}_{\omega} \mathbf{P}))}_{\mathbf{f}_f} \tau_{\text{pto},v} \right] \quad (4.26)$$

Which in compact form is given as:

$$E_{\text{har}} = T_s \left[-\tau_{\text{pto},v}^T \mathbf{Q}_f \tau_{\text{pto},v} + \mathbf{f}_f \tau_{\text{pto},v} \right] \quad (4.27)$$

In [22] the reactive controller is designed with an assumed PTO efficiency of $\eta_{\text{pto}} = 0.7$. The reactive controller found in [22] is utilised in the model, and the damping friction

coefficient is chosen such that a PTO efficiency of 0.7 is obtained for sea state 2. This resulted in a friction coefficient of $b_f = 1.1 \cdot 10^6 \left[\frac{Nms}{rad} \right]$. To evaluate the significance of the inclusion of PTO efficiency simulations with and without the PTO efficiency included in the MPC formulation are performed. Hence Equation (4.15) and Equation (4.27) are used as the MPC cost function in the two simulations respectively. The results of the

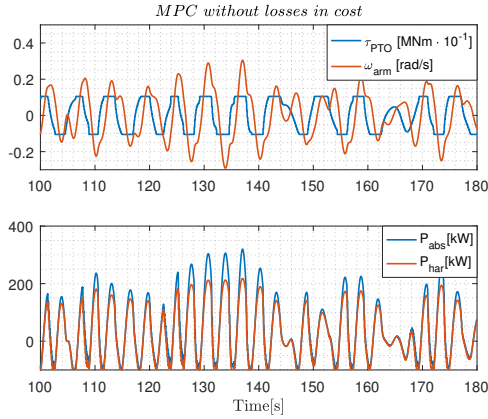


Figure 4.16: Simulation without losses in cost for MPC with $T_s = 0.1s$ and $N = 20$.

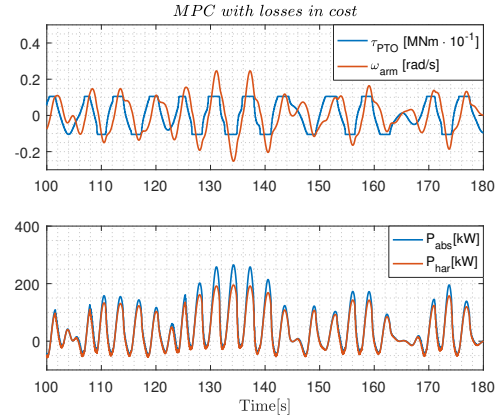


Figure 4.17: Simulation with losses in cost for MPC with $T_s = 0.1s$ and $N = 20$.

two simulations are shown in Figure 4.16 and 4.17. The average absorbed and harvested power for the simulation, is shown in Table 4.1.

MPC type	$P_{abs,avg}[kW]$	$P_{har,avg}[kW]$
MPC without losses in cost	31.8	17.4
MPC with losses in cost	29.9	22.9

Table 4.1: Comparison of the MPC performance with and without losses in the cost function.

From Figure 4.16 and 4.17 the damping friction losses are seen to penalise the reactive power. Significantly less reactive power is seen for the MPC with losses included in the cost function. When including losses in the cost function the absorbed power is lower but the harvested power is higher compared to the MPC without loss included in the cost function. This may indicate that loss should be included in the MPC formulation to increase the average harvested power.

4.2.5 Wave Forecasting

Until now the wave forecasting has been assumed ideal, meaning perfect knowledge of the future waves has been assumed. It is beyond the scope of this thesis to develop an accurate wave forecasting scheme. The wave forecasting presented next is included to indicate the necessary forecasting accuracy, and the significance of forecasting errors. The forecasting is based on an autoregressive (AR) model as proposed in [23], and an excitation torque estimation based on a disturbance observer.

AR Model

A forecast of the incoming wave excitation torque is necessary for the MPC. If it is assumed that the excitation torque may be described by a linear combination of the past values and the parameters a_i , an AR model of the wave excitation torque may be formulated as:

$$\tau_{\text{ext}}(k) = \sum_{i=1}^n a_i \tau_{\text{ext}}(k-i) \quad (4.28)$$

Where n is the order of the AR model, and a_i are the model parameters. The given sea state determines the model parameters of the AR model. This means that the AR model needs to be trained to a given wave data set, and is only valid if the training data represents the current sea state. Thus, if the sea state changes significantly, the AR model needs to be trained on a new data set. The training set is obtained from a time series of estimated wave excitation torque, obtained from the output of a disturbance observer elaborated in Section 4.2.5 over approximately 100 wave periods, as it is expected to reflect the entire frequency range of the given sea state. The trained AR model is thus assumed to represent the sea states for the next 100 wave periods as it is assumed that the sea state does not change significantly during this period. The model parameters are obtained with use of the *ar* function in Matlab, which minimises the sum of squared prediction error.

The future excitation torque may be predicted N steps ahead as:

$$\hat{\tau}_{\text{ext}}(k+N|k) = \sum_{i=1}^n a_i \hat{\tau}_{\text{ext}}(k+N-i|k) \quad (4.29)$$

Where $\hat{\tau}_{\text{ext}}(k+N-i|k) = \tau_{\text{ext}}(k)$ if $k+N-i \leq k$, meaning that the estimate at instant k is known, and the future estimates are based on a mixture of known values and predicted values. For a second order AR model, a two step ahead forecast of the excitation torque may be "lifted" in the same manner as the MPC approach:

$$\hat{\tau}_{\text{ext}}(k+1|k) = a_1 \hat{\tau}_{\text{ext}}(k|k) + a_2 \hat{\tau}_{\text{ext}}(k-1|k) \quad (4.30)$$

$$\begin{aligned} \hat{\tau}_{\text{ext}}(k+2|k) &= a_1 \hat{\tau}_{\text{ext}}(k+1|k) + a_2 \hat{\tau}_{\text{ext}}(k|k) \\ &= (a_1^2 + a_2) \hat{\tau}_{\text{ext}}(k|k) + a_1 a_2 \hat{\tau}_{\text{ext}}(k-1|k) \end{aligned} \quad (4.31)$$

This may be given in matrix notation as:

$$\begin{bmatrix} \hat{\tau}_{\text{ext}}(k+1|k) \\ \hat{\tau}_{\text{ext}}(k+2|k) \end{bmatrix} = \begin{bmatrix} a_1 & a_2 \\ a_1^2 + a_2 & a_1 a_2 \end{bmatrix} \begin{bmatrix} \hat{\tau}_{\text{ext}}(k|k) \\ \hat{\tau}_{\text{ext}}(k-1|k) \end{bmatrix} \quad (4.32)$$

Following this relation the N step ahead forecast may be written as:

$$\hat{\tau}_{\text{ext},v}(k+N|k) = \Upsilon \hat{\tau}_{\text{ext},v}(k-n|k) \quad (4.33)$$

with:

$$\Upsilon = \begin{bmatrix} \mathbf{C}_\tau \mathbf{B}_{\text{ar}} \\ \mathbf{C}_\tau \mathbf{B}_{\text{ar}}^2 \\ \vdots \\ \mathbf{C}_\tau \mathbf{B}_{\text{ar}}^{N-1} \end{bmatrix} \quad \mathbf{B}_{\text{ar}} = \begin{bmatrix} a_1 & a_2 & \cdots & a_{n-1} & a_n \\ 1 & 0 & \cdots & 0 & 0 \\ 0 & 1 & \ddots & \ddots & \vdots \\ \vdots & \vdots & \ddots & 0 & 0 \\ 0 & 0 & \cdots & 1 & 0 \end{bmatrix} \quad \mathbf{C}_\tau = [1 \quad 0 \quad \cdots \quad 0] \quad (4.34)$$

$$\hat{\tau}_{\text{ext},v}(k+N|k) = [\hat{\tau}_{\text{ext}}(k+1|k) \quad \hat{\tau}_{\text{ext}}(k+2|k) \quad \cdots \quad \tau_{\text{ext},k+N}]^T \quad (4.35)$$

$$\hat{\tau}_{\text{ext},v}(k-n|k) = [\hat{\tau}_{\text{ext}}(k|k) \quad \hat{\tau}_{\text{ext}}(k-1|k) \quad \cdots \quad \hat{\tau}_{\text{ext}}(k-n|k)]^T \quad (4.36)$$

As the excitation torque is unmeasurable it needs to be estimated. The estimation of the excitation torque is elaborated in the next section.

Excitation Torque Estimation

The estimation of the wave excitation torque is formulated as a linear disturbance observer, as proposed in [24]. Using the linear point absorber model, a disturbance observer may be configured as shown in Figure 4.18.

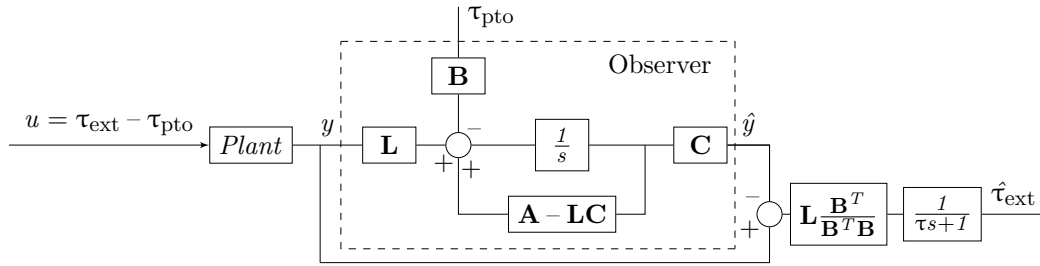


Figure 4.18: Diagram of disturbance observer.

An observer may be formulated with only the PTO torque as input. The estimation of the excitation torque may then be driven by the error between measured outputs and observed outputs with only the PTO torque as input. The observer state equation with only the PTO torque as input may be formulated as[21]:

$$\hat{\dot{\mathbf{x}}} = \mathbf{A}\hat{\mathbf{x}} - \mathbf{B}\tau_{\text{pto}} + \mathbf{L}(y - \hat{y}) \quad (4.37)$$

Where \mathbf{L} is the observer gain matrix. As the excitation torque act as an additional input to the system, the "true" state equation may also be written as:

$$\dot{\mathbf{x}} = \mathbf{A}\mathbf{x} - \mathbf{B}\tau_{\text{pto}} + \mathbf{B}\hat{\tau}_{\text{ext}} \quad (4.38)$$

From Equation (4.37) and (4.38) the estimated excitation torque may be formulated as:

$$\hat{\tau}_{\text{ext}} = \frac{\mathbf{B}^T}{\mathbf{B}^T\mathbf{B}}\mathbf{L}(y - \hat{y}) \quad (4.39)$$

Where $\frac{\mathbf{B}^T}{\mathbf{B}^T\mathbf{B}}$ is imposed to obtain the inverse value of each element of \mathbf{B} . From Equation (4.39) the excitation torque estimation is given by the error dynamics, $y - \hat{y}$. The observer gain matrix \mathbf{L} is designed with use of the kalman function of Matlab. The gain matrix is designed such the dynamics of Equation (4.39) is dominated by the plant dynamics in y , hence the poles of Equation (4.37) is much faster than the plant dynamics. As high frequency content may be present in y at each force shift of the PTO cylinder, $\hat{\tau}_{\text{ext}}$ is low pass filtered with a first order low pass filter with a cut off frequency such that the dominating frequency content in τ_{ext} is ensured.

In Figure 4.19 the estimated excitation torque is shown for a simulation for sea state 1, with MPC applied as WPEA.

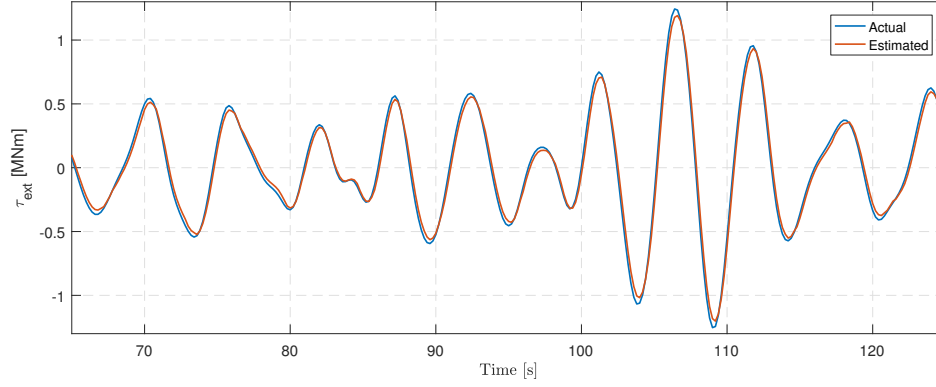


Figure 4.19: Actual and estimated wave excitation torque.

In Figure 4.20 forecasting of the wave torque at three instants is shown. Here the AR model is trained on the observed excitation torque for the same sea state sampled with the same sample time as the MPC. An order of $n = 40$ is used meaning that the forecast is based on 40 previous samples. The wave is forecasted 5 seconds forward in time. As evident from the figure the wave prediction may be used for forecasting of approximately 2-3 seconds. Other methods for forecasting the wave torque may be possible, however better wave forecasting is out of the scope for this thesis, and serves just as an indicator of what might be achievable with unknown wave torque. An accurate forecast of the wave far into the horizon may not be necessary as these have lower impact on the optimal PTO torque applied at time $t = k$.

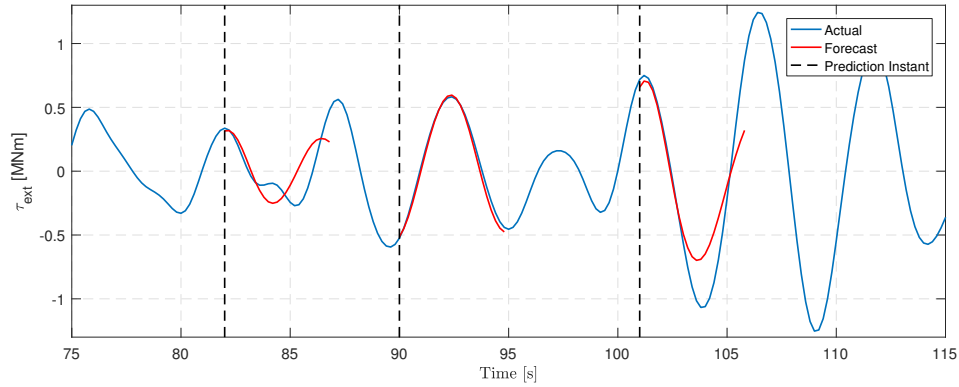


Figure 4.20: Actual and predicted wave excitation torque. At each prediction instant the future wave torque is predicted based on previous 40 observations.

To measure the accuracy of the wave forecasting the following "goodness of fit" at every prediction instant k is used, where a normalised root mean square error is calculated as:

$$\sigma(k) = 1 - \frac{\|\tau_{\text{ext}}(k+n|k) - \hat{\tau}_{\text{ext}}(k+n|k)\|}{\|\tau_{\text{ext}}(k+n|k) - E\{\tau_{\text{ext}}(k+n|k)\}\|} \quad (4.40)$$

$\sigma(k)$ is the goodness of fit indicator and is a number in the region $[-\infty : 1]$. $\sigma(k) = -\infty$ is a bad fit and $\sigma(k) = 1$ is a perfect fit. $\|\cdot\|$ indicates the euclidean norm of a vector, $E\{\cdot\}$ indicates the mean of a vector and $n = 1 \dots N$ where N is the horizon length. A histogram

of the goodness of fit for a forecast of ten steps for a waves series is shown in Figure 4.21. To give a visual example of the goodness of fit two examples with a goodness of fit with 0.86 and -1.95 respectively are shown in Figure 4.22.

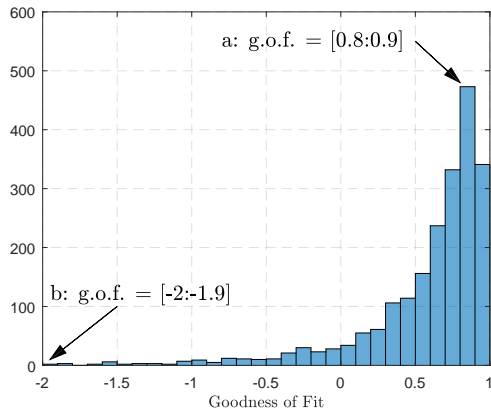


Figure 4.21: Histogram of $\sigma(k)$ for a 10 step ahead forecasting at every prediction instant k .

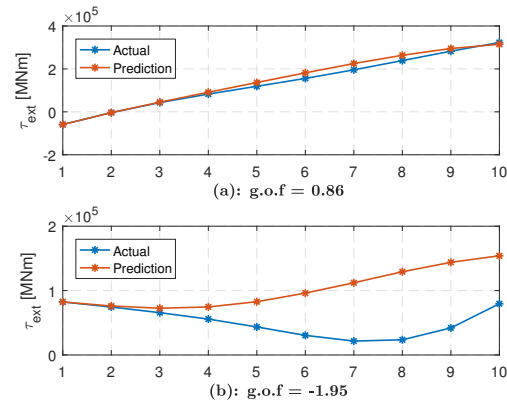


Figure 4.22: Visual example of $\sigma(k)$ with the values 0.86 and -1.95 respectively.

In general the AR forecasting method shows good performance. For the example shown above an average goodness of fit of 0.56 is obtained. To investigate the significance of the forecasting accuracy a simulation is performed with wave forecasting included in the MPC formulation for three different sea states. In Figure 4.23-4.25 the difference in average harvested power with respect to ideal wave prediction, and wave forecasting based on the AR model is shown. The simulations are performed with a MPC sample time of 0.1s.

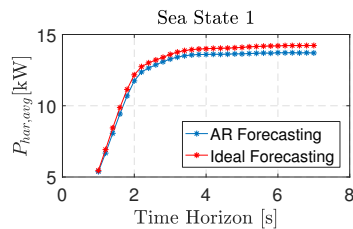


Figure 4.23: Average harvested power with ideal and estimated future excitation torque forecasting for SS1.

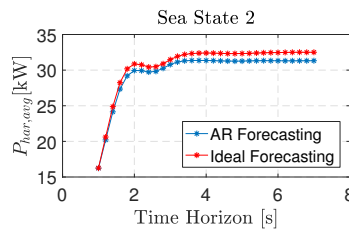


Figure 4.24: Average harvested power with ideal and estimated future excitation torque forecasting for SS2.

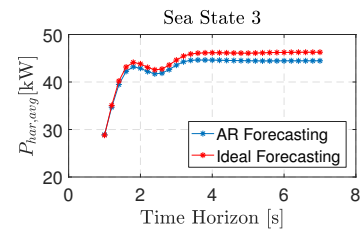


Figure 4.25: Average harvested power with ideal and estimated future excitation torque forecasting for SS3.

As evident from the figures, the AR model can provide acceptable performance with respect to average harvested power compared to ideal forecasting. Even at longer horizon lengths the difference between perfect knowledge and estimation is small with only a reduction in average harvested power of approximately 4%.

4.3 Part Conclusion

It was found that for regular waves the MPC solution approaches the analytical optimal solution as the sample frequency and horizon length goes towards infinity. This indicates that MPC of the point absorber may provide optimal power extraction of the waves. No significant improvement of the MPC was found past horizon length of approximately 4s, however the MPC sample time should be reduced as much as possible. To lower the computational demand of the MPC, a truncated model for the MPC formulation was found suitable if the damping coefficient is chosen appropriately. Simple losses were imposed in the PTO system to investigate the significance with respect to harvested energy. It was found that losses should be included in the MPC formulation to increase the average harvested energy. A simple AR model was proposed for forecasting the future excitation torque and it was shown. The AR forecasting may provide close to ideal performance, with only a reduction in average harvested power of 4%.

5 | Quantized Input MPC

As explained in Section 1.1 the discrete displacement PTO system for the Wave Star WEC is effectively a system with quantized inputs. So far the MPC has been formulated with the assumption of the PTO system able of applying continuous forces on the point absorber. In this chapter, a MPC scheme able of handling the discrete nature of the PTO system is developed. Considerations regarding the control formulation is done, as well as the formulation of cost functions including the losses described in Section 3.4. It is desired to use the linear point absorber model in the MPC, why a suitable transformation from PTO cylinder space to absorber space will be considered. The choice of cost function variable is presented next, as the discrete displacement PTO system allows different formulations.

5.1 Cost Function Variable

The PTO force is obtained by connecting the cylinder chambers to either a low, medium, or high pressure line through a manifold of nine DFCUs. The configuration allows different system input formulations. Choosing the pressure level in each chamber as input, the system is effectively a multiple input single output (MISO) system, where the inputs are the pressure level in each chamber of the PTO cylinder. By formulating the MPC with the MISO approach, the cost function variables would be the pressure level in each of the three cylinder chambers.

A second approach is to formulate it as a SISO system with the PTO cylinder force as input. Thus, the output of the MPC is a force belonging to the set of available forces. An additional mapping from force level to required chamber pressures is thus required by this choice of MPC formulation.

It is chosen to formulate the MPC using the SISO approach with the cost function variable being an integer between 1 and 27 corresponding to a PTO cylinder force. The SISO approach results in fewer design variables in the cost function formulation, as only one variable is to be computed at each time step compared to three with the MISO approach. However, it is not believed that any advantage is gained from this formulation as the number of possible solutions at each time step remains the same for the two approaches. The SISO approach is chosen for simplicity of the cost function formulation and easy incorporation of estimated losses by lookup tables which will be utilised to decrease the computational demand of the MPC cost function.

5.2 Absorber to Cylinder Space

So far, the MPC has been investigated in the point absorber space, computing the optimal PTO torque at each time step. It is desired to base the MPC on the linear point absorber model, why a transformation from torque to cylinder force is required for the MPC formulation. As shown in Section 3.1.2 the moment arm of the point absorber is a nonlinear function of the cylinder stroke x_c . As a simple MPC formulation is desired, the relation is evaluated in the middle position of the PTO cylinder, yielding a constant moment arm. The deviation of the approximation from the true value as function of the cylinder stroke is shown in the figure below.

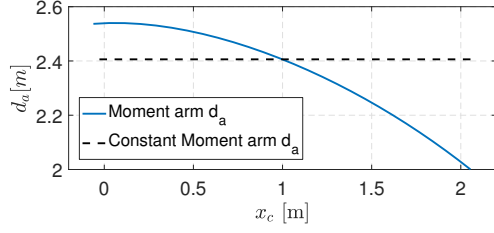


Figure 5.1: The moment arm as function of the cylinder stroke and an indication of the constant moment arm.

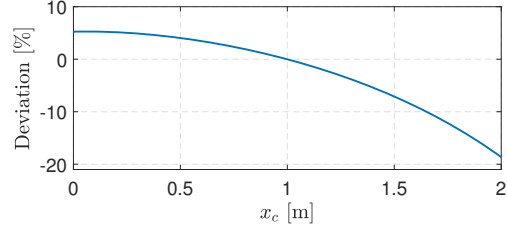


Figure 5.2: The deviation of the constant moment arm from the true moment arm as function of the cylinder stroke.

From simulations it is seen that the cylinder stroke mostly operates within 0.5m to 1.5m. With a cylinder stroke of 1.5m a deviation from the true moment arm is only 6.5% why the approximation is regarded fair.

With a constant moment arm, a 1D lookup table containing the discrete PTO torques available for the optimisation algorithm is formulated. The discrete PTO forces obtained from shifting between the chamber pressures are calculated and sorted in ascending order as shown in Figure 3.11 and converted to resulting torques by means of the constant moment arm. The force level output from the MPC is then mapped to corresponding valve signals by a mapping function as shown in Figure 5.3.

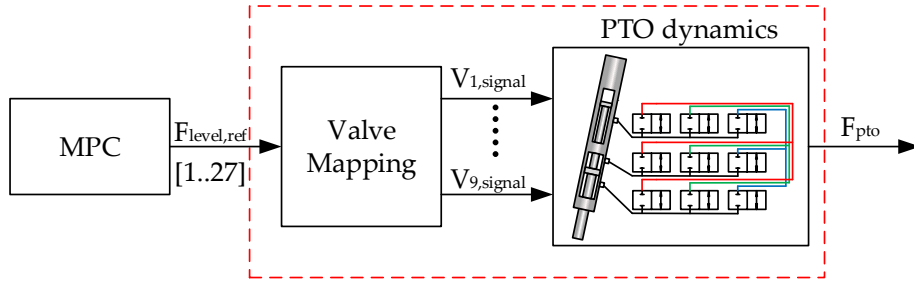


Figure 5.3: Force level reference to valve position mapping. Red dashed line indicates force dynamics which are not included in the MPC formulation.

Formulating the MPC as shown in chapter 4, the PTO and valve dynamics are not included in the MPC formulation. This imposes delays from the force reference computed by the MPC to the actual force which is not explicit considered in the MPC formulation. The delays are addressed in Section 5.3. In Figure 3.7, the kinematics describing the transformation from absorber space to PTO cylinder is shown. The kinematics may be linearised without large deviation as the relation shown in Figure 3.7 is almost linear, why the relation is linearised for simplicity. . The transformation is thus approximated with a maximum deviation of 2% from the true relation of Equation (3.12) as:

$$x_c \approx \left. \frac{dx_c}{d\theta_{\text{arm}}} \right|_{\theta_{\text{arm}}=0} \Delta\theta_{\text{arm}} + x_{c,0} = -k_{d2x}\theta_{\text{arm}} + x_{c,0} \quad (5.1)$$

5.3 MPC Sample Time

In this section, the sample time of the MPC is considered. At each force shift, the PTO cylinder chamber pressures are controlled such that a constant pressure gradient is obtained during a pressure shift. This is obtained by shaping the valve opening trajectories as described in [7]. The valve opening trajectories impose delays from the force reference computed by the MPC to the actual force applied by the PTO cylinder. The valve opening trajectories are introduced to reduce pressure oscillation, why short delays in the PTO force may be seen as a trade off to higher pressure oscillations. As the PTO force delays are not explicitly accounted for in the MPC formulation, these are addressed in the following.

5.3.1 Pressure Dynamics

To consider the delays a simple model from the pressure line to the cylinder chamber is investigated. Considering a fixed volume and hose, the pressure dynamics in the volume may be described as:

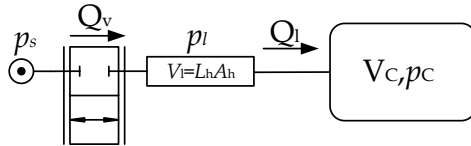


Figure 5.4: Model of a fixed volume chamber and hose.

$$Q_v = x_{v,eq} n_1 k_v \sqrt{p_s - p_l} \quad (5.2)$$

$$\dot{Q}_l = \frac{(p_l - p_c) A_h}{\rho L_h} \quad (5.3)$$

$$\dot{p}_l = \frac{\beta}{V_{l,0}} (Q_v - Q_l) \quad (5.4)$$

$$\dot{p}_c = \frac{\beta}{V_{c,0}} Q_l \quad (5.5)$$

The characteristics of the simple model are defined by the chamber volume, hose length and diameter and the bulk modulus. Fast switching between the pressure lines results in excitation of the system dynamics, why pressure oscillations may occur. To avoid pressure oscillations, slower switching may be applied, however as mentioned this imposes delays in the PTO force. Different switching times are tested on the model to test how fast the switching may be chosen to obtain acceptable oscillations. The valve opening trajectories are computed based on the shifting algorithm described in [7]. The simulations are performed for a cylinder stroke of $x_c = 1m$, fixed volume and a pressure shift from 100bar to 200bar. The simulation results are shown in Figure 5.5 and 5.6 for the pressure shift performed in chamber one of the PTO cylinder, as this yields the highest pressure oscillations due to the hose connected to this chamber is approximately four times longer than the other hoses. As evident from the simulation of the simple fixed chamber model, a faster switching results in higher pressure oscillations. From the simulations it may be seen that smooth pressure transition without oscillations may be obtained by choosing pressure development times of 150ms and 200ms. Slower switching may also be shown to increase switching losses [7]. The pressure development time is chosen as a compromise between force delay, pressure oscillations and switching losses. As the pressure shifting is desired as fast as possible, a pressure development of 50ms is chosen, as this only introduces small oscillations when shifting.

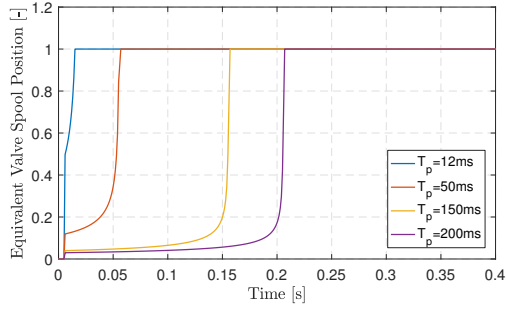


Figure 5.5: Opening trajectories for valve to reduce pressure oscillation in the cylinder chamber.

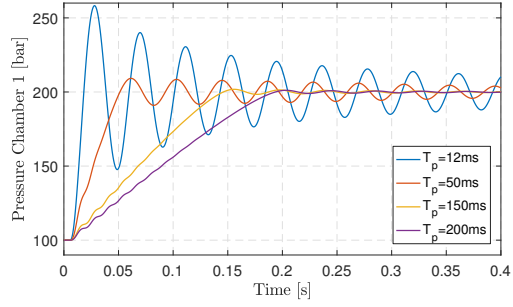


Figure 5.6: Simulated chamber pressure for a shift from 100bar to 200bar for different valve opening trajectories.

From this it may be concluded that a minimum switching time between each chamber pressure shift must be formulated, to allow the PTO force to fully develop before the next MPC sample, and must be considered when designing the MPC. A minimum switching time between each force of 0.1s, corresponding to a MPC frequency of 10Hz. By this the requested force from the MPC is obtainable within half of the minimum switching period. The minimum switching time could be obtained by imposing a constraint in the MPC formulation, or by choosing the sample time of the MPC to 0.1s. The second approach is chosen. From Figure 4.15 it is seen, that a sample time of 0.1s may be chosen without significant reduction in performance of the MPC. Given the complexity of the MPC cost function, a MPC sample time of 0.1s may not be realisable. For this reason an upper limit on the MPC sample time is formulated as well. Based on the MPC analysis performed in Section 4.2 the maximum MPC sample time is chosen as 0.35s. Thus it is desired to run the MPC with a sample time as close to 0.1s as possible, however if this is not possible a maximum sample time of 0.35s is set as a requirement.

5.4 Cost Functions

In this section, four cost functions for the MPC is formulated. It is desired to evaluate the harvested energy subject to different model complexities used in the MPC. The model complexity will be expressed in the amount of losses included in the cost function. Common for the different cost functions is that they are minimised with no constraints on the state variables for the reasons discussed in Section 4.1.1.

5.4.1 No Loss

Including no losses in the cost function corresponds to maximising the absorbed energy of the point absorber over the time horizon of the MPC. Using the same approach as in Section 4.1 the cost function that maximises the absorbed energy over the time horizon is given as:

$$\underset{\tau_{pto,v} \in \tau_{available}}{Min} \left(T_s \left[\tau_{pto,v}^T \mathbf{Q} \tau_{pto,v} - \mathbf{f} \tau_{pto,v} \right] \right) \quad (5.6)$$

Where $\tau_{available}$ is the set of 27 PTO torques which may be applied by the PTO cylinder. \mathbf{Q} and \mathbf{f} are derived in the same manner as in Section 4.1.

5.4.2 Static Shifting Losses

A simple form of loss inclusion in the cost function is by adding an additional term in the cost function approximating the force shifting losses in a lookup table. As shown in Section 3.4 the shifting losses are a function of the chamber pressures and volumes. To avoid having the MPC predicting the future chamber volumes, the shifting loss may be approximated by a lookup table evaluated in a cylinder position $x_{c,0}$. By summation of the compression loss in each chamber according to Equation (3.39), the energy loss associated with a single force shift is calculated as:

$$E_{loss,\beta} = \frac{1}{2}(p_{1,new} - p_{1,old})^2 \frac{V_1(x_{c,0})}{\beta} + \frac{1}{2}(p_{2,new} - p_{2,old})^2 \frac{V_2(x_{c,0})}{\beta} + \frac{1}{2}(p_{3,new} - p_{3,old})^2 \frac{V_3(x_{c,0})}{\beta} \quad (5.7)$$

As 27 different PTO forces may be produced, a 27x27 lookup table containing the compression loss from every possible force shift is computed and is denoted $E_{loss,\beta}(i, j)$, where i is the current force level and j is the new force level. The lookup table is computed for a cylinder stroke of $x_{c,0} = 1m$. Due to the choice of cost function variable as an integer between 1 and 27, the lookup table can be included without the need of additional transformation. The cost function may thus be formulated as:

$$\underset{\tau_{pto,v} \in \tau_{available}}{Min} \left(T_s \left[\tau_{pto,v}^T \mathbf{Q} \tau_{pto,v} - \mathbf{f} \tau_{pto,v} \right] + \sum_{i=1}^N E_{loss,\beta}(\tau_{pto,v}(i-1), \tau_{pto,v}(i)) \right) \quad (5.8)$$

Where $\tau_{pto,v}(0)$ is the force level from the previous iteration.

5.4.3 Static Shifting Losses and Throttling Loss

To include throttling losses in the cost function an additional term is added to Equation (5.8) describing the throttling loss over the time horizon. The instantaneous power loss from flow throttling is given in Equation (3.47), thus the cost function with throttling losses may be written as:

$$\underset{\tau_{pto,v} \in \tau_{available}}{Min} \left(T_s \left[\tau_{pto,v}^T \mathbf{Q} \tau_{pto,v} - \mathbf{f} \tau_{pto,v} + (|y_\omega k_{d2x}|)^T \Gamma (|y_\omega k_{d2x}| \circ |y_\omega k_{d2x}|) \right] + \sum_{i=1}^N E_{loss,\beta}(\tau_{pto,v}(i-1), \tau_{pto,v}(i)) \right) \quad (5.9)$$

Where $y_\omega = \mathbf{C}_\omega \chi_{k+}$ is the future predicted angular velocity of the float arm, $\Gamma = \sum_{i=1}^3 \frac{A_i^3}{(n_i k_v)^2}$ is the throttling loss coefficient, \circ denotes the component wise multiplication and k_{d2x} is the linearisation coefficient computed from Equation (5.1) mapping the predicted absorber angular velocities to predicted PTO cylinder velocities.

5.4.4 Complete Losses

A complete loss model is investigated to compare with the other cost functions. Both the static and dynamic shifting loss and throttling loss are included based on future

estimated states. Thus according to the losses elaborated in Section 3.4 the cost function that maximises the harvested energy over the MPC time horizon may be formulated as:

$$\begin{aligned}
\underset{\tau_{\text{pto},v} \in \tau_{\text{available}}}{\text{Min}} \left(T_s \left[\tau_{\text{pto},v}^T \mathbf{Q} \tau_{\text{pto},v} - \mathbf{f} \tau_{\text{pto},v} + \sum_{i=k}^{k+N} \sum_{j=1}^{\mathcal{J}} \frac{|A_j v_c(i)|^{\mathcal{J}}}{(n_j k_v)^{\mathcal{J}}} \right] \right. \\
+ \sum_{i=k}^{k+N} \sum_{j=1}^{\mathcal{J}} \left(\frac{1}{2} (p_{j,\text{new}} - p_{j,\text{old}})^2 \frac{V_j(i)}{\beta} + \frac{1}{2} (p_{j,\text{new}} - p_{j,\text{old}}) \dot{V}_j(i) T_p \right. \\
\left. \left. + \frac{1\mathcal{J}}{70} (p_{j,\text{new}} - p_{j,\text{old}})^2 \frac{\dot{V}_j(i)}{\beta} T_p \right) \right) \quad (5.10)
\end{aligned}$$

A drawback of the cost function including complete losses is that the future system states has to be computed to calculate the complete loss. Compared to the cost functions estimating the loss by a lookup table additional computations has to be done which increases the computational time.

5.5 Optimisation Algorithm

After formulating the discrete MPC an optimisation algorithm capable of handling discrete design variables is required. As the design variables of the optimisation are no longer continuous, strictly gradient based optimisations algorithms can no longer be used to solve the MPC problem. In order for real time implementation of the MPC to become feasible, a fast and efficient optimisation algorithm needs to be incorporated in the MPC. To choose a suitable optimisation algorithm, a comparison of two optimisation algorithms able of handling discrete variables is done. The first algorithm is based on the Branch and Bound principle. The second algorithm is a genetic algorithm called differential evolution. Branch and Bound is a well known method for discrete optimisation but may have certain drawbacks such as dealing with nonlinearities. Differential evolution is an algorithm based on evolutionary principles which can handle complex problems such as discrete optimisation problems. In section 5.3 it was found that the sample time of the MPC should be chosen as close to 0.1s as possible but no larger than 0.35s. A requirement for the optimisation algorithm is thus to converge to a solution within 0.35s. Ideally the optimisation algorithm finds the optimal solution for all instances but this may not be possible if the requirement for the computational time should be met. It may be necessary to compromise with the consistency of the optimisation algorithm to obtain lower sample time. In the following the comparison of the two algorithms are elaborated.

5.5.1 Optimisation Algorithm Evaluation

The performance of the optimisation algorithm will be based on the time spend to find the optimum and how often the true optimum is found. For this purpose, a scenario where the true optimum is known is established. Thus, if a problem formulation for the optimisation is setup where true optimum is known, the optimisation algorithms may be benchmarked against each other. The optimisation algorithms are benchmarked for a scenario, where the time horizon for the MPC control is one second, and the sample time is 0.1s. Thus, for the given scenario 10 design variables is to be found which should

yield the maximum harvested energy during the given time span. The simplified point absorber model described in Equation (4.23) is utilised for simplicity.

To further simplify the scenario, the PTO force is assumed to only take 9 discrete values, evenly distributed between $\pm 420kN$. This corresponds to a PTO torque evenly distributed between $\pm 1MNm$ when choosing a constant moment arm of $2.4m$. The simplified point absorber model is subjected to an arbitrary chosen excitation torque generated with the provided wave generator, and an initial condition of $x_0 = [0 \ 0]^T$ is chosen.

To find the combination of PTO torques which yields the maximum harvested energy, the simplified model is simulated over 1 second subject to every possible combination of PTO moments, where the PTO moment can take 9 discrete values, and may shift every 0.1 second. This gives in total $9^{10} \approx 3.48 \cdot 10^9$ possible combinations, which is brute forced in Matlab. The brute force routine was performed on a desktop PC with a i5 Intel core CPU with a clock frequency of 3.4GHz and took approximately 37 hours and 13 minutes. A diagram of the brute force routine is shown in Figure 5.7.

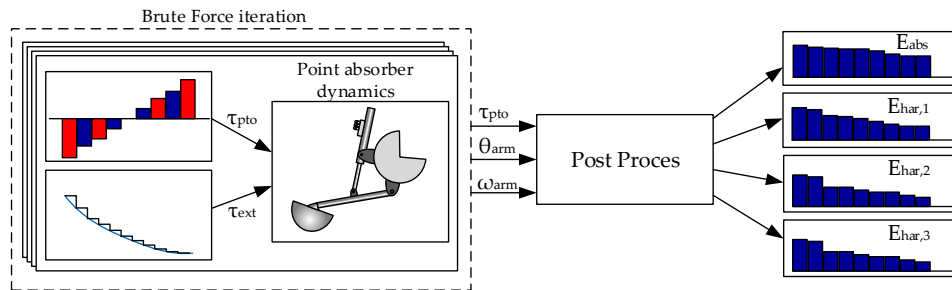


Figure 5.7: Diagram of the performed brute force routine. Every combination of PTO torques during 1s with a sampling period of 0.1s is simulated and post processed to find combination of PTO torques which yields maximum energy harvested.

For the incoming excitation torque and each combination of PTO torques the point absorber position and velocity is saved for post-processing. The post-processing consist of calculation of harvested energy. To compare different loss mechanism influence of the optimal PTO torque trajectory, four different scenarios are compared. The four scenarios are listed below including different losses in the PTO system.

- E_{abs} : No loss included, only absorbed energy
- $E_{har,1}$: Static shifting loss included
- $E_{har,2}$: Static and dynamic shifting loss included
- $E_{har,3}$: Static and dynamic shifting loss and throttling loss

For the four scenarios the harvested energy is calculated based on the brute force solution

as:

$$E_{\text{abs}} = T_s \sum_{k=1}^{\frac{T_{\text{sim}}}{T_s}} \omega_{\text{arm}}(k) \tau_{\text{pto}}(k) \quad (5.11)$$

$$E_{\text{har},1} = E_{\text{abs}} - \sum_{n=1}^2 \sum_{k=1}^{\frac{T_{\text{sim}}}{T_s}} \frac{1}{2} \Delta p_n(k)^2 \frac{V_n}{\beta} \quad (5.12)$$

$$E_{\text{har},2} = E_{\text{har},1} - \sum_{n=1}^2 \sum_{k=1}^{\frac{T_{\text{sim}}}{T_s}} \left(\frac{1}{2} \Delta p_n(k) \dot{V}_n T_p - \frac{13}{70} \Delta p_n(k)^2 \frac{\dot{V}_n}{\beta} T_p \right) \quad (5.13)$$

$$E_{\text{har},3} = E_{\text{har},2} - \sum_{n=1}^2 \sum_{k=1}^{\frac{T_{\text{sim}}}{T_s}} \frac{|A_n v_c(k)|^3}{(n_n k_v)^2} \quad (5.14)$$

Where T_s is the sample period chosen as 0.1s, T_{sim} is the simulation time chosen as 1s, $\Delta p_n(k)$ is the pressure difference in the n'th chamber after each sample period. Δp_n is computed from a lookup table with current and previous force levels as input for a secondary controlled asymmetric cylinder configuration shown in Figure 1.3. T_p is the pressure development time in the cylinder chambers, and is chosen to 50ms. A_n is the piston area of the n'th chamber, n_n is the number of valves used in the DFCU connected to the n'th chamber, k_v is the fitted valve gain of the valves used in the DFCUs and $v_c(k)$ is the cylinder velocity at sample time k. The geometry and chamber volumes are assumed equal to chamber one and two of the PTO cylinder of the test bench modelled in Section 3.3.

The combinations of PTO torques is ranked against most harvested energy. In Figure 5.8 the three best solutions of PTO torques with respect to harvested energy is shown along with point absorber velocity and excitation torque for each loss scenario.

From Figure 5.8 it may be seen that introducing losses yields fewer force shifts compared to the case with no losses included.

Introducing the dynamic compression losses at each force shift according to Equation (5.13), does not change the optimal PTO torque trajectory compared to the scenario only including static shifting losses. The optimal solution for the case with throttling losses included is seen to have a lower absorber velocity compared to the solutions of the other scenarios. In Figure 5.9 the ten highest ranked scenarios which yielded the most harvested energy are shown. The harvested energy for the four different loss scenarios are normalised to the maximum absorbed energy for easier comparison. From the figure it is evident that when no losses is included, the difference in harvested energy for the ten best trajectories is relatively low. This may suggest that finding the best solution when no losses are included are of less importance due to the relatively low difference in the ten best solution. Finding the best solution when losses are included in the cost function is shown to be important, as the difference between the ten best solution are larger compared to no losses.

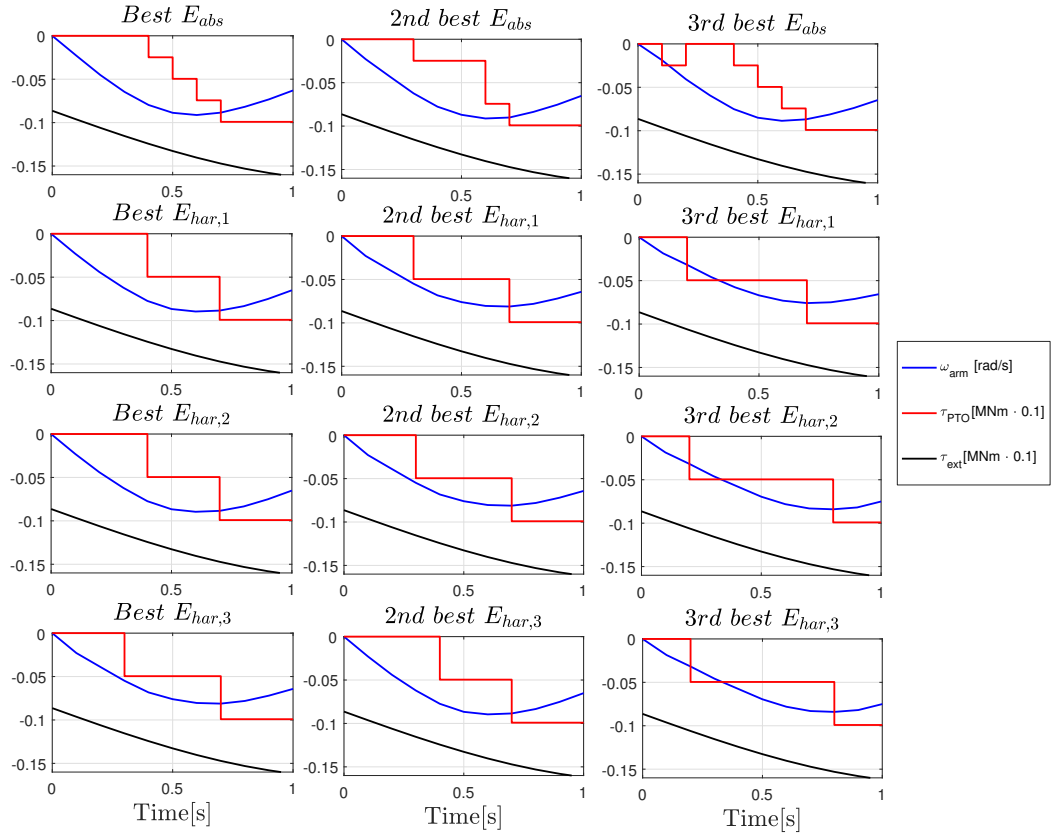


Figure 5.8: PTO torque trajectories which yields the three highest amounts of harvested energy for the four different loss scenarios.

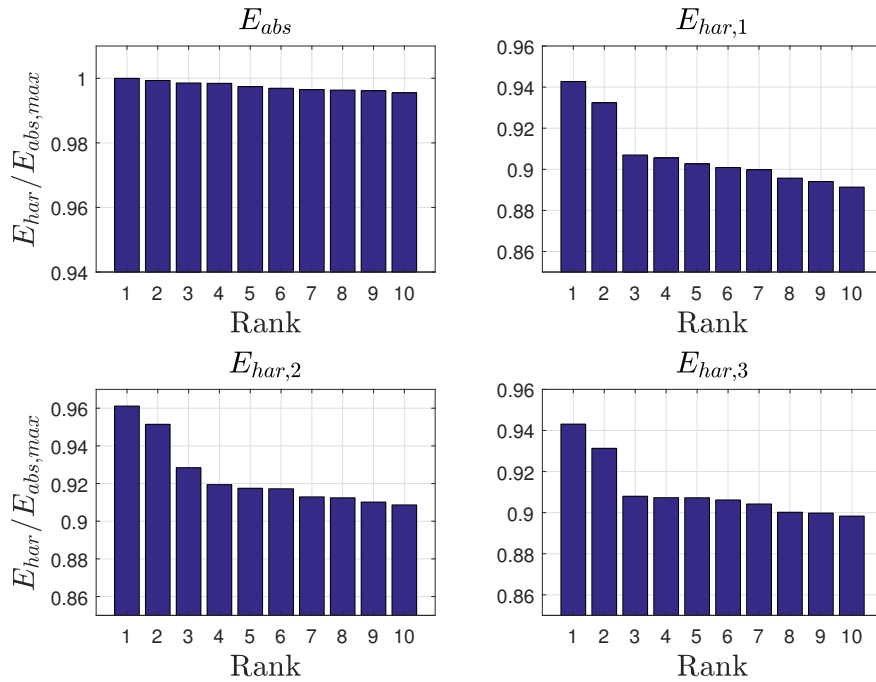


Figure 5.9: Ten highest normalised harvested energy for the four different loss scenarios.

As the ten best PTO torque trajectories for different loss scenarios are known, the optimisation algorithms may be tested to investigate if the optimum is found, how often it is found, and the time to find the optimum.

5.5.2 Comparison of Optimization Algorithm Performance

Two optimization algorithms suited for discrete variables are compared. The first is an optimization algorithm based on Branch & Bound (BnB), the other is a Differential Evolution (DE) which is a genetic algorithm. The BnB algorithm is a modified version of the BNB20 algorithm accessible from the Mathworks file exchange library[25]. The BNB20 algorithm solves a mixed integer problem by first solving the relaxed problem, then searching for the optimal solution by estimating upper and lower bounds of the optimal solution and then enumerating candidate solutions between the bounds. DE is based on a "survival of the fittest" approach, where an initial population is evolved through generations.

It is desired to test the optimization algorithms' sensitivity to the initial guess of the PTO torques for the optimization problem, why the initial guess is chosen randomly. An optimization problem is set up for the same scenario as the brute force scenario, and the four different loss scenarios are included as well. For all loss scenarios the static shifting loss described in equation 5.12 is estimated by a lookup table where the shifting loss is calculated for a cylinder stroke of $x_c = 1$.

The optimization may be seen equivalent to a MPC calculation at $t = 0$ with perfect knowledge of the future excitation torque. As in the brute force scenario, the PTO torque may shift every 0.1s, hence the model of Equation (4.23) is discretized with a zero order hold with a sample period of 0.1s.

The optimization problem is then solved with BnB and DE respectively. To test the performance, the problem is solved 1000 times, with a random generated initial guess for each iteration. The performance of the two algorithms are summarized in Table 5.1. The performance test is performed on a laptop PC with an i7 2.70GHz processor. The time to solve the optimization problem is obviously depended on the hardware used to solve the problem, why the time shown in the table should be reviewed relative to each other.

<i>Algorithm</i>	<i># Best found</i>	<i># 2nd best found</i>	<i>Average Time</i>	<i>Max Time</i>
Branch & Bound				
E_{abs}	1000	0	0.627s	1.876s
$E_{har,1}$	803	9	0.711s	2.161s
$E_{har,2}$	724	9	0.681s	2.215s
$E_{har,3}$	787	10	0.776s	2.310s
Differential Evolution				
E_{abs}	1000	0	0.146s	0.210s
$E_{har,1}$	994	0	0.286s	0.695s
$E_{har,2}$	929	0	0.627s	1.029s
$E_{har,3}$	941	0	0.648s	0.996s

Table 5.1: Comparison of the two optimization algorithms.

Based on the results shown in Table 5.1 it is concluded that the DE algorithm performs

better than the BnB algorithm. The lowest success rate of the DE is 92.9% compared to the lowest success rate of the BnB algorithm which is 72.4%. A reason for the low success rate for BnB may be the discontinuities introduced by the lookup table for the static shifting loss. Inconsistency in the BnB algorithm is expected with lookup tables, since a gradient based search algorithm is used to solve the relaxed problem. The relaxed solution found by the gradient based optimization algorithm is dependent of the initial guess why the optimal solution is not found at all times. This may also indicate that BnB is not suited for solving the optimisation problem when introducing losses by a lookup table.

The most crucial parameter for the performance is the time to find the optimum, as the optimization algorithms are to be implemented in an online MPC scheme. The DE algorithm also outperforms the BnB algorithm on this parameter for the cases where the objective function are E_{abs} and $E_{\text{har},1}$. The high success rate of the DE algorithms also suggest that it is not as sensitive to initial guess as the BnB algorithm. A drawback for both algorithms is that the optimal solution cannot be guaranteed. The brute force analysis indicates that multiple solutions are close to the optimal solution. Due to this it may not be necessary to find the actual optimum and may be sufficient to find one of the best solutions as long as the first control input is the same, as this is the actual applied control input. The benchmark of the optimisation algorithms suggests however that DE is capable of finding the optimal solution 92.9% of the time in the worst case scenario, which may indicate that DE is suitable for the MPC algorithm. Further it may be seen that the cost functions with no loss or loss included as a lookup table is significant faster to solve compared to the cost functions with calculated loss. This may indicate that losses should be included by lookup tables to minimise the computational time. DE is chosen as optimisation algorithm and will be used in the MPC for the remaining thesis. The convergence time of the DE algorithm is considered next subject to the horizon length.

5.6 Convergence time

The sensitivity of the DE algorithm with respect to the horizon length is addressed. As the DE is not based on gradient based search direction, the convergence time of the DE algorithm is expected to increase exponentially with the horizon length N , as the solution space increases with F_n^N , where F_n is the number of force levels. To test the significance of the horizon length the DE is solved with different horizon lengths for the same scenario as the brute force scenario. In the scenario only static shifting loss is included by a lookup table. Thus, the MPC is solved with a time horizon of 1s, and 9 force levels available, but with different sample times to increase the number of design variables for the optimization algorithm. The true optimum for other sample times is unknown, however the DE algorithm is tuned in terms of number of population members until a solution that resembles the solution with a sample time of 0.1s is found. In Figure 5.10 the solutions found with different horizon lengths is shown, and the corresponding convergence times are shown in Table 5.2. For each horizon length, the number of members in each population is increased to ensure that the DE does not converge prematurely.

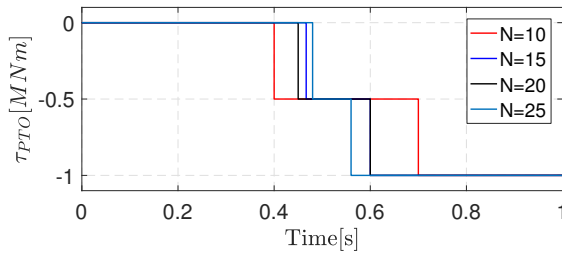


Figure 5.10: Solution of DE subject to different horizon lengths N .

Horizon	Convergence Time
$N = 10$	$T = 0.31s$
$N = 15$	$T = 9.48s$
$N = 20$	$T = 107s$
$N = 25$	$T = 1473s$

Table 5.2: Convergence time for DE for multiple horizon lengths.

As evident the convergence time increase significantly with the horizon length N . From this it may not be practically possible to run the MPC with a horizon length above $N = 10$, if the requirement of a maximum sample time 0.35s should be fulfilled. Modifications of the DE is done to optimise its performance. The standard differential evolution algorithm used is presented in the next section, to allow clarification of what modifications is done to the algorithm to obtain faster convergence time.

5.7 Differential Evolution Algorithm

Differential evolution is an evolutionary algorithm capable of performing global optimisation of non differentiable objective functions. DE was first developed in [26].

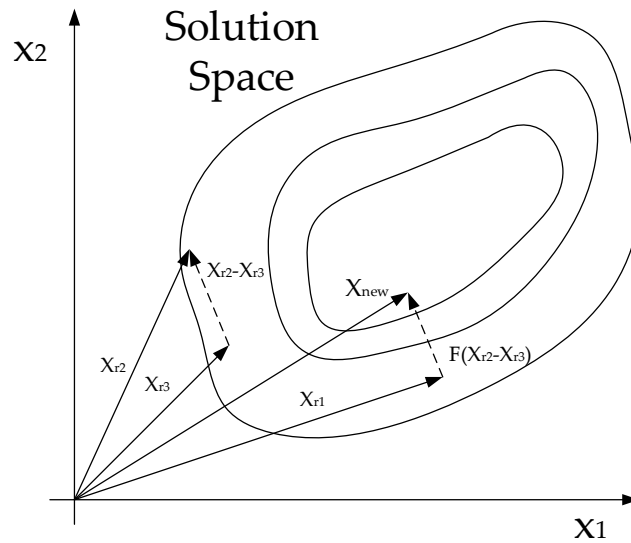


Figure 5.11: Illustration of the procedure for a basic variant of differential evolution.

The general idea is to generate a population of candidate solutions called members and then relocate the members in the solution space by generating new members from existing members by mutation. In Figure 5.11 the generation of a new member is illustrated. The new member is found from the function shown in the equation below:

$$X_{\text{new}} = X_{r1} + F \cdot (X_{r2} - X_{r3}) \quad (5.15)$$

Where X_{r1} , X_{r2} and X_{r3} are randomly selected members of the original generation and F is a mutation factor. After generating a new candidate population from the current population a selection of the best members are made to create the final new population. The population is then iterated through generations until a stop criteria is met and the best solution of the final generation is selected as the solution. The procedure can be stated by four steps listed below:

Step 1 - Initialisation:

A population of NP designs is generated as shown below by generating a random integer for each design variable, x_j , where N is the horizon length:

$$X_i = [x_j \quad x_{j+1} \quad \cdots \quad x_N] \quad \forall \quad i = 1, 2, \dots, NP \quad (5.16)$$

Step 2 - Mutation:

NP number of trial designs are generated from three randomly selected designs from the current population, as shown below:

$$X_{\text{new}} = X_{r1} + F(X_{r2} - X_{r3}) \quad (5.17)$$

Where F is a mutation coefficient.

Step 3 - Crossover:

Individual elements of the new solution may be taken directly from the previous as:

$$\text{if } r_{i,j} > CR, \quad X_{\text{new},i,j} = X_{i,j} \quad \forall i = 1, 2, \dots, NP \quad j = 1, 2, \dots, N \quad (5.18)$$

Where $r_{i,j}$ is a random number between 0 and 1 and CR is a crossover coefficient.

Step 4 - Selection:

Designs are chosen for the new population by comparing the trial generation with the current generation as shown below.

$$\text{if } f(X_i) > f(X_{\text{new},i}), \quad X_i = X_{\text{new},i} \quad \forall i = 1, 2, \dots, NP \quad (5.19)$$

Step 2-4 are then repeated until the convergence criteria is met and the algorithm terminates and the best design is then chosen as the final solution. Typically the stop criteria is based on the variance of the population. The different steps may all influence convergence time and the solution and each step may be changed to fit the problem.

5.8 Differential Evolution Modification

To reduce the computational time of the DE some modifications are done. The modification is done in the mutation step of the algorithm. Five different mutation methods were tried but one including the current best solution of the population performed best compared on computational time. This modification of the differential evolution algorithm is developed in [27], and differs from the original in the mutation step, which is carried out as shown below:

$$X_{\text{new}} = X_{r1} + F(X_{\text{best}} - X_{r1}) + F(X_{r2} - X_{r3}) \quad (5.20)$$

Where X_{best} is the best solution of the current population, with respect to the cost function evaluation. All the remaining steps are similar to the original algorithm. To

see the effect of this modification a simulation comparing the original and the modified algorithm is done. As for the benchmark the algorithms are compared on how often the optimal solution is found and the computational time which is shown in Table 5.3. The comparison is performed for the same scenario as the benchmark scenarios as elaborated in Section 5.5.2. The comparison is only shown for the loss scenario, including static shifting loss, shown in Equation (5.12) but the same trends were seen for the other loss scenarios.

<i>Algorithm</i>	<i># Best found</i>	<i># 2nd best found</i>	<i>Average Time</i>	<i>Max Time</i>
Branch & Bound				
DE_{original}	999	0	0.252s	0.367s
DE_{modified}	998	0	0.166s	0.238s

Table 5.3: Comparison of the original DE and the modified DE algorithm.

As shown the modified DE algorithm is significantly faster compared to the original. For the given example the average time to find the optimum is decreased with approximately 34%. The faster convergence is obtained without compromising with the consistency, as the optimum is found 99.8% of the time. Based on this the modified DE is chosen as the optimisation algorithm.

To further decrease the computational time a "warm start" may be used in the initialisation of the population. The warm start procedure is based on starting the optimisation algorithm in a point close to the solution from the previous sample instant. The warm start may cause the optimisation algorithm to converge faster under the assumption that the new solution is in the neighbourhood of the previous solution. The initial population is slightly perturbed from the previous solution as shown below:

$$X_i = X_{\text{PreviousSolution}} + X_{\text{random}} \quad \forall \quad i = 1, 2, \dots, NP \quad (5.21)$$

Where $X_{\text{PreviousSolution}}$ is the previous solution and X_{random} is a vector with random generated integers from -1 to 1. To analyse the effect of the warm start the model is used to simulate the system for sea state 1 with and without the warm start. The sample time is chosen as 0.2s with a time horizon of 2s, and the objective function for the optimisation algorithm is only including static shifting loss. A histogram of the computational time of the optimisation algorithm are shown in Figure 5.12 for both warm and normal start.

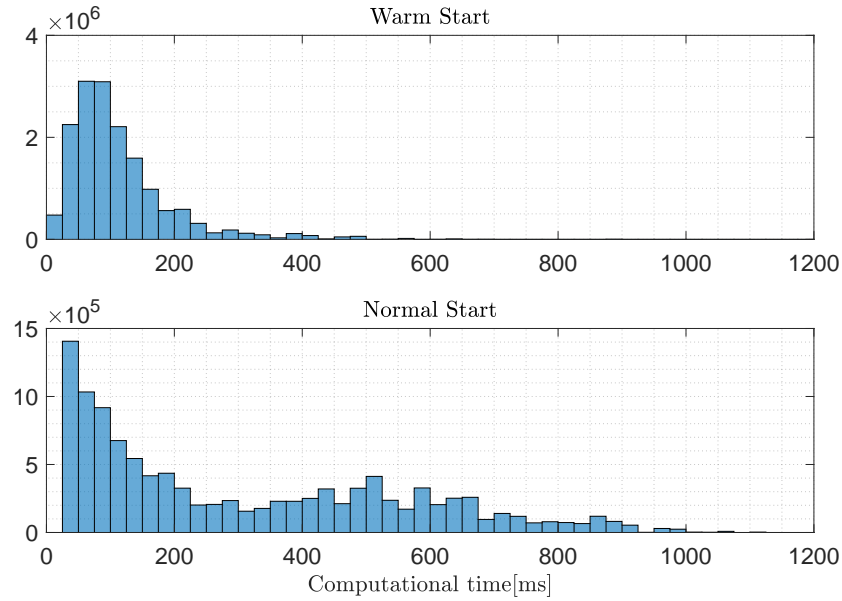


Figure 5.12: Histogram of the computational time with and without warm start with groups of 2ms.

As it may be seen the warm start decreases the computational time for the majority of the iterations. A significant reduction in maximum time for the DE to converge is seen. For the example given in Figure 5.12 an average convergence time of 0.304s for the "normal start" obtained, and 0.112s for the "warm start". The warm start procedure is also seen to be more consistent in convergence time. The average power harvested for the two simulations were found approximately equal. The simulations may indicate that the warm start does not compromise with average harvested power while being significantly faster, why the warm start is utilised.

6 | MPC Simulation Evaluation

The performance of the MPC in Chapter 5 will be evaluated subject to different time horizons and cost functions. Initially a performance evaluation of the MPC based on the simulation model is desired. This is done to verify the preliminary results obtained in Chapter 4 based on the continuous MPC. For the simulations a MPC sample time of 0.2s is chosen to compare the simulations with measurements as 0.2s was found realisable for implementation. Using the model for simulation allows for investigation of increased horizon length, as limitations regarding the computational time is not a concern in the simulation model. The MPC performance is based on the point absorber model. A diagram showing the evaluation procedure is shown in the figure below. To verify the

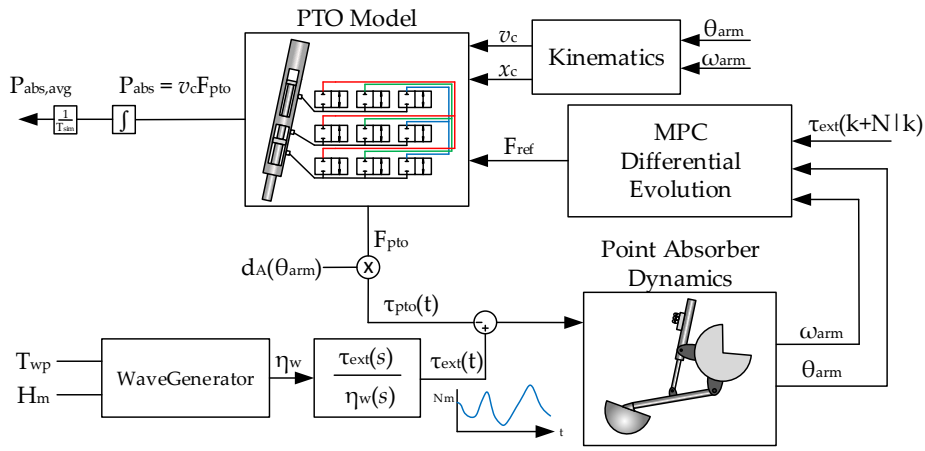


Figure 6.1: Diagram showing the MPC evaluation procedure.

developed MPC schemes, the model is simulated for test wave 3 given in Table 6.1 for the four different cost functions given in Section 5.4. The MPC is simulated with a horizon length of 10 and with the assumption of ideal wave forecasting. The simulation results are shown in Figure 6.2, where the piston velocity and PTO force for the four different cost functions are shown. From the figure it is evident that introducing force shifting losses to the MPC cost functions significantly reduces the amount of force shifts. The MPC with losses included in the cost function is seen to only utilise 4-6 force steps when going from the minimum PTO force to maximum force. This may indicate that a system design with fewer force levels may be utilised without compromising with the performance. However, this is not addressed in this thesis. A slight difference between the PTO force trajectories are seen for the three MPC formulation with losses included. As elaborated in the following sections, the cost functions with more losses performs better with respect to harvested energy, with the drawback of higher computational demand.

In the following section the MPC performance is evaluated based on average harvested power in different sea states. The harvested energy for a given simulation is calculated as:

$$E_{har} = E_{abs} - E_{loss,\beta} - E_{loss,t} = \int_{t_0}^{T_{sim}} v_c(t) F_{PTO}(t) dt - \sum_{i=1}^{n_{shifts}} E_{loss,\beta,i} - \int_{t_0}^{T_{sim}} P_{loss,t}(t) dt \quad (6.1)$$

The average harvested power is calculated as $P_{har,avg} = \frac{E_{har}}{T_{sim}}$. T_{sim} is the time length of

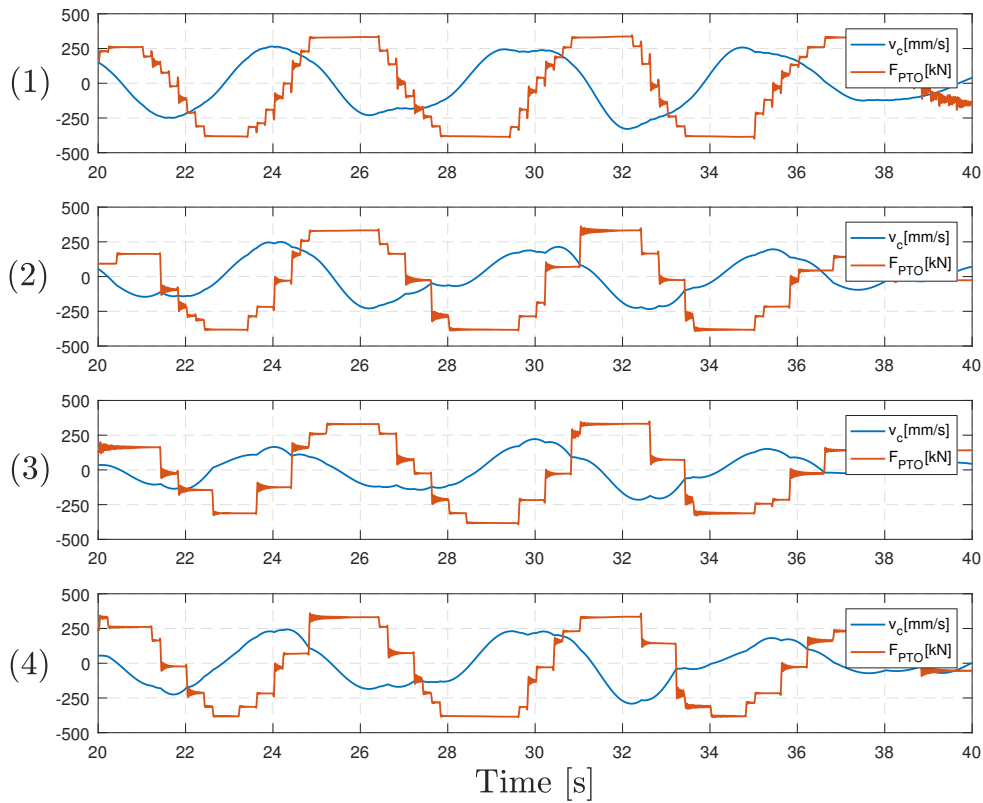


Figure 6.2: Visual example of PTO force trajectories for: (1) No loss Eq. (5.6), (2) Lookup Eq. (5.8), (3) Lookup and throttle Eq. (5.9), (4) Complete loss Eq. (5.10). $T_s = 0.2s$, $N = 10$.

the simulation, $E_{\text{loss},\beta}$ is the shifting loss and $P_{\text{loss},t}$ is the throttling loss. The shifting losses and the throttling losses are calculated according to Equation (3.45) and (3.47) respectively.

6.1 Model Complexity and Time Horizon

To investigate the harvested energy subject to different cost functions, simulations with the four different cost functions described in Chapter 5 are performed for five different sea states. The parameters for the sea states used in the simulations are shown in Table 6.1.

Wave	1	2	3	4	5
H_m	0.75m	1m	1.25m	1.75m	2.25m
T_{wp}	3.5s	4.5s	4.5s	5.5s	5.5s

Table 6.1: Test waves parameters.

This analysis should indicate how the average harvested power is affected by the model complexity and the time horizon of the MPC scheme. In Figure 6.3 the average harvested

power is shown for simulations of approximately 100 wave periods for the different test waves given in Table 6.1 and the four different cost functions described in Chapter 5. For the simulations shown in Figure 6.3 a constant time horizon of 4s is chosen such only the influence of the MPC cost function is obtained.

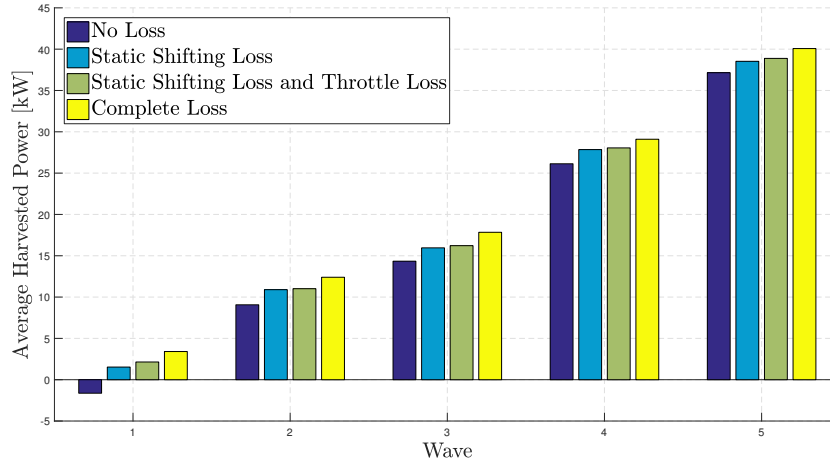


Figure 6.3: Average harvested power for different cost functions and different ocean waves with $N = 20$ and $T_s = 0.2s$.

As evident from the figure the average harvested power increases with the complexity of the MPC cost function. Imposing losses in the PTO transmission according to Equation (3.45) and (3.47) it is evident that including these in the MPC formulation results in higher energy output. This shows that if the actual losses in the PTO is modelled appropriately, the MPC scheme allows to include these for better performance. The cost function including shifting loss computed from estimated cylinder states further increased the average harvested power as cheaper force shifts may be taken at cylinder strokes with lower chamber volumes.

The MPC is evaluated for different values of N to obtain the horizon length at which the average harvested power saturates. In Figure 6.4 the average harvested power is shown for the cost function only including static loss by a lookup table. As evident from the simulations the average harvested power does not increase beyond a time horizon of 4 seconds. The same trend were also seen for the continuous MPC in Chapter 4. This shows that it is unnecessary to increase the time horizon beyond 4 seconds as this only complicates the optimisation problem in terms of additional design variables.

6.2 Evaluation of MPC Computational Time

As the computational time may be a main issue for discrete MPC it is analysed how the computational time is affected by the complexity of the cost function and the time horizon. This is shown in Figure 6.5 where the average computational time for different cost functions and increasing time horizon is shown. All simulations are done for test wave number four.

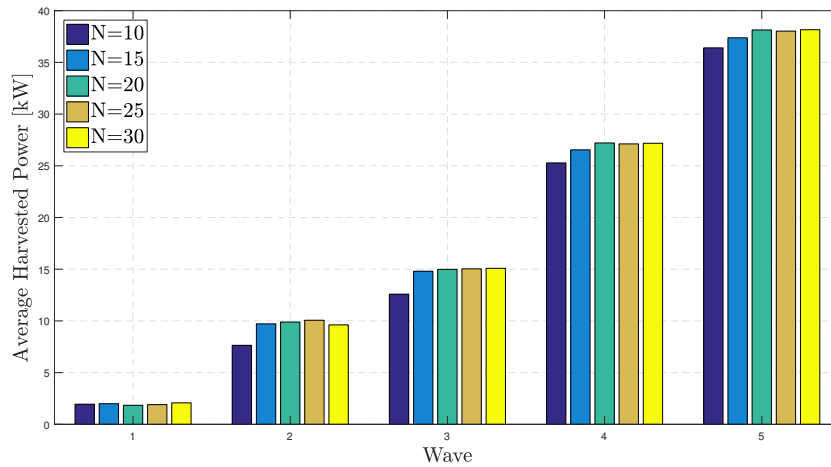


Figure 6.4: Average harvested power for different ocean waves and different time horizon with $T_s = 0.2s$.

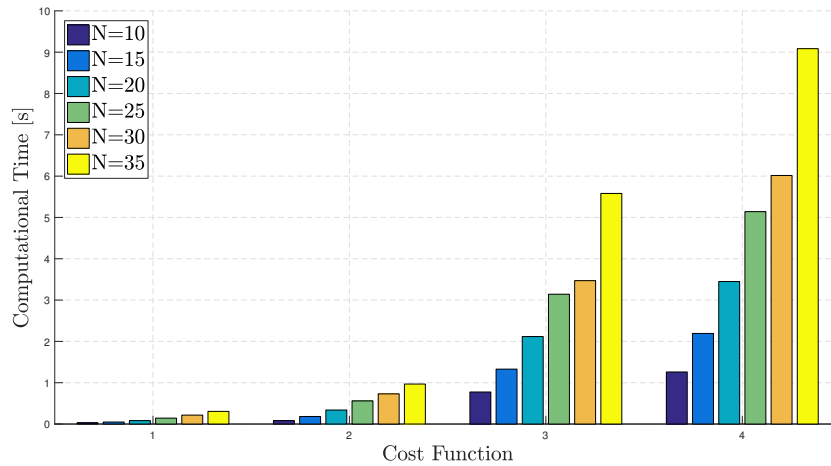


Figure 6.5: Average computational time of MPC for different cost functions and different time horizon. (1) No loss Eq. (5.6), (2) Lookup Eq. (5.8), (3) Lookup and throttle Eq. (5.9), (4) Complete loss Eq. (5.10).

The computational time increases significantly as more losses are included in the cost function. A reduction in computation time compared to the original DE algorithm is obtained. Table 5.2 shows a convergence time of approximately 1400s with a horizon length of 25 for the original DE algorithm. The difference may be due to modifications of the algorithm, and the utilised warm start procedure. The results indicates that losses estimated from computed states as stated in Equation (5.10) may be impractical to implement due to the computational demand. Further high horizon lengths may be difficult to implement if losses are to be included. The computational times shown is for a MATLAB function and not a final implemented algorithm. The computational time should therefore only be seen relatively to each other.

6.3 Part Conclusion

It is shown that if losses are modelled appropriately these may be included in the MPC formulation to obtain increased performance. Increasing the amount of losses in the cost function also increases the computational time of the MPC, potentially making it impractical for real time implementation. Further it may be seen that the time horizon of the MPC influences the amount of harvested power, however the average harvested power does not increase beyond a time horizon of approximately 4 seconds. For real time implementation a compromise between model complexity, time horizon and computational time has to be made.

7 | Experimental Evaluation

The implementation of the developed MPC scheme is performed on the test bench described in Section 1.1.3. The control of the test bench, data logging etc. is performed on a LabVIEW Real-Time target (RT target) as shown in Figure 7.1. The RT target communicates with a host PC from which a HMI displays relevant states of the test bench in real time. In Appendix B the implementation of the MPC in LabVIEW is elaborated.

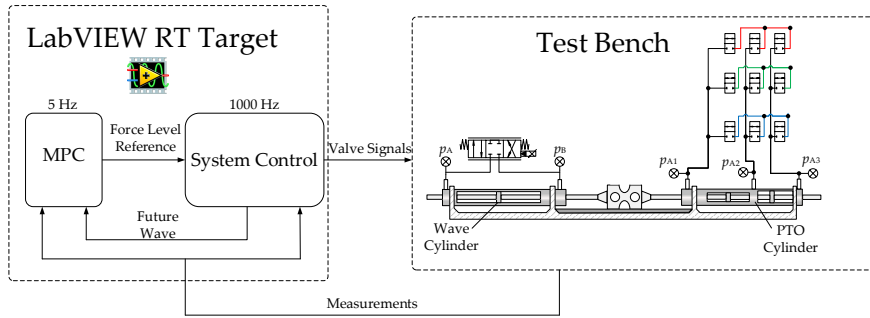


Figure 7.1: Overview of the control of the test bench.

The RT target executes the control of the PTO and wave system with 1000Hz. The frequency of the MPC is chosen dependent of which cost function that is used and will be addressed later in this chapter. The MPC sets up the optimisation problem after each sample instance of the MPC, based on the point absorber model and the future excitation torque and executes the DE algorithm to generate the force level reference for the PTO system.

The MPC is formulated such the solution for the PTO force is assumed to be applied at time $k = t$, thus not considering the delay in the applied PTO force reference due to computational time. To visualise the delay of $F_{pto,ref}$ a timeline of the MPC execution is shown in Figure 7.2.

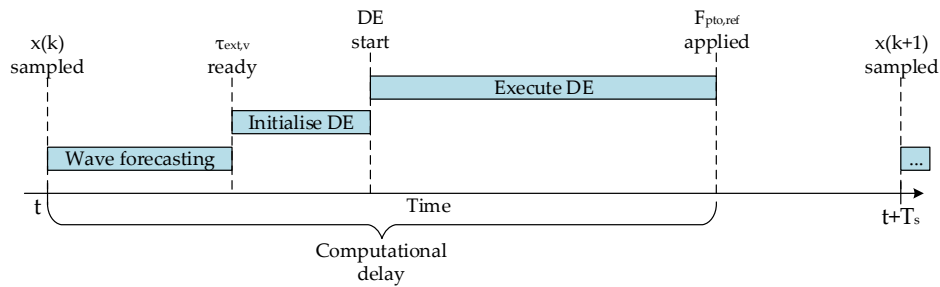


Figure 7.2: Timeline of the MPC execution as implemented.

At time t the cylinder position and velocity is sampled and converted into equivalent point absorber coordinates. The wave forecasting described in Section 4.2.5 is executed to generate the future excitation torque, $\tau_{ext,v}$, used in the MPC cost function. If wave forecasting is disabled $\tau_{ext,v}$ is taken from the known excitation torque. The optimisation

problem is then initialised by generating \mathbf{f} , as shown in Equation (4.15), of the cost function. After formulating the optimisation problem the DE algorithm is executed. This implies that the force reference is delayed by the computational time as shown in Figure 7.2. The execution time of the wave forecasting and the formulation of the optimisation problem is seen to be insignificant compared to the computational time of the DE algorithm. Due to the stochastic behaviour of the DE algorithm the computational time may vary and may even exceed the sample time T_s . If the computational time exceeds the sample time, T_s , the next MPC execution is skipped, why it is desired to avoid computational times above the sample time. To account for this a restriction of allowed generations of the DE algorithm is utilised to ensure that the DE algorithm finishes before the next sample instant. . This may affect the solution of the optimisation problem as the DE algorithm is not allowed to converge for all instants.

Simulation including a fixed delay in the applied PTO force reference has shown that the influence with respect the harvested power is insignificant. The computational delay is thus assumed neglectable for the tests why the implementation of the MPC scheme is considered appropriate. However some effort has been put into formulating the MPC to compute the next force reference instead of the current, such the delays of the DE execution may be handled. The alternative approach of executing the MPC scheme addressing the computational delay is considered in Appendix B.1.1 but is not evaluated experimentally.

The MPC code is partly implemented as LabVIEW code and as custom defined shared libraries which allows to execute the developed DE algorithm on the RT targets. The DE code implementation is elaborated in the following section.

7.1 DE Code Implementation

The DE algorithm is implemented by creating a shared library which may be executed on the RT target. This is done by translating the MATLAB code into C code by the MATLAB application "MATLAB Coder". The C code is used to generate a shared library with the software package "LabWindows CVI" from National Instruments. "LabWindows CVI" is used to ensure that the generated shared library is compatible with the RT target.

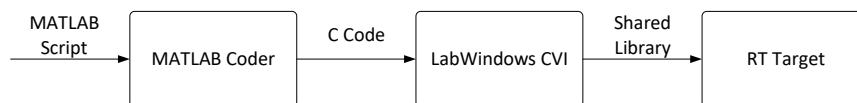


Figure 7.3: Overview of the generation of shared library.

For the cost function with static shifting loss, given in Equation (5.8), approximated by look up table and with a horizon length of $N = 10$, the DE algorithm was able to converge with an average of approximately 50ms, why it is chosen to run the MPC with this cost function with a sample time of 0.2s.

For the cost function with throttling losses included, given in Equation (5.9), and with a horizon length of $N = 10$, the DE algorithm was able to converge with an average of approximately 150ms, why it is chosen to run the MPC with this cost function with a sample time of 0.3s.

It was not able to obtain convergence time within the requirement of 0.35s for the MPC

with the cost function computing the complete losses given in Equation (5.10). For this reason the cost function is omitted in the experimental evaluation of the MPC. The MATLAB script for the implemented DE algorithm is given in Appendix B.2. In the following the implemented MPC will be evaluated on the test bench.

7.2 Evaluation

The developed MPC is to be evaluated and compared with the reactive control scheme. The control parameters for the reactive control is optimised for each sea state with respect to maximum harvested power. The average absorbed power and average harvested power of a given test is calculated based on flow and pressure measurements in the PTO valve manifold according to the method elaborated in Section 3.5.2.

Initially the consistency of the test results is analysed to indicate how the harvested power is varying from each test.

7.2.1 Measurement Consistency

To analyse the consistency of the test results, ten measurements are conducted under the same conditions. The tests are conducted for a MPC including static shifting loss and throttle loss in the cost function, and with a sample time of 0.3 and a time horizon 3s. Test wave 3 from Table 6.1 is utilised for the tests. Each test is performed for approximately 500s. The average harvested power for each test is shown in Figure 7.4 along with the average for the ten tests.

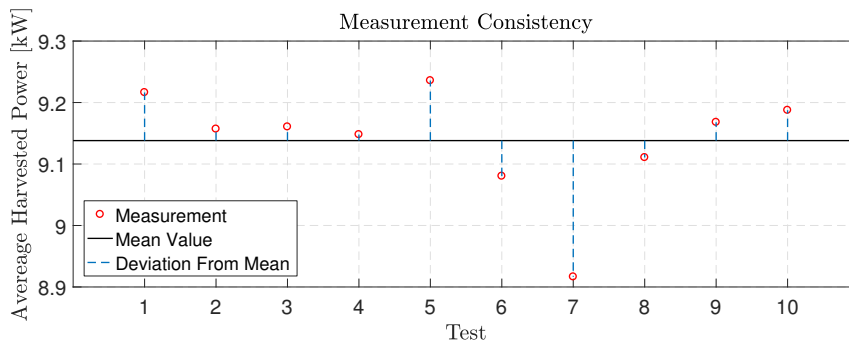


Figure 7.4: Five measurements conducted under the same conditions.

The maximum deviation from the average value is 0.22kW, however the 7th test is seen to deviate significantly more than the others. Based on the result shown in Figure 7.4 it is concluded that one test for each wave is sufficient for evaluation.

First the MPC is evaluated with loss and no loss in the cost function. The performance is evaluated with respect to harvested energy and efficiency.

7.2.2 Comparison of Loss and no Loss Formulation

To investigate the effect of including losses in the cost function a test comparing the MPC with and without losses is performed. This is done to indicate whether losses should be included in the MPC cost function. The cost functions given in Equation (5.6) and (5.8)

are used. The comparison is performed for the same test wave of approximately 500 seconds. The measured average absorbed power and harvested power for the two tests are shown in Table 7.1.

MPC type	$P_{\text{abs,avg}}[\text{kW}]$	$P_{\text{har,avg}}[\text{kW}]$	η
MPC without losses in cost	8.73	1.20	0.14
MPC with losses in cost	6.16	4.44	0.72

Table 7.1: Comparison of the MPC performance with and without losses in the cost function.

As evident from the table, a higher average harvested power is obtained by including the static shifting losses in the cost function. The absorbed power is higher for MPC without losses included but the low efficiency results in less harvested power. It may be concluded that losses should be included in the MPC formulation to increase the average harvested power. The low efficiency of the MPC without losses included is caused by more frequently and energy expensive force shifts. In Figure 7.5 and 7.6 a comparison of the MPC with loss and without loss is shown. As evident from the MPC including static shifting losses in the cost function, the force is always shifted with use of the medium pressure line. The MPC without shifting losses is seen to not always make use of the medium pressure line when shifting chamber pressure, and are often shifting multiple chambers simultaneously.

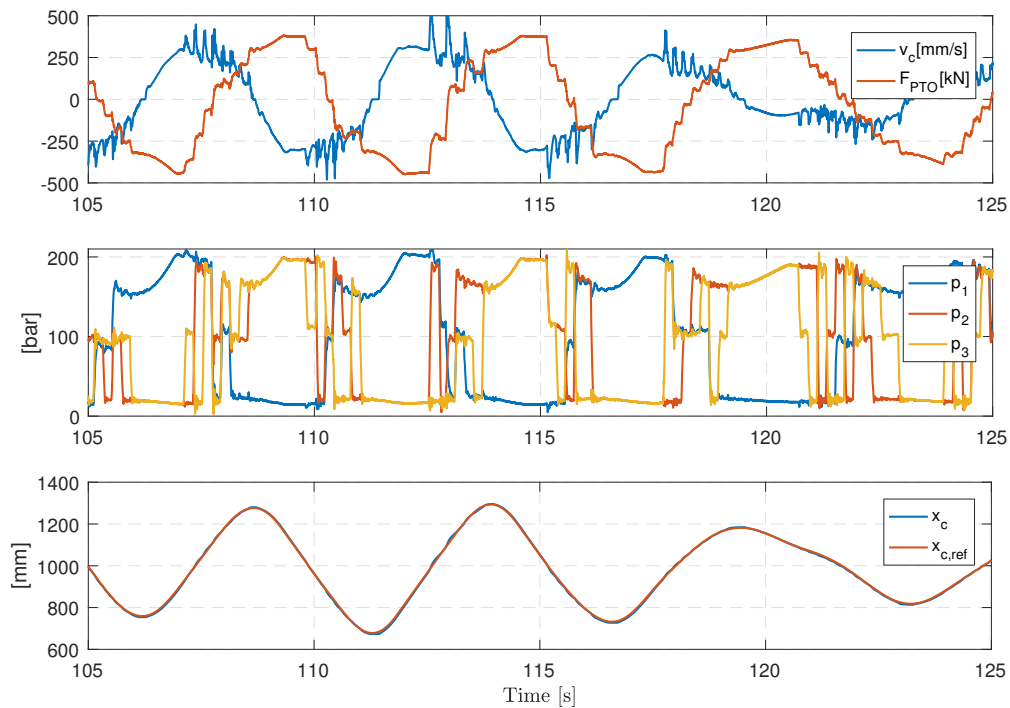


Figure 7.5: MPC with sample time of 0.2s and horizon length of $N=10$, with no losses in cost and ideal wave forecasting.

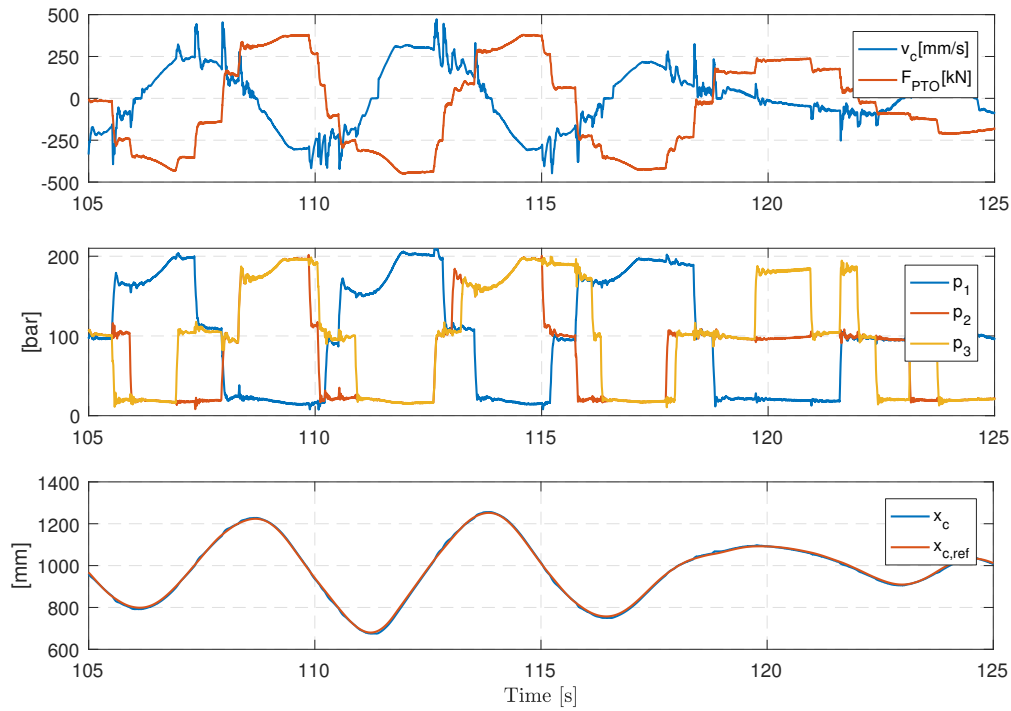


Figure 7.6: MPC with sample time of 0.2s and horizon length of $N=10$, with static shifting losses in cost and ideal wave forecasting.

It is seen that the wave cylinder control yields good tracking performance, why the PTO cylinder is subjected to motion equal to the Wave Star point absorber. To evaluate the execution of the MPC the computational time is logged. A histogram of the execution time of the two tests are shown in the Figure 7.7.

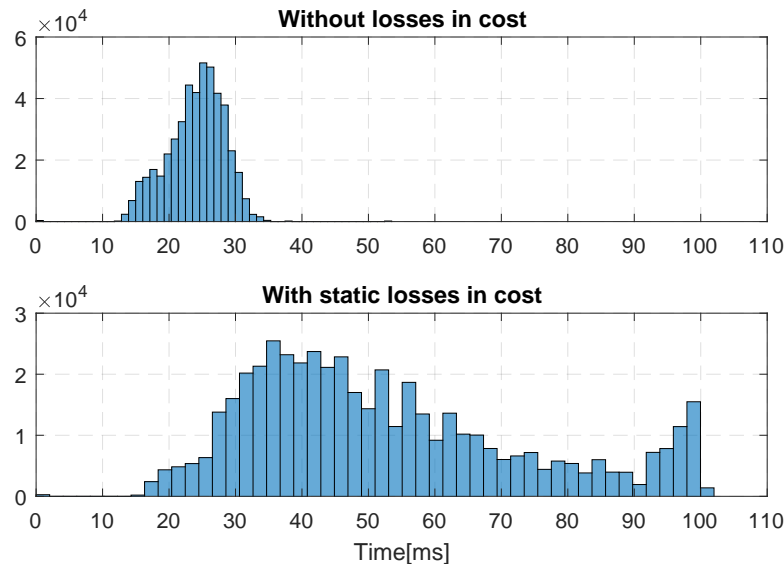


Figure 7.7: Computation time of MPC for the cases shown in Figure 7.5 and 7.6 respectively.

From Figure 7.7 it is evident that the MPC without losses is significantly faster than the MPC with losses. This imposes that the computational delay is reduced compared to the

MPC with losses. The tests have shown that the fast execution of the MPC without losses does not compensate for the lower amount of harvested power, caused by not penalising energy expensive force shifts in the cost function. As a consequence it is chosen only to evaluate MPC schemes including loss in the following.

7.2.3 Comparison of MPC and Reactive Control

Both reactive control and MPC will be evaluated subjected to several waves series, to investigate the performance for different test waves. Five different waves are used in the performance evaluation, with the wave parameters given in Table 7.2.

<i>Wave</i>	1	2	3	4	5
$H_m[m]$	0.75	1	1.25	1.75	2.25
$T_{wp}[s]$	3.5	4.5	4.5	5.5	5.5
$k_{pto} \left[\frac{N}{m} \right]$	$-8.8 \cdot 10^5$	$-8.8 \cdot 10^5$	$-1.1 \cdot 10^6$	$-1.1 \cdot 10^6$	$-1.1 \cdot 10^6$
$B_{pto} \left[\frac{Ns}{m} \right]$	$5 \cdot 10^5$	$5 \cdot 10^5$	$8.8 \cdot 10^5$	$1.4 \cdot 10^6$	$1.6 \cdot 10^6$

Table 7.2: Test waves parameters and reactive control parameters used for each test wave.

The reactive control parameters used in the evaluation are optimised for each test wave with respect to average harvested power. The reactive controller is used along with the force shift algorithm explained in Section 1.2.

For the following comparison ideal wave forecasting is assumed for the MPC. To give a visual comparison of the reactive controller and the MPC, the cylinder velocities and PTO force along with instantaneous absorbed power for test wave 4 are shown in Figure 7.8. Here a time horizon of 3s and a sample period of 0.3s is chosen for the MPC only including shifting loss.

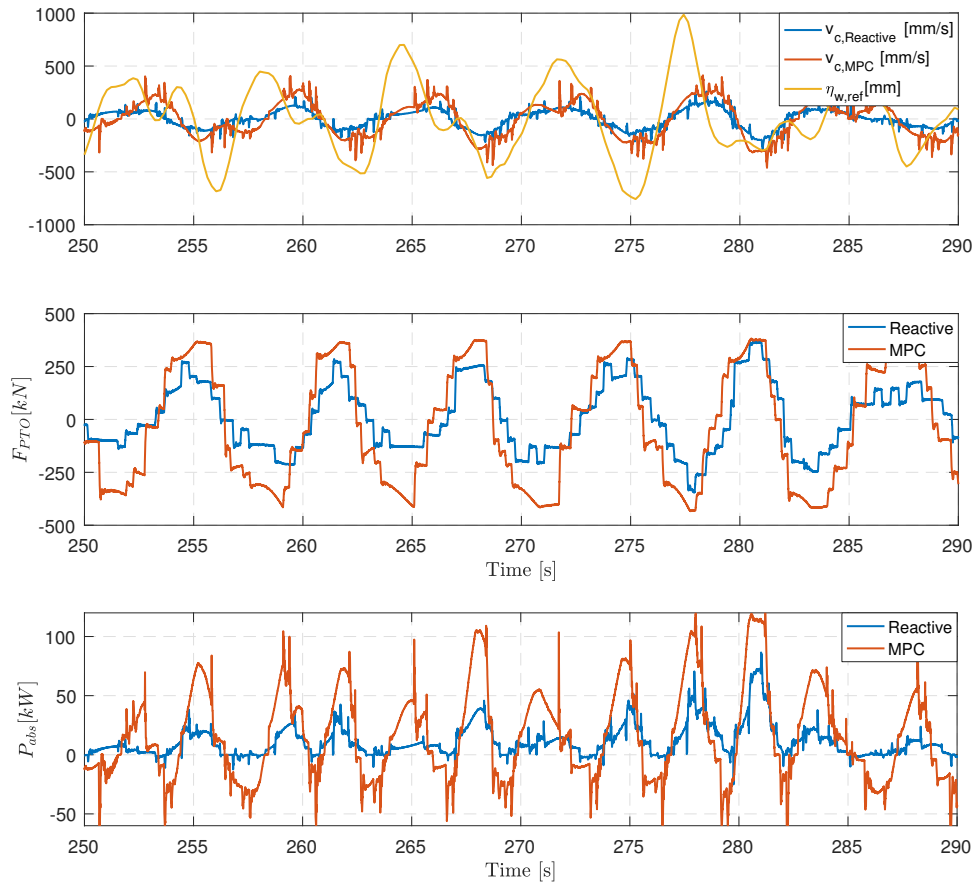


Figure 7.8: Comparison of reactive controller optimised to test wave 4, and MPC with $T_s = 0.3s$ and $N = 10$.

From the measurements it is evident that the MPC imposes more reactive power in the PTO transmission. In addition it may be seen that the instantaneous absorbed peak power is significantly higher for the MPC. As a consequence the MPC generally imposes higher cylinder piston velocities for the same test wave. The PTO system of the Wave Star WEC is designed to utilize intermediate energy storage by use of hydraulic accumulators between the primary and secondary stage of the PTO system. Thus, the high fluctuating power absorption of the MPC is not of concern, as the intermediate energy storage allows the hydraulic motor to operate at optimal operating conditions[22]. The higher amount of reactive power and cylinder piston velocity with the MPC may suggest that more power is dissipated in the PTO system. The possible fatigue associated with this is not addressed in this thesis, however just noted as an observation.

For the evaluation of the MPC, different parameters and cost functions of the MPC is tested. A MPC with horizon length of $N = 5$ is included to emphasise the significance of increasing N . The following configurations of the MPC are shown:

- MPC1: $T_s = 0.2s$, $N = 5$, Static shifting loss: Equation (5.8).
- MPC2: $T_s = 0.2s$, $N = 10$, Static shifting loss: Equation (5.8).

- MPC3: $T_s = 0.3s$, $N = 10$, Static shifting loss: Equation (5.8).
- MPC4: $T_s = 0.3s$, $N = 10$, Static shifting loss and throttle loss: Equation (5.9).

For the different test waves and control schemes the absorbed power, harvested power and efficiency is shown in Figure 7.9, 7.10 and 7.11 respectively.

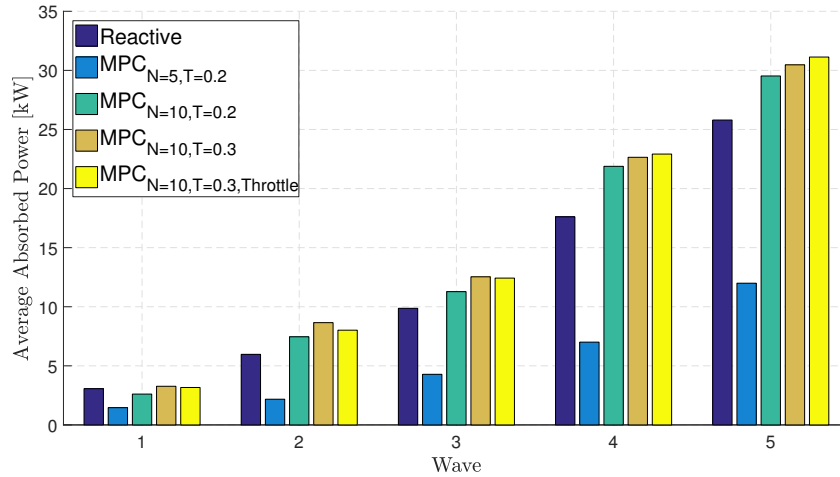


Figure 7.9: Average absorbed power for different control schemes and wave series.

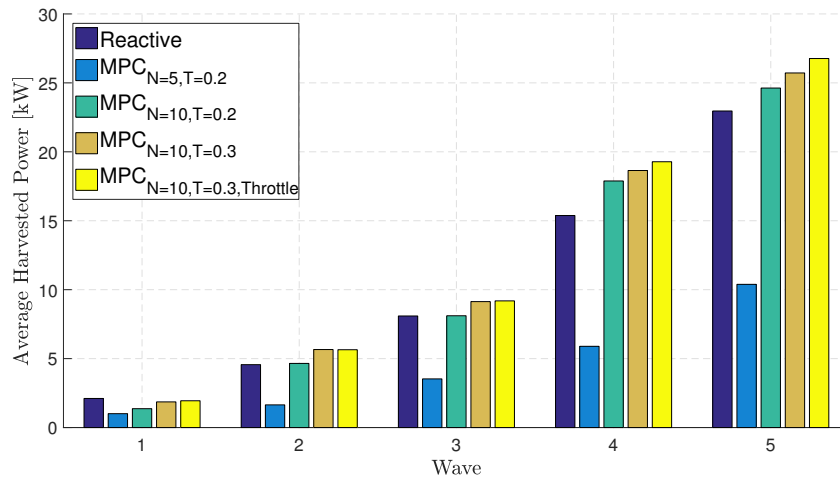


Figure 7.10: Average harvested power for different control schemes and wave series.

As evident the MPC with a sample time of 0.2s and a time horizon of 1s harvests significantly less power compared to the remaining control schemes. This indicates that MPC should have a certain time horizon to perform sufficient compared to the reactive control scheme. Further it may be seen that MPC with a sample time of 0.3s and a time horizon of 3s performs slightly better compared to MPC with a sample time of 0.2s and a time horizon of 2s. From this it may be seen that the additional second in the time horizon is more significant than the increased sample time. It is expected that the influence of increasing the time horizon to 4s would increase the average harvested power. Thus if more computational power is available, simulations shows that the performance of the MPC may be increased. Figure 7.10 shows that the MPC scheme including throttling

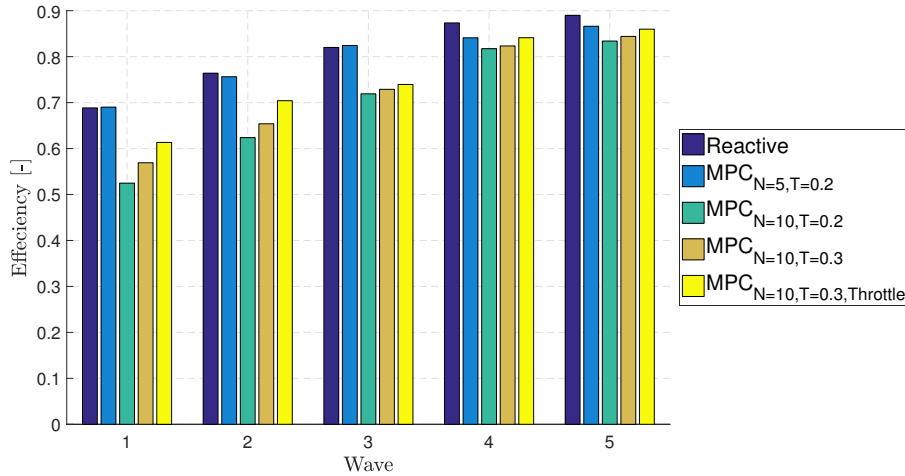


Figure 7.11: Efficiency for different control schemes and wave series.

losses, with a sample time of 0.3s and a horizon length of 10 was able of increasing the average harvested power of 14% to 25% for 4 out 5 tested waves, compared to the reactive control scheme. The results indicate that MPC is a suitable control topology for a discrete displacement hydraulic power take-off system. In Appendix C the exact values of the measurements shown in Figure 7.9, 7.10 and 7.11 are given.

In general the MPC schemes performs better than reactive control, with respect to harvested power, when having a sufficient time horizon. For the smallest test wave the reactive control scheme performs better with respect to harvested power. Without definite conclusions one potential reason for the poor performance of the MPC for the small wave series is discussed. The explanation comes from practical observations during testing. The MPC was seen to “get stuck” in a force level, and due to a relative short time horizon the energy cost of shifting to a new force level may be too high compared to the harvested power over the time horizon. For this reason the MPC was seen to give the same force reference for 10-15 seconds during testing. An example of this is shown in the figure below. Here the MPC sample time is 0.2s, and the horizon length is 10 for test wave 1.

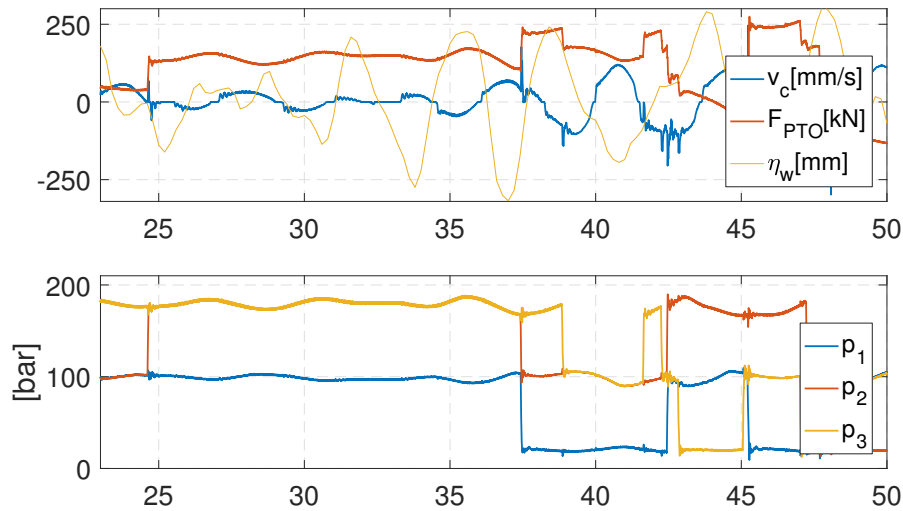


Figure 7.12: MPC with $T_s = 0.2s$, $N = 10$ for test wave 1. An example of MPC getting "stuck" in a force level.

To overcome this problem it is suggested that the pressure levels in the high and medium line is lowered in small sea states to allow less expensive force shifts to be made.

In general the reactive control scheme has higher efficiency. Even though the harvested power is higher for the MPC, the lower efficiency may indicate higher fatigue in the PTO transmission as more energy is dissipated in the process. It has further been shown that discrete MPC may be implemented for a discrete displacement fluid power PTO system and increase the average harvested power for most test waves compared to the reactive control scheme.

7.3 MPC with Wave Forecasting

To investigate how the wave estimation described in Section 4.2.5 affects the harvested power, tests are conducted with and without wave excitation torque forecasting. The order of the AR model used for wave forecasting is chosen to 40, thus the wave forecasting is depended on the 40 previous estimates of the wave excitation torque. As no samples are available at the beginning, the first 40 MPC iterations are performed with ideal wave forecasting for the comparison. Both strategies are tested with the MPC including static loss and throttling loss in the cost function and with a sample time of 0.3s and a horizon length of $N = 10$. The tests are conducted for the five test waves shown in Table 6.1. In Figure 7.13 the average harvested power for each test wave with and without wave estimation is shown.

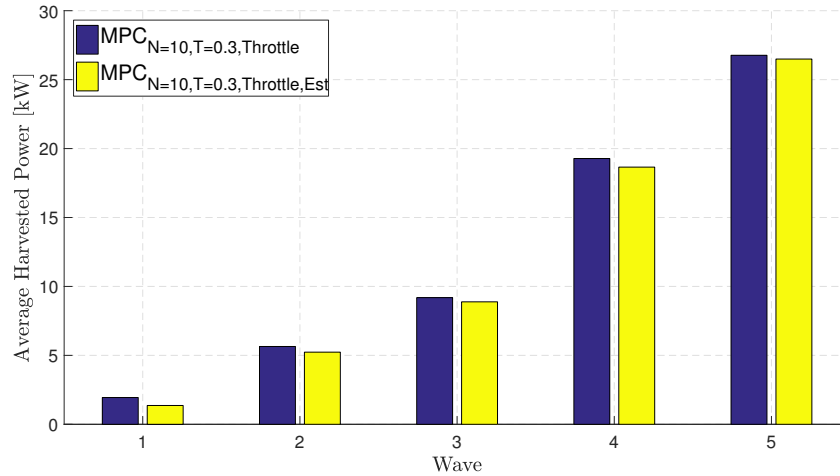


Figure 7.13: Average harvested power with and without wave estimation for MPC with static shifting loss and throttling losses, $T_s=0.3s$ and $N=10$.

As shown in the figure the MPC using the forecasted excitation torque performs slightly worse than the MPC using the ideal future torque. The reduction is between 0.27kW and 0.62kW in average harvested power for the five test waves. For test wave 2-5 the MPC using forecasting has a higher average harvested power compared to the reactive control scheme.

The results may indicate that the future torque applied by the wave can be estimated sufficiently without compromising significantly on the performance. For the tests, ideal wave excitation torque estimation is assumed, why the excitation torque used in the forecasting is directly fetched from the input torque given to the point absorber model computing the position and velocity reference for the wave cylinder piston.

7.4 Part Conclusion

In this chapter it has been shown that MPC for a discrete fluid power system may be implemented in real time and increase the average harvested power compared to a reactive control scheme. Further it has been shown that losses should be included in the MPC to increase the amount of harvested power for the majority of the tested waves. The reactive control was found to yield higher average harvested power for the smallest test wave. It may complicate the MPC to include complex loss calculations and it has not been possible to include more than static shifting loss and throttling loss for the implementation. In general more reactive power is imposed in the PTO system compared to the reactive control scheme. This resulted in higher average harvested power, however with lower PTO transmission efficiency. This may result in higher fatigue of the PTO system but this is not addressed in this thesis. Forecasting of the excitation torque is possible and have been implemented assuming ideal estimation of the excitation torque. Using the proposed forecasting scheme resulted in a reduction between 0.27kW and 0.62kW in average harvested power.

8 | Conclusion

In this thesis, a model predictive control scheme has been developed for a discrete displacement hydraulic power take-off system. A case study of the Wave Star wave energy converter was taken. The main objective for the thesis has been to investigate if a model predictive control scheme may be formulated and implemented in real time for a discrete displacement hydraulic power take-off system. A second objective has been to investigate if a model predictive control scheme may increase the performance of the power take-off system compared to the previous used reactive control scheme.

A MPC has been formulated based on a linear point absorber model of the Wave Star WEC. The optimisation of the MPC was formulated as an energy maximisation problem over a finite time horizon including losses of the PTO system in the cost function. Two different optimisation algorithms were tested and a modified differential evolution algorithm was chosen as the solver over a Branch and Bound inspired algorithm.

Four cost functions including different combinations of force shifting- and flow throttling losses were formulated. Simulations showed that the energy harvested from the waves may be improved by increasing the amount of losses included in the MPC cost function. Increasing the time horizon of the MPC was also seen to increase the harvested energy, however no significant improvement beyond a time horizon of 4 seconds was seen. The increase of losses and horizon length comes with an increased computational demand, why a compromise should be chosen to allow real time implementation.

The developed MPC scheme was implemented on a LabVIEW RT target and tested on the Wave Star PTO test bench. Three out of the four cost functions evaluated in the simulations were found possible to execute within the required maximum time limit of 0.35s. A cost function maximising the absorbed power over the time horizon including no losses were found to yield bad performance, why it was concluded that losses must be included in the cost function to obtain acceptable efficiency of the PTO transmission. A cost function with the energy loss associated with force shifting approximated by a lookup table evaluated for a fixed position, and a cost function including flow throttling losses as well were evaluated and compared to the reactive control scheme. A cost function with position depending force shifting losses was found too computational demanding why it was not evaluated experimentally.

The MPC with only shifting losses were evaluated with a sample time of 0.2s, and the MPC including throttling losses as well were evaluated with a sample time of 0.3s. The MPC was tested for five different test waves, subject to different time horizons. It was found that a time horizon of 1 second yielded significantly lower harvested power compared to the reactive control scheme. MPC schemes with a time horizon of 3s and a sample time of 0.3s had higher average harvested power compared to the MPC scheme with a sample time 0.2s and a time horizon of 2s. The tested MPC with highest average harvested power was a MPC scheme with shifting losses and throttling losses included in the cost function, with a sample time of 0.3s and a horizon length of 10. This MPC was able of increasing the average harvested power of 14% to 25% for 4 out 5 tested waves, compared to the reactive control scheme.

To address the required precision of wave forecasting, a simple wave forecasting scheme based on an autoregressive model was developed. The AR model was designed to compute

the equivalent wave excitation torque over the MPC time horizon. The used method showed that it was possible to forecast incoming waves with acceptable accuracy 2-3 seconds forward in time. Simulations showed that the obtained accuracy was sufficient to allow close to ideal performance. The forecasting scheme was evaluated experimentally, and it was shown that the MPC with non-ideal future wave knowledge could outperform the reactive control scheme. A reduction between 0.27kW and 0.62kW for the tested waves for the case with wave prediction was seen compared to the case with ideal wave forecasting.

In general, it is concluded that model predictive control is a suitable control topology for a discrete displacement hydraulic power take-off system. Based on experimental evaluation, a MPC scheme may increase the average harvested power for a wave energy converter utilizing a discrete PTO system compared to a reactive controller.

Bibliography

- [1] J. P. Kofoed, “Ressourceopgørelse for bølgekraft i danmark,,” 2009. Aalborg: Department of Civil Engineering, Aalborg University. (DCE Contract Reports; Nr. 59).
- [2] A. Pecher and J. P. Kofoed, *Handbook of Ocean Wave Energy*. Springer Open, 7th ed., 2017.
- [3] <http://www.emec.org.uk/about-us/media-centre/gallery/>, 2017. [Online; accessed 25-April-2017].
- [4] <http://www.oceanpowertechnologies.com/pb3/>, 2017. [Online; accessed 25-April-2017].
- [5] L. M. Morten M. Kramer and P. Frigaard, “Performance evaluation of the wavestar prototype,” 2011. The 9th European Wave and Tidal Energy Conference: EWTEC 2011. University of Southampton, 2011.
- [6] T. O. A. Rico H. Hansen and H. C. Pedersen, “Model based design of efficient power take-off systems for wave energy converters,,” 2011. The Twelfth Scandinavian International Conference on Fluid Power, May 18-20, 2011, Tampere, Finland.
- [7] A. H. Hansen and H. C. Pedersen, “Energy cost of avoiding pressure oscillations in a discrete fluid power force system,” 2015. Proceedings of The 2015 Bath/ASME Symposium on Fluid Power and Motion Control, 2015 Chicago.
- [8] R. H. Hansen, “Design and control of the powertake-off system for a wave energy converter with multiple absorbers,” 2013. Ph.D. dissertation, Department of Energy Technology, Aalborg University.
- [9] T. O. A. Rico H. Hansen and H. C. Pedersen, “Analysis of discrete pressure level systems for wave energy converters,” 2011. Fluid Power and Mechatronics(FPM), 2011 International Conference. 17-20 Aug.
- [10] M. T. S. Mohsen N. Soltani and M. Mirazei, “Model predictive control of buoy type wave energy converter,” 2014. The International Federation of Automatic Control Cape Town, South Africa. August 24-29, 2014.
- [11] T. K. A. Brekken, “On model predictive control for a point absorber wave energy converter,” 2011. 2011, IEEE Trondheim PowerTech Conference paper.
- [12] K. M. N. Palle Andersen, Tom S. Pedersen and E. Vidal, “Model predictive control of a wave energy converter,” 2015. 2015 IEEE Conference on Control Applications (CCA), Part of 2015 IEEE Multi-Conference on Systems and Control, September 21-23, 2015. Sydney, Australia.
- [13] A. Grancharova and T. A. Johansen, *Nonlinear Model Predictive Control*, vol. 384, ch. Explicit Approximate Model Predictive Control of Constrained Nonlinear Systems with Quantized Input, pp. 371–380. Springer Berlin Heidelberg, 2009.
- [14] N. Tom and R. W. Yeung, “Experimental confirmation of nonlinear model predictive control applied offline to a permanent magnet linear generator for ocean-wave energy conversion,” 2016. IEEE Journal of Oceanic Engineering, Vol. 41, No. 2, April 2016.
- [15] R. H. Hansen and M. M. Kramer, “Modelling and control of the wavestar prototype,” 2011. Proceedings of the 9th European Wave and Tidal Energy Conference: EWTEC 2011, University of Southampton, 2011.
- [16] J. Falnes, *Ocean Waves and Oscillating Systems*. Cambridge University Press, 2002.
- [17] N. H. Niels Pedersen, Magnus Asmussen and S. Jørgensen, “Control of hydraulicwave simulator system,” 2015. 7th Semester Project, Department of Energy Technology, Aalborg University.

- [18] PARKER, *PARKER D111FP NG32, DATA SHEET*.
- [19] MOOG, *MOOG D634-P series, DATA SHEET*.
- [20] J. A. Rossiter, *Model-Based Predictive Control: A Practical Approach*. CRC Press, 2003.
- [21] C. L. Phillips and J. M. Parr, *Feedback Control Systems*. Pearson, 5th ed., 2013.
- [22] M. M. K. Rico H. Hansen and E. Vidal, "Discrete displacement hydraulic power take-off system for the wavestar wave energy converter," 2013. In *Energies* 6: 4001-4044, August 2013.
- [23] F. Fusco and J. V. Ringwood, "Short-term wave forecasting for real-time control of wave energy converters," 2010. *IEEE Transactions on Sustainable Energy*, Vol. 1, NO 2, July 2010.
- [24] Y. O. Jin-Hua She, Hiroyuki Kobayashi and X. Xin, "Disturbance estimation and rejection - an equivalent input disturbance estimator approach," 2004. 43rd IEEE Conference on Decision and Control, December 14-17, 2004, Atlantis, Paradise Island, Bahamas.
- [25] K. Kuipers, "bnb." <https://se.mathworks.com/matlabcentral/fileexchange/95-bnb/content/BNB20.m>, 2000. [Online; accessed 09-March-2017].
- [26] R. Storn and K. Price, "Differential evolution - a simple and efficient adaptive scheme for global optimization over continuous spaces," 1995.
- [27] H. Li and L. Zhang, "Discrete hybrid differential evolution algorithm for solving integer programming problems," 2014. *Engineering Optimization*, 46:9, 1238-1268.
- [28] J. S. Arora, *Introduction to Optimum Design*. Elsevier Inc., 3rd ed., 2012.

A | Branch and Bound Algorithm

In this chapter a general explanation of the branch and bound optimisation algorithm used is elaborated.

The Branch and Bound Method (BnB) is an optimisation method developed for solving integer programming problems. The BnB is one of the earliest and most common algorithms used to solve discrete variable optimisation problems[28].

The implementation of the BnB is based on the concepts “branching”, “bounding” and from that creating a so-called solution tree of subspaces containing candidate solutions and searching for candidate solutions in the branches of the solution tree in a systematic manner. The systematic approach mainly consist of cutting off parts of the search three, often called fathoming a branch of the search tree, if it is possible to conclude that a branch of the search tree does not contain the optimal solution. The enumeration starts from the solution of the relaxed problem, and the initial subspace is the entire solution space. In general, a BnB algorithm has three main components listed below:

- *Bounding*: Find a lower bound of the best possible solution of a subspace of the entire solution space.
- *Selection*: A strategy of selecting the next subspace to investigate.
- *Branching*: If a subspace cannot be fathomed, a strategy of creating new subspaces by imposing constraints on the design variables.

Many different strategies for a BnB algorithm exist, and different strategies suits different problems. The BnB algorithm used in this thesis is a modified algorithm available from the Mathworks file exchange library[25]. A visual example of how the used BnB algorithm solves the integer problem is shown in the figure below, where some of the first steps in the enumeration of the search tree is explained. The example is taken from a MPC routine with a horizon length of $N = 10$, hence ten design variables in the optimisation problem.

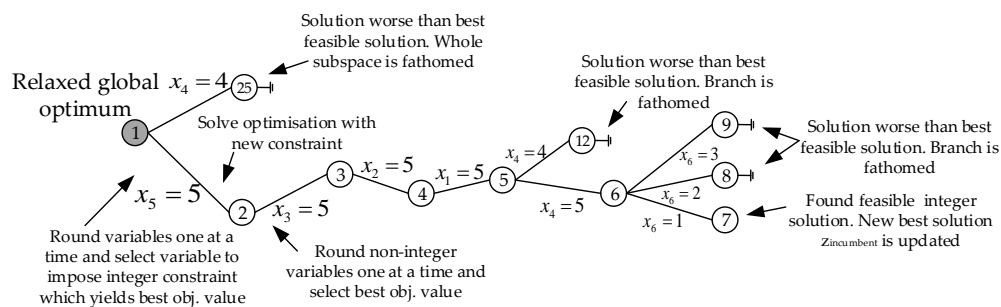


Figure A.1: Visual example of how the BBM algorithm solves the integer problem. The number of each subspace indicates the iteration number of the algorithm.

A simplified step by step procedure of the used algorithm is elaborated below:

Step 1:

A stack of candidate solution is initialized with an initial size of one. The first candidate solution is found from the initial guess and constraints provided by the user.

$$\textit{Initialize} : z_{\text{incumbent}} = \infty \quad c = 1 \quad (\text{A.1})$$

Step 2 - Update candidate solution:

Update constraints from stack:

$$x_l = x_{l,\text{stack}}(c) \quad (\text{A.2})$$

$$x_u = x_{u,\text{stack}}(c) \quad (\text{A.3})$$

Lower stack counter by one:

$$c = c - 1 \quad (\text{A.4})$$

Step 3 - Relaxation:

Solve relaxed problem of candidate solution.

$$(z, x) = \min\{F(x)\} \quad (\text{A.5})$$

$$\textit{st.} \quad x_l \leq x \leq x_u \quad (\text{A.6})$$

Step 4 - Fathoming:

Set selection = 1

$$\textit{if} \quad z \geq z_{\text{incumbent}} : \textit{Fathoming branch set selection} = 0 \quad (\text{A.7})$$

$$\textit{elseif integer solution} : z_{\text{incumbent}} = z, \quad x_{\text{incumbent}} = x, \quad \textit{set selection} = 0 \quad (\text{A.8})$$

Step 5 - Selection and branching:

if selection = 1:

1. Select variable to impose constraint: Round variables which are not integer one at a time, and select variable which yields lowest objective function to branch from.
2. Create branches based on branching strategy and store in stack.
3. Update stack counter, c , by number of new branches created.

Step 2-5 of the BnB algorithm is repeated until all branches are explored, hence all branches are fathomed. This corresponds to the stack counter is 0 of the step by step procedure above.

The BnB algorithm is only guaranteed to find the optimum solution if the problem formulation is linear or convex. This is evident from Table 5.1 when no losses is included in the objective function. When no losses is included the problem is a quadratic programming problem and is convex, why the BnB algorithm finds the optimum with a success rate of

100%. When losses are included the problem is no longer convex, and the BnB algorithm is sensitive to the solution of the relaxed problem. Since a derivative based algorithm is used to solve the relaxed problem, the relaxed global optimum is not guaranteed to be found, and a branch may be fathomed prematurely.

B | LabVIEW Program

This appendix chapter describes the implementation of the LabVIEW program developed for the MPC. A LabVIEW Real time target has already been setup for the AAU PTO test bench where the already existing datalogging, safety measures, fault handling, wave cylinder control and PTO manifold control is reused for this thesis. The MPC is incorporated as a sub VI, to fit the structure of the already existing LabVIEW program. A simplified of structure the Labview program is shown in the figure below:

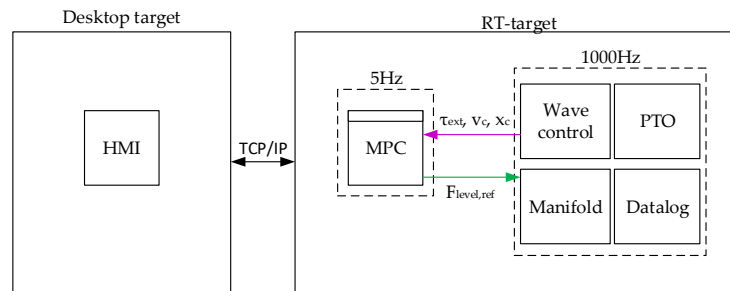


Figure B.1: Simplified structure of the LabVIEW program.

Control of the wave cylinder is performed in the Wave control VI. The force control of the PTO cylinder is done by the Manifold VI, and the line pressure control is performed in the PTO VI. The MPC VI calculates a force level reference which is send to the PTO manifold control VI. The LabVIEW project consist of two targets, a HMI is executed on a desktop PC, and the signal handling and process algorithms are executed on the RT target. To share variables between the two, “Network-Published” shared variables are used. Data variables which are passed from the MPC VI to other VI’s are also saved as shared variables, and without the use of buffering. The timed loop incorporated in the LabVIEW RT program is shown in the figure below.

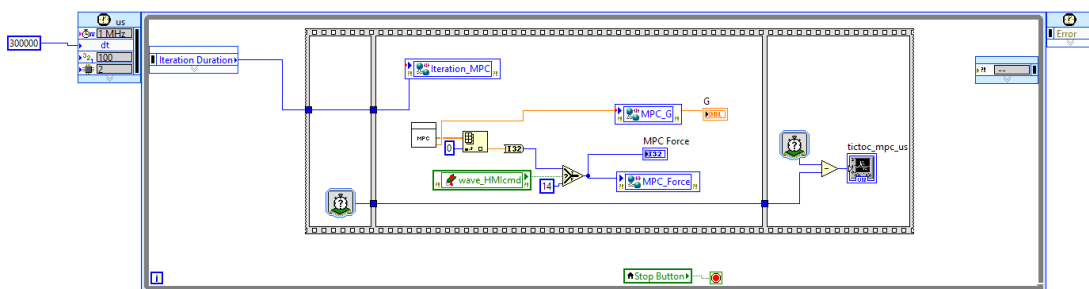


Figure B.2: Picture of the MPC VI as implemented in LabVIEW.

The MPC VI is placed in a flat sequence structure to allow measuring the execution time of the MPC calculation. The MPC VI is programmed to execute specific tasks in a sequence as follows:

1. If wave estimation is set to true, the wave predictor is given the current excitation torque fetched from the same excitation torque input given to the online simulation

of the point absorber computing the position reference for the wave cylinder. If ideal wave forecasting is used the future excitation torque is fetched from the excitation torque array, with a pointer offset corresponding to the time horizon of the MPC.

2. The optimisation problem is formulated. This is done by sampling the position and velocity of the PTO cylinder, and the Q matrix and the f vector is formulated. The prediction matrices used in the optimisation formulation are initialized at LabVIEW startup and saved in memory as local variables.
3. The DE algorithm is executed. The DE algorithm is placed in a case structure, such that different cost functions may be tested without having to reprogramming the MPC VI. The DE algorithm is executed in LabVIEW by configuration of a user library based on the shared library created with the LabWindowsCVI tool made by National Instrument. The solution of the DE is saved in memory through a feedback node, and used in the next iteration as “warm start”. The first entry in the solution from the DE is updated to the MPC Force variable as shown in Figure B.2, and passed to the PTO manifold control VI.

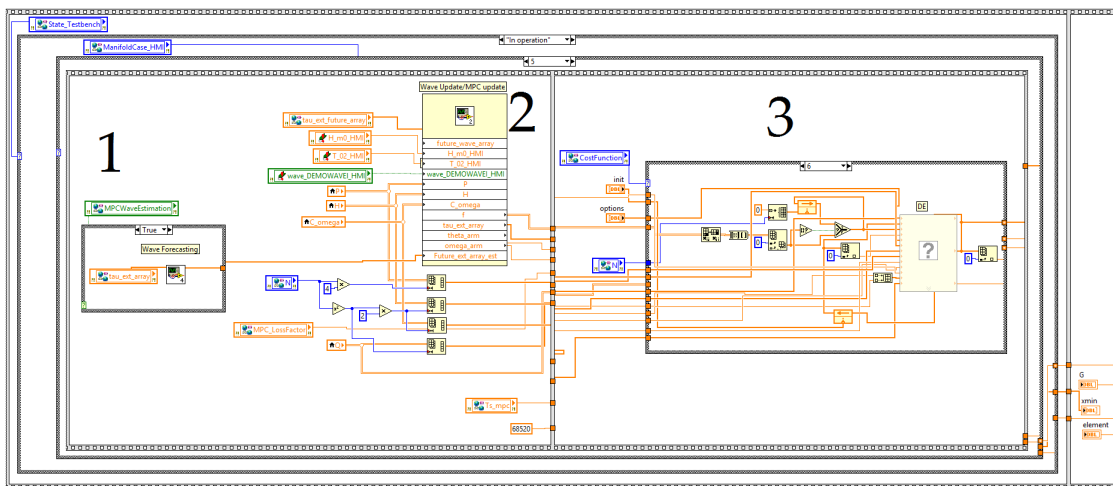


Figure B.3: Picture of the MPC VI structure as implemented in LabVIEW.

The whole process is repeated once the timed loop starts executing the code again after the sampling interval is passed.

B.1 Timing and Finish Late Handling

The timing of the MPC sub VI is performed with a use of the timed loop structure in LabVIEW to ensure that the MPC runs at the desired frequency. The execution of the MPC VI is started at a fixed interval, and the new force reference obtained from the solution of the MPC is send to the PTO control VI as fast as possible. A delay in this process is inevitable, and the MPC execution time may even exceed the frequency of the MPC loop if the MPC execution time is not handled in some manner. To ensure that finish late of the MPC VI does not occurs, the DE algorithm is set to terminate after approximately 100ms. This is done by setting the maximum number of generations in the DE algorithm to approximately correspond to an execution time of 100ms. The weakness of this approach is that the DE algorithm may be terminated before the optimum is

found. The solution given if the MPC terminates by exceeding the time limit is thus the best solution found during that time span. Another weakness is that the delay is varying, why the applied control input is not applied with a fixed interval.

B.1.1 Alternative Timing Handling Proposal

An alternative approach to the MPC execution shown in Figure 7.2 is proposed. In the implemented MPC scheme, elaborated in Chapter 7 the sample time of the MPC is chosen with a margin to the average convergence time of the DE algorithm to ensure that the DE always converges within the sample period. If the DE should not converge nothing is implemented to ensure that a control input is applied, and the LabVIEW program handles this as a finish late, hence the next iteration is skipped in order to obtain synchronization. To ensure that a solution is available at a fixed time interval the MPC may be formulated to calculate the next PTO force reference instead of the current. A timeline of the alternative MPC execution is shown in Figure B.4.

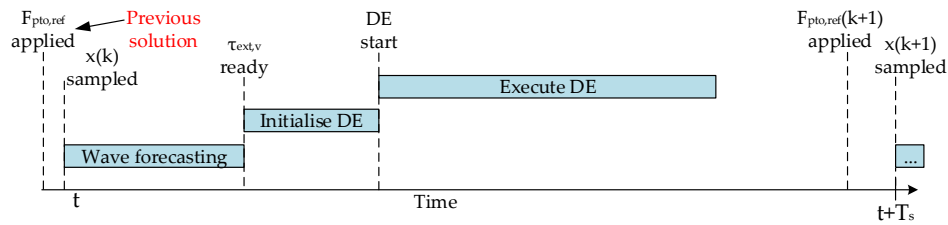


Figure B.4: Timeline of an alternative approach of executing the MPC algorithm.

By this approach the entire sample interval is available for the DE algorithm to converge. Thus the margin between the DE convergence time and MPC sample time could be lowered. This allows for including more members of each population in the DE algorithm to ensure that the DE algorithm converges to the true optimum. It may also be possible to increase the horizon length as effectively more time is allowed for the optimisation. If the DE algorithm has not converged within the sample interval the previous MPC solution may be utilised by taking the next sample. This approach ensures that the PTO force reference is applied with a fixed interval and allows to get rid of varying time delays due to the inconsistent convergence time of the DE. A disadvantage of this approach is that the computed control input is applied based on the next predicted states.

For the alternative approach the state prediction may be formulated as shown below:

$$\chi_{k+} = \mathbf{P}\mathbf{x}_k + \mathbf{H}(\tau_{\text{ext},v} - \tau_{\text{pto},v}) + \mathbf{F}(\tau_{\text{ext},k} - \tau_{\text{pto},k}) \quad (\text{B.1})$$

Where an additional term is added compared to the state prediction utilised in Equation (4.7). The additional term is the control input applied just before the state sampling has occurred. The prediction matrices is thus given as:

$$\mathbf{P} = \begin{bmatrix} \mathbf{A} \\ \mathbf{A}^2 \\ \mathbf{A}^3 \\ \vdots \\ \mathbf{A}^N \end{bmatrix} \quad \mathbf{H} = \begin{bmatrix} \mathbf{0} & \mathbf{0} & \cdots & \mathbf{0} \\ \mathbf{B} & \mathbf{0} & \cdots & \mathbf{0} \\ \mathbf{AB} & \mathbf{B} & \cdots & \mathbf{0} \\ \vdots & \vdots & \ddots & \vdots \\ \mathbf{A}^{N-2}\mathbf{B} & \mathbf{A}^{N-3}\mathbf{B} & \cdots & \mathbf{B} \end{bmatrix} \quad \mathbf{F} = \begin{bmatrix} \mathbf{B} \\ \mathbf{AB} \\ \mathbf{A}^2\mathbf{B} \\ \vdots \\ \mathbf{A}^{N-1} \end{bmatrix}$$

Where the future excitation torques and future control inputs to be solved for in the optimisation is shifted one sample period, and is for the same time horizon one less in length than the method implemented in Chapter 7.

$$\boldsymbol{\tau}_{\text{ext},v} = [\boldsymbol{\tau}_{\text{ext},k+1} \quad \boldsymbol{\tau}_{\text{ext},k+2} \quad \cdots \quad \boldsymbol{\tau}_{\text{ext},k+N-1}]^T \quad (\text{B.2})$$

$$\boldsymbol{\tau}_{\text{pto},v} = [\boldsymbol{\tau}_{\text{pto},k+1} \quad \boldsymbol{\tau}_{\text{pto},k+2} \quad \cdots \quad \boldsymbol{\tau}_{\text{pto},k+N-1}]^T \quad (\text{B.3})$$

The proposed formulation of the MPC given in this section allows for better timing handling of the control input. Secondly more time is allowed for the optimisation problem as the entire sampling period is available to compute the next control input. the proposed formulation has not been evaluated experimentally, why it is left for future work.

B.2 MATLAB Code

DE Algorithm

```

1 function [xmin,fmin,dur,G] = de(objective,init)
2 %% Declare options
3 D      = 10;           % Number of design variables
4 NP     = 350;         % Population size
5 CR     = 0.8;         % Crossover factor
6 F      = 0.8;         % Mutation factor
7 Gmax   = 150;         % Maximum Generations
8 Tol    = 1e-8;        % Tolerance for stop criteria
9 Tf     = 5;           % Length of history for stop criteria
10 history = rand(1,Tf); % History for the objective values in the ...
    population
11
12 %% Initialization and evaluation of first population
13 pop.x = randi([-1 1],NP,D)+init; % Initialise population
14 pop.f = feval(objective);        % Evaluate initial population
15 new.x = zeros(NP,D);             % Initialise new population
16 new.f = zeros(NP,1);            % Initialise new population evaluation
17 G     = 0;                       % Initialise generation counter
18
19 %% The loop through generations
20 while (std(history) ≥ Tol && G ≤ Gmax)
21
22 %% Mutation
23 % Select three random members for each member
24 ind      = randi([1 NP],NP,3);
25 % Find best solution in current population
26 best     = find(pop.f==min(pop.f),1);
27 % Generate new population
28 new.x    = pop.x(ind(:,1),:) + F * ( pop.x(best(1),:) - ...
    pop.x(ind(:,1),:) + F * ( pop.x(ind(:,2),:) - pop.x(ind(:,3),:)));
29
30 %% Crossover
31 % Generate random number
32 temp     = rand(NP,D);
33 % Check if random number higher than CR
34 ind      = (temp > CR);
35 % Keep old member if random number higher than CR
36 new.x(ind) = pop.x(ind);
37 % Evaluate trial population
38 new      = feval(objective);
39
40 %% Selection
41 % Is child 1 worse than member 1
42 ind      = (new.f(:,end) > pop.f(:,end));
43 % Is child 1 worse than member 1 then keep member
44 new.x(ind,:) = pop.x(ind,:);
45 % Is child 1 worse than member 1 then keep member
46 new.f(ind,:) = pop.f(ind,:);
47
48 % Preparation for the next generation
49 pop      = new; % Population ...
    for next generation initialization
50 temp     = sum(pop.f);
51 history(mod(G,options.Tf)+1) = temp; % Update history
52 G       = G + 1; % Update ...
    generation number

```

```

53 end % end loop through generations
54
55 %% Final Solution
56 ind      = find(pop.f==min(pop.f));           % Find mimimum ...
           cost evaluation of final generation
57 xmin     = pop.x(ind(1),1:D);               % Final solution
58 fmin     = pop.f(ind(1),:);                 % Final

```

Cost Function without losses

```

1 %% Cost function without loss included
2 function [ f ] = Cost(x,NP,ff,Tau0,H)
3 % Compute cost evaluation with no loss included
4 % Initialise vector of cost evaluations
5 f = zeros(NP,1);
6 % Declare vector of PTO moments to translate from force level to ...
   applied torque
7 F = 1e5 * 2.36.*...
8 [-3.812 -3.116 -2.836 -2.420 -2.140 -1.932 -1.860 -1.444 -1.236...
9 -1.164 -0.956 -0.540 -0.468 -0.260 -0.052 0.020 0.436 0.644...
10 0.716 0.924 1.340 1.412 1.620 1.900 2.316 2.596 3.292];
11 % Translate from forcelevel to applied torque
12 tau = F(x);
13 % Calculate absorbed energy
14 for i = 1:NP
15 f(i,1) = 0.2*(tau(i,:)*H*tau(i,:) + ff'*tau(i,:));
16 end
17 end

```

Cost Function with Shifting Losses

```

1 %% Compute cost evaluation with loss included as lookup table
2 function [ f ] = Cost(x,NP,ff,Tau0,H,E,Ts,N)
3 % Initialise variables
4 f      = zeros(NP,1);           % vector of cost evaluations
5 Eloss = zeros(NP,10);         % matrix of static shifting loss
6 % Declare vector of PTO moments to translate from force level to ...
   applied torque
7 F = 1e5 * 2.36.*...
8 [-3.812 -3.116 -2.836 -2.420 -2.140 -1.932 -1.860 -1.444 -1.236...
9 -1.164 -0.956 -0.540 -0.468 -0.260 -0.052 0.020 0.436 0.644...
10 0.716 0.924 1.340 1.412 1.620 1.900 2.316 2.596 3.292];
11 % Translate from forcelevel to applied torque
12 tau = F(x);
13 % Declare lookkup table of static shifting loss
14 Etot = E;           % Fetch lookup table containing shifting losses
15 % Calculate shifting loss based on lookup table, Etot
16 for jj = 1:NP
17 Eloss(jj,1) = Etot(Tau0,x(jj,1));
18 for ii = 2:N
19 Eloss(jj,ii) = Etot(round(x(jj,ii-1)),round(x(jj,ii)));
20 end
21 end
22 % Translate from forcelevel to applied torque

```

```

23 tau = F(x);
24 % Calculate absorbed energy static shifting loss and throttle loss
25 for i = 1:NP
26 f(i,1) = Ts*(tau(i,:)*H*tau(i,:) + ff'*tau(i,:)' + ... % absorbed energy
27 sum(Eloss(i,:)); % static shifting loss from lookup table
28 end
29 end

```

Cost Function with Shifting and Throttle Losses

```

1 %% Compute cost evaluation with loss included as lookup table and ...
  throttle losses
2 function [ f ] = Cost(x, NP, ff, Tau0, H, AA, BB, CC, tauk, xk, thro_co, E, Ts, N)
3 % Initialise variables
4 f = zeros(NP,1); % vector of cost evaluations
5 Eloss = zeros(NP,10); % matrix of static shifting loss
6 % Declare vector of PTO moments to translate from force level to ...
  applied torque
7 F = 1e5 * 2.36.*...
8 [-3.812 -3.116 -2.836 -2.420 -2.140 -1.932 -1.860 -1.444 -1.236...
9 -1.164 -0.956 -0.540 -0.468 -0.260 -0.052 0.020 0.436 0.644...
10 0.716 0.924 1.340 1.412 1.620 1.900 2.316 2.596 3.292];
11 % Translate from forcelevel to applied torque
12 tau = F(x);
13 % Declare lookup table of static shifting loss
14 Etot = E; % Fetch lookup table containing shifting losses
15 % Calculate shifting loss based on lookup table, Etot
16 for jj = 1:NP
17 Eloss(jj,1) = Etot(Tau0,x(jj,1));
18 for ii = 2:N
19 Eloss(jj,ii) = Etot(round(x(jj,ii-1)),round(x(jj,ii)));
20 end
21 end
22 % Translate from forcelevel to applied torque
23 tau = F(x);
24 % Calculate absorbed energy static shifting loss and throttle loss
25 for i = 1:NP
26 f(i,1) = Ts*(tau(i,:)*H*tau(i,:) + ff'*tau(i,:)' + ... % absorbed energy
27 abs((CC*(AA*xk + BB*(tauk-tau(i,:))) * 2.36)' * (thro_co) * abs((CC*(AA*xk ...
  + BB*(tauk-tau(i,:))) * 2.36).^2)) + ... % throttle loss
28 sum(Eloss(i,:)); % static shifting loss from lookup table
29 end
30 end

```

Cost Function with Complete Losses

```

1 %% Compute cost evaluation with shifting loss and throttle loss calculated
2 function [ f ] = Cost(x, NP, ff, tau0, H, tauk, x0, N)
3 % Initialise variables
4 f = zeros(NP,1); % vector of cost evaluations
5 Eloss = zeros(NP,10,3); % matrix of static shifting loss
6 xx = zeros(NP,20); % system states
7 p = zeros(3,27); % pressure lookup table

```

```

8 % Declare vector of PTO moments to translate from force level to ...
   applied torque
9 F = 1e5 * 2.36.*...
10 [-3.812 -3.116 -2.836 -2.420 -2.140 -1.932 -1.860 -1.444 -1.236...
11 -1.164 -0.956 -0.540 -0.468 -0.260 -0.052 0.020 0.436 0.644...
12 0.716 0.924 1.340 1.412 1.620 1.900 2.316 2.596 3.292];
13 % Translate from force level to applied torque
14 tau = F(x);
15 % Calculate system states
16 for k = 1:NP
17 xx(k,:) = A * x0 + B * (tau(k, :)-tau_k)';
18 end
19 % Convert point absorber states to cylinder states
20 xx(:,1:2:options.N*2-1) = -xx(:,1:2:options.N*2-1)*2.36;
21 xx(:,2:2:options.N*2) = -xx(:,2:2:options.N*2)*2.36 + 1;
22 % Declare line pressure constants
23 pL = 20e5;
24 pM = 100e5;
25 pH = 180e5;
26 % Declare pressure lookup table
27 p(1,:) = [pH pH pH pH pH pM pH pH pM pH pM pM pH pM pL pM pM pL pM pL ...
   pL pM pL pL pL pL pL];
28 p(2,:) = [pL pL pM pL pM pL pH pM ...
   pL pH pM pH pM pH pH];
29 p(3,:) = [pL pM pL pH pM pL pL pH pM pM pL pH pH pM pL pL pH pM pM pL ...
   pH pH pM pL pH pM pH];
30 % Declare system parameter
31 A = [-0.0235 0.0122 0.0087];
32 Beta = 7000e5;
33 V0 = [0.04814 0.00114 0.000228];
34 T = 50e-3;
35 kv = 1.005116102984629e-06;
36 n = [18 10 8];
37 for j = 1:NP
38 for i=1:3
39 Eloss(j,1,i) = 0.5 *(p(i,x(1))-p(i,tau0))^2 * (V0(i) + (x0(2))*A(i) ...
   )/Beta + abs(A(i)*x0(1))^3 / (n(i)*kv)*Ts;
40 for ii = 2:N
41 Eloss(j,ii,i) = 0.5 *(p(i,x(j,ii))-p(i,x(j,ii-1)))^2 * (V0(i)+ ...
   (xx(j,2*ii-1))*A(i) )/Beta + abs(A(i)*xx(j,2*ii-1))^3 / ...
   (n(i)*kv)*0.2 ;
42 end
43 end
44 end
45 Eloss_tot = sum(sum(Eloss,2),3);
46 % Calculate absorbed energy minus the energy loss
47 for i = 1:NP
48 f(i,1) = f(i,1) = Ts*(tau(i,:) * H * tau(i,:))' + ff' * tau(i,:) + ... % ...
   absorbed energy
49 abs((CC*(AA*xk + BB*(tau_k - tau(i,:))) * 2.36)' * (thro_co) * abs((CC*(AA*xk ...
   + BB*(tau_k - tau(i,:))) * 2.36).^2)) + ... % throttle loss
50 sum(Eloss(i,:)); % static shifting loss from lookup table
51 end
52 end

```

C | Results

In this appendix the experimental results are summarised in tables. The following MPC schemes are shown:

- MPC1: $T_s = 0.2s$, $N = 5$, Static shifting loss: Equation (5.8).
- MPC2: $T_s = 0.2s$, $N = 10$, Static shifting loss: Equation (5.8).
- MPC3: $T_s = 0.3s$, $N = 10$, Static shifting loss: Equation (5.8).
- MPC4: $T_s = 0.3s$, $N = 10$, Static shifting loss and throttle loss: Equation (5.9).
- MPC4 est: Same as MPC4, but evaluated with wave forecasting.

In Table C.1 the average absorbed power for different MPC schemes and the test waves given in Table 6.1 is shown.

<i>Wave</i>	1	2	3	4	5
$P_{abs,avg}[kW]$					
Reactive	3.06	5.97	9.87	17.60	25.80
MPC 1	1.45	2.17	4.28	7.00	11.99
MPC 2	2.61	7.45	11.28	21.88	29.52
MPC 3	3.27	8.65	12.47	22.64	30.47
MPC 4	3.17	8.02	12.43	22.92	31.13
MPC 4 est	2.73	7.52	11.71	22.02	30.48

Table C.1: Average absorbed power for different control schemes and test waves.

In Table C.2 the average harvested power for different MPC schemes and the test waves given in Table 6.1 is shown.

<i>Wave</i>	1	2	3	4	5
$P_{har,avg}[kW]$					
Reactive	2.11	4.56	8.09	15.38	22.96
MPC 1	1.00	1.64	3.52	5.89	10.38
MPC 2	1.37	4.65	8.11	17.88	24.62
MPC 3	1.86	5.65	9.13	18.64	25.71
MPC 4	1.94	5.64	9.19	19.28	26.77
MPC 4 est	1.36	5.23	8.88	18.65	26.49

Table C.2: Average harvested power for different control schemes and test waves.

In Table C.3 the efficiency for different MPC schemes and the test waves given in Table 6.1 is shown.

<i>Wave</i>	1	2	3	4	5
<i>Efficiency</i>					
Reactive	0.69	0.76	0.82	0.87	0.89
MPC 1	0.69	0.75	0.82	0.84	0.86
MPC 2	0.52	0.62	0.72	0.82	0.83
MPC 3	0.57	0.65	0.69	0.82	0.84
MPC 4	0.61	0.70	0.74	0.82	0.84
MPC 4 est	0.49	0.69	0.76	0.84	0.87

Table C.3: *Efficiency for different control schemes and test waves.*